Simulation and beam test measurements of the CMS pixel detector

Dissertation

zur

Erlangung der naturwissenschaftlichen Doktorwürde (Dr. sc. nat.)

vorgelegt der

Mathematisch-naturwissenschaftlichen Fakultät

der

Universität Zürich

von

Enver Alagöz

aus der Türkei

Promotionskomitee

Prof. Dr. Claude Amsler (Leitung der Dissertation)

Prof. Dr. Vincenzo Chiochia

Dr. Alexander Schmidt

Zürich, 2009

Abstract

The CMS experiment located at the CERN Large Hadron Collider (LHC) consists of a silicon pixel detector as the innermost device. The pixel detector plays an important role in the reconstruction of tracks and interaction vertices. In the harsh LHC radiation environment with large track multiplicities a good pixel device performance is a big challenge. In the innermost layer of the pixel detector the sensors will be exposed to a fluence of 3×10^{14} $n_{eq}/cm^2/yr$ at full LHC luminosity with consequent degradation of the silicon lattice structure and particle detection performances. In this PhD thesis the simulation and beam test measurements for the CMS pixel barrel detector are presented. In particular, the performances of irradiated sensors are studied.

A detailed Monte Carlo simulation is performed for the CMS pixel sensors. The simulation incorporates an effective radiation damage model to predict sensor performance after irradiation. The simulation has important impacts on the development of accurate particle hit reconstruction algorithms and the calibration of the charge sharing functions. The simulated position resolutions with existing hit reconstruction algorithms are studied and the results are presented. The simulation shows that a position resolution for perpendicular tracks in 3 T magnetic field along the CMS transverse plane is 10 μm for an unirradiated sensor and 18 μm for a heavily irradiated sensor. In addition, it is shown that the systematic effects due to radiation damage in pixel sensors can be corrected.

The CMS pixel sensors are tested on a high energy pion beam at CERN at several bias voltages and irradiation fluences in a 3 T magnetic field. These tests are performed for the first time with the final sensor dimensions and the final front-end electronic in a magnetic field. The measurements as a function of irradiation fluence are: charge collection, leakage current and related damage rates, signal-to-noise ratio, and position resolutions. Futhermore, the position resolution as a function of readout threshold is presented for an unirradiated sensor.

An important result is that the position resolution of an unirradiated sensor is 11 μm at 200 V, while for a sensor irradiated to a fluence of $6.2\times\ 10^{14}$ $n_{eq}cm^{-2}$ the resolution is 21 μm at 300 V bias for tracks perpendicular to the sensors in the CMS transverse plane. The position resolution is degraded by at most 30% when the readout threshold increases to 6500 electrons. The resolution for events in which the charge is shared between adjacent pixels remains constant. This is due to the fact that the operated bias voltage is same for all the threshold measurements.

A simulation and beam test comparison are performed. Good agreement is observed between the simulation and beam test results.

This PhD thesis work has led to the publications [1] [2] [3].

Zusammenfassung

Der innerste Teil des CMS Experiments am CERN 'Large Hadron Collider' (LHC) ist ein Silizium Pixeldetektor. Der Pixeldetektor spielt eine wichtige Rolle in der Rekonstruktion des Wechselwirkungsvertex und der zugehörigen Teilchenspuren.

Es ist eine grosse Herausforderung, unter der harten Strahlungsbelastung am LHC eine hohe Leistung des Pixeldetektors zu gewährleisten. Wenn der LHC seine volle Luminosität erreicht hat, werden die Sensoren in der innersten Schicht des Pixeldetektors einer Fluenz von 3×10^{14} $n_{eq}/cm^2/yr$ ausgesetzt sein. Diese hohe Strahlungsbelastung führt zu einer Auflösung der Gitterstruktur des Siliziums und damit zu einer geringeren Leistungsfähigkeit in der Teilchendetektion. In dieser Doktorarbeit werden Simulationen und Testmessungen für den zylinderförmigen Teil des CMS Pixeldetektors vorgestellt. Besondere Aufmerksamkeit wird dabei der Leistungsfähigkeit von bestrahlten Sensoren geschenkt.

Es wurde eine detaillierte Monte Carlo Simulation für den Pixeldetektor durchgeführt. Um die Leistung von bestrahlten Sensoren vorhersagen zu können, beinhaltet die Simulation ein effektives Modell für Strahlungschäden. Die Ergebnisse dieser Simulation haben einen hohen Einfluss auf die Entwicklung genauerer Algorithmen zur Rekonstruktion von Teilchentreffern und auf die Kalibrierung von Funktionen zur Beschreibung der Ladungsaufteilung. Die durch die Simulation bestimmten Ortsauflösungen verschiedener Algorithmen werden miteinander verglichen. Die Simulation zeigt dass die Ortsauflösung für senkrechte Spuren und unbestrahlte Sensoren in einem 3 T starken Magnetfeld 10 μm entlang der transversalen Ebene des CMS Detektors beträgt. Für stark bestrahlte Sensoren verschlechtert sich die Ortsauflösung bis zu 18 μm. Es wird dargelegt, dass es möglich ist, die systematischen Effekte durch Strahlungschäden zu korrigieren.

Unterschiedlich stark bestrahlte CMS Pixelsensoren wurden in einem 3 T starken Magnetfeld mit einem Pionenstrahl am CERN für verschiedenen Basisvorspannungen getestet. Es war das erste Mal, dass solche Tests im Magnetfeld für Sensoren mit der endgültigen Abmessung und Front-End-Elektronik durchgeführt wurden. Die folgenden Grössen wurden in Abhängigkeit von der Strahlungsbelastung gemessen: Ladungsammlung, Verluststrom und die zugehörige Schadenshäufigkeit, Signal-Rausch-Verhältnis und Ortsauflösung. Die Ortsauflösung eines unbestrahlten Sensors wird zusätzlich als Funktion der Ausleseschwelle angegeben.

Ein wichtiges Ergebnis dieser Studien ist, dass die Ortsauflösung für senkrechte Spuren und unbestrahlte Sensoren bei einer Basisvorspannung von 200 V 11 μm entlang der transversalen Ebene des CMS Detektors beträgt. Für Sensoren, die mit einer Fluenz von 6.2×10^{14} $n_{eq}cm^{-2}$ bestrahlt wurden, beträgt die Auflösung dagegen 21 μm bei einer Basisvorspannung von 300 V. Die absolute Ortsauflösung verschlechtert sich um maximal 30%, wenn die Ausleseschwelle angehoben wird. Die Ortauflösung für Ereignisse, bei denen sich die Ladung zwichen benachbarten Pixeln aufteilt, bleibt konstant. Dieses Ergebnis ist der Tatsache geschuldet, dass bei allen Schwellenmessungen die gleiche Basisvorspannung anlag. Es wurde ein Vergleich zwischen den Ergebnissen des Tests und der Simulation durchgeführt und eine gute Übereinstimmung festgestellt.

Diese Doktorarbeit führte zu den Veröffentlichungen [1] [2] [3].

Contents

1 Introduction

During the last century much progress has been made in elementary particle physics. Many experiments were performed contributing to discoveries which converged into the Standard Model (SM) of particle physics. This model explains the constituents of matter and their interactions in nature. The SM describes strong, weak and electromagnetic interactions (forces) which are based on gauge theories. Most of the SM building blocks have been tested with a very high accuracy. All these measurement results are in good agreement with the theoretical predictions. As a result, the particle physics data up to now is explained by the SM with a great precision. Despite all achievements in particle physics, there are several open questions to be answered. Especially, the origin of the particle masses.

In the SM, the Z^0, W, and γ are the gauge bosons of the electroweak symmetry group $SU(2)_L \otimes U(1)_Y$. While the Z^0 and W bosons have large masses, the γ boson has zero mass. The large difference between the boson masses is explained by the electroweak symmetry breaking down to the electromagnetic symmetry group $U(1)_{em}$. The hypothetical spontaneous symmetry breaking is due to the non-vanishing vacuum expectation value of the scalar Higgs field. The quanta of this field are the Higgs bosons [4].

The spontaneous symmetry breaking mechanism could explain the origin of the particle masses. Therefore, the discovery of the Higgs boson would be a very important achievement for the SM. So far the working particle accelerators have not detected it but they have put upper and lower limits on its mass.

Discovery of the Higgs boson and physics searches beyond the SM are among the main motivations for the Large Hadron Collider (CERN, Switzerland) project.

1.1 The Higgs boson in the Standard Model

The Higgs boson is one of the most important theoretical ingredient of the SM. It has zero spin and is its own antiparticle. The SM does not predict the mass of the Higgs boson. Therefore, predicted Higgs production cross sections vary by many orders of magnitude, depending on the assumed mass of the Higgs particle and its production mechanism. The most important production processes are:

- gluon fusion (the dominant production mechanism at the LHC);
- vector boson fusion;
- associated $t\bar{t}H$;
- Higgs radiation from Z, and W.

The experimental lower limit on the Higgs mass measured by the LEP experiments is 115.6 GeV/c^2 [5]. In addition, a mass higher than 1 TeV/c^2 is disfavored by theory unitary bounds.

Furthermore, the FNAL [1] experiments exclude the production of a SM Higgs boson with mass between 160 and 170 GeV/c^2 [6]. Experimentally accessible Higgs decays are listed in Table 1.1 and their predicted branching ratios and cross sections are shown in Fig. 1.1.

The most promising channel is $H \to \gamma\gamma$ if the Higgs mass is lower than 150 GeV/c^2 and providing that a very good electromagnetic calorimeter for precise photon identification is available. The leptonic decay channels are in the high Higgs mass range. Discovery in these channels requires good performance of the muon detectors as well as the tracker and electromagnetic calorimeter. For the channels with missing transverse energy [2], E_T^{miss}, plus leptons and jets one needs a high performance hadronic calorimeter. The Compact Muon Solenoid (CMS) experiment, which is built on the Large Hadron Collider (LHC), has been designed to fulfill the requirements mentioned above.

Table 1.1 Experimentally accessible Higgs decay channels [7].

Mass range	Decay channel
100 GeV $\lesssim m_H \lesssim$ 150 GeV	$H \to \gamma\gamma$
90 GeV $\lesssim m_H \lesssim$ 120 GeV	$H \to b\bar{b}$ in $t\bar{t}H$
50 GeV $\lesssim m_H <$ 200 GeV	$H \to \tau^+\tau^-$
130 GeV $\lesssim m_H \lesssim$ 200 GeV	$H \to ZZ^* \to 4\ell$ (e or μ)
140 GeV $\lesssim m_H \lesssim$ 180 GeV	$H \to WW^* \to \ell\ \nu\ \ell\nu$
200 GeV $\lesssim m_H \lesssim$ 750 GeV	$H \to ZZ^* \to 4\ell$
500 GeV $\lesssim m_H \lesssim$ 1 TeV	$H \to 2\ell\ 2\nu$
$m_H \approx$ 1 TeV	$H \to WW^* \to \ell\ \nu$ + 2 jets
$m_H \approx$ 1 TeV	$H \to ZZ^* \to 2\ell$ + 2 jets

The SM Higgs boson may be discovered anywhere within the whole mass range from the measured lower bound 115.6 GeV/c^2 (LEP) to the theoretical upper bound of 1 TeV/c^2.

1.2 The Large Hadron Collider and its experiments

The Large Hadron Collider (LHC) [9] is a circular proton-proton collider at the European Organization for Nuclear Research (CERN) lying under Swiss-French border near Geneva, Switzerland. The overview of the LHC tunnel and infrastructure is shown in Fig. 1.2. The proton beam bunches will be accelerated up to 7 TeV in opposite directions with a bunch separation of 25 ns. In each bunch, there will be 1.15$\times$ 10^{11} protons. The LHC will reach a 14 TeV center-of-mass energy. However, for the first year the center of mass energy is going to be 10 TeV due to technical problems. In addition, a heavy ion (Pb^{82+}) program will be conducted at the LHC. The LHC design luminosity is 10^{34}cm^{-2}s^{-1} but initially it will be operating with a luminosity of 10^{32}cm^{-2}s^{-1}. The LHC is scheduled to start colliding beams in the autumn 2009.

One of the main physics motivation for the LHC project is the search for the Higgs boson. In addition, the LHC will

[1] Fermi National Accelerator Laboratory: http://www.fnal.gov/.
[2] Due to escape of the neutrinos without interaction in the detector.

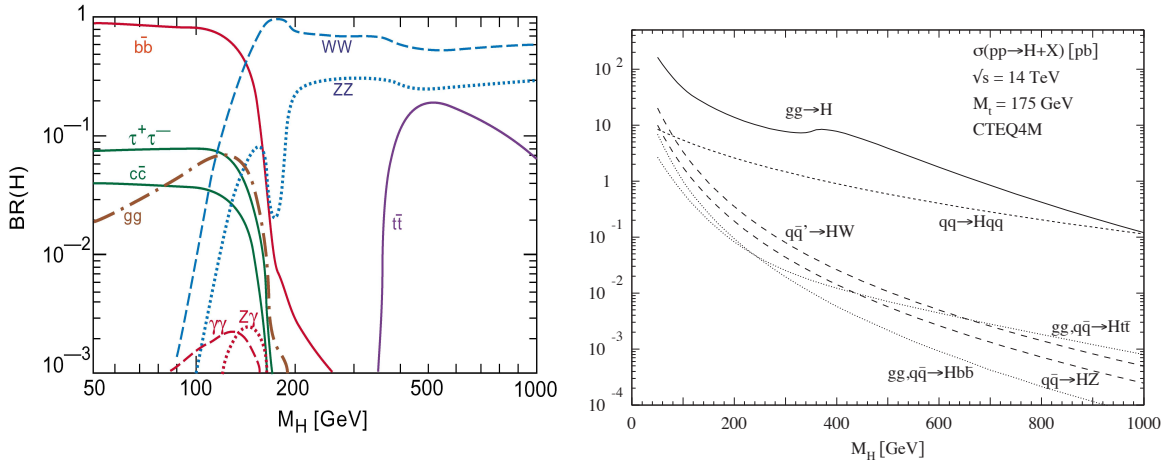

Figure 1.1 Left: branching fractions of the SM Higgs boson as a function of its mass M_H. Right: Higgs production cross sections [8]

- explore new physics beyond the SM (e.g. SUSY, extra dimensions etc.);
- allow measurements of the SM parameters with extraordinary precision in order to compare and find deviations from the SM predictions;
- study quark-gluon plasma in heavy ion collisions.

The LHC ring is equipped with several experiments (see Fig. 1.2):

- ATLAS - **A** **T**oroidal **L**HC **A**pparatus [10]
- CMS - **C**ompact **M**uon **S**olenoid [11]
- ALICE - **A** **L**arge **I**on **C**ollider **E**xperiment [12]
- LHCb - The **L**arge **H**adron **C**ollider **b**ottom Experiment [13]
- TOTEM - **TOT**al cross section, **E**lastic scattering and diffraction dissociation **M**easurements [14]

ATLAS and CMS are general-purpose detectors. ALICE is mainly dedicated to heavy ion physics and LHCb to bottom quark physics. TOTEM is designed to measure the total proton-proton cross-section, elastic scattering and search for diffractive processes.

1.3 The CMS experiment

CMS is one of two general purpose experiments at the LHC and it is located at Point 5 as shown in Fig. 1.2. It is designed to take data using both proton-proton and ion-ion collisions. The main physics goals are the search for the SM Higgs boson and physics beyond the SM, heavy quarks, and heavy ion physics.

CMS has to fulfill several requirements [15]:

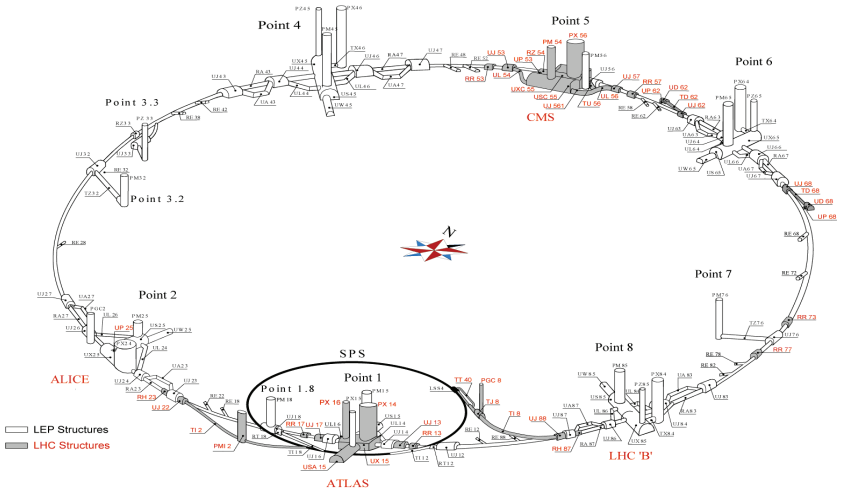

Figure 1.2 Overview of LHC ring and infrastructure [9].

- Good muon identification and momentum resolution over a wide range of momenta in the pseudorapidity [3] region $\eta < 2.5$, good dimuon mass resolution ($\approx 1\%$ at 100 GeV/c^2), and the ability to determine unambiguously the charge of muons with $p < 1$ TeV/c.
- Good charged particle momentum resolution and reconstruction efficiency in the inner tracker. Efficient triggering and offline tagging of τ's and b-jets, requiring pixel detectors close to the interaction region.
- Good electromagnetic energy resolution, good diphoton and dielectron mass resolution ($\approx 1\%$ at 100 GeV/c^2), wide geometric coverage ($\eta < 2.5$), measurement of the direction of photons and/or correct localization of the primary interaction vertex, π^0 rejection and efficient photon and lepton isolation at high luminosities.
- Good transverse missing energy E_T^{miss} and dijet mass resolution, requiring hadron calorimeters with a large hermetic geometric coverage ($\eta < 5$) and with fine lateral segmentation.

The requirements above led to the detector design shown in Fig. 1.3. Ideally, the detector shape would be spherical for best hermeticity but this is almost impossible technically. A cylindrical shape therefore is chosen to achieve very good geometrical coverage and include a magnetic solenoid for particle momentum measurements.

CMS comprises several sub detectors (see Fig. 1.3). An assembled part of the CMS experiment in SX5 underground is shown in Fig. 1.4. The sub detectors from the innermost to outermost are

- the inner tracker (silicon strips and pixels)
- the electromagnetic calorimeter
- the hadronic calorimeter and

[3] Pseudorapidity is defined as $\eta = -\ln(\tan\frac{\theta}{2})$, where θ is the angle between the beam pipe and the particle track. Each η unit has almost the same number of particles.

- the muon system.

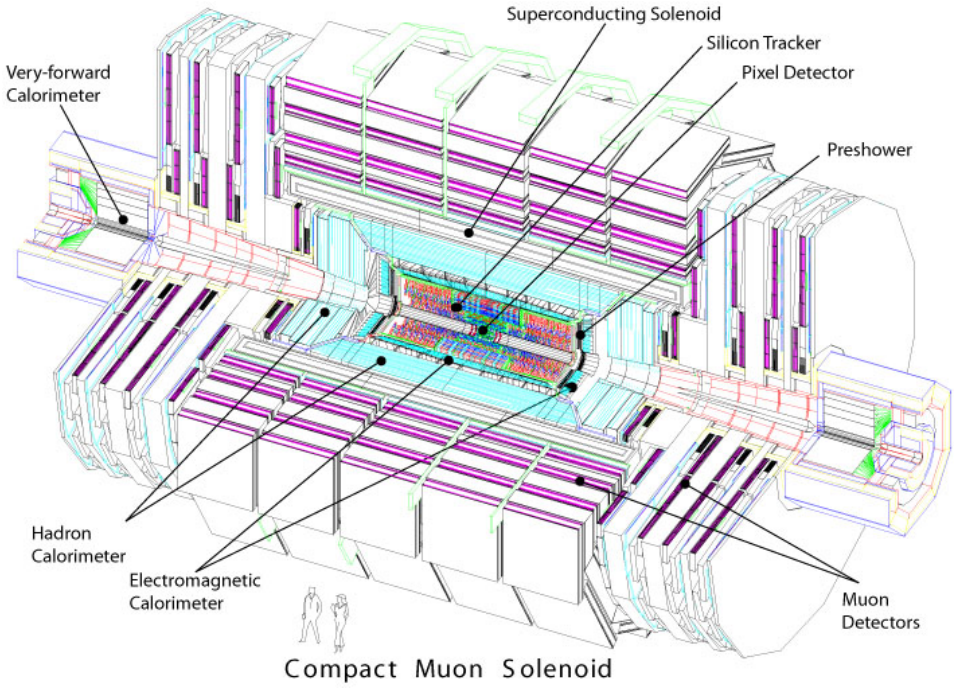

Figure 1.3 Overall layout of the CMS experiment and its subdetector components [11].

The origin of the CMS coordinate system is at the interaction point, the y-axis pointing vertically upward, and the x-axis pointing radially inward towards the center of the LHC ring. The z-axis points along one of the beam direction (towards the Jura mountains). The azimuthal angle ϕ is measured from the x-axis in the x-y plane. The polar angle θ is measured from the z-axis. These coordinates will also be used later in this thesis.

1.3.1 Magnet

As mentioned before, CMS requires a high performance of the muon system and a momentum resolution of 10% at $p = 1$ TeV/c. Therefore a large magnet is chosen for CMS [16], composed of a superconducting solenoid and a magnet yoke. The solenoid is 13 m long and has an inner diameter of 6 m. It contains the tracker and calorimeters. The magnetic field inside the solenoid is 4 T while in the yoke it is 2 T. The bending direction within the solenoid is opposite to the one in the magnet yoke, as shown in Fig. 1.5. This provides a longer path for the energetic muons, increasing the precision of muon momentum measurements.

1.3.2 Inner tracking system

The expected charged particle flux as a function of the distance to the interaction point determined the design of the inner tracker system. At a distance of 4 cm a flux of up to 100 MHz/cm^2 is expected. The innermost part of the tracker will be exposed to very high radiation doses, with time causing severe radiation damage to the tracker material. The radiation dose

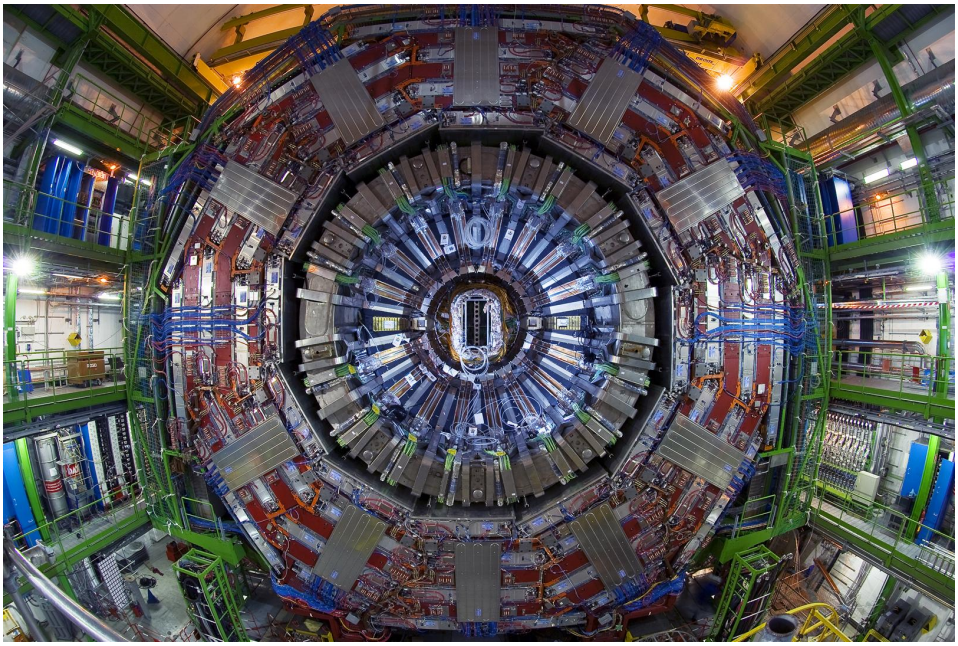

Figure 1.4 An assembled part of the CMS in the underground experimental cavern.

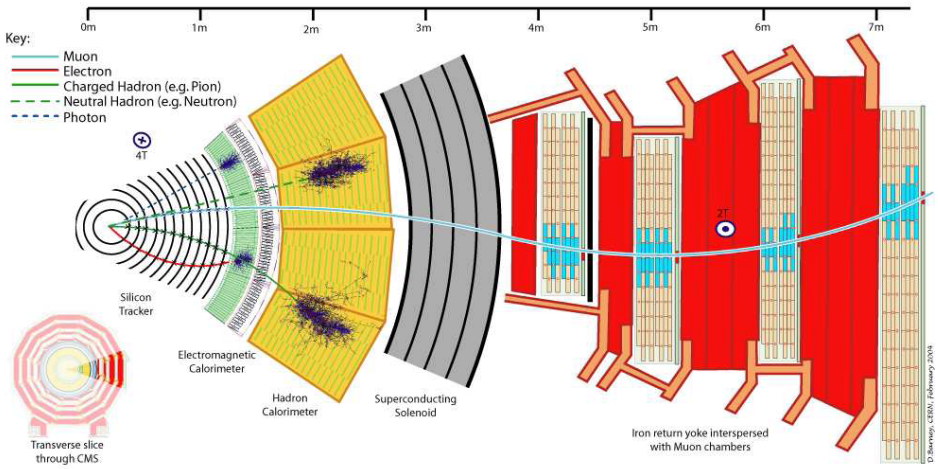

Figure 1.5 Transverse slice of the CMS experiment. The neutral and charged particles tracks are shown [11].

is proportional to $1/r^2$, where r is the radius of the tracker layer. The expected radiation dose and hadron fluence in radial layers of the CMS tracker are shown in Table 1.2 for different radii. It is worth mentioning that a few Grays of dose is lethal for human. One of the main challenges is to operate the tracker in such a harsh environment for an expected lifetime of 10 years at the full LHC luminosity 10^{34} cm^{2}s^{-1}. The radiation hardness, granularity and speed requirements favored devices based on silicon technology.

Table 1.2 Expected radiation dose and hadron fluence in radial layers of the CMS tracker for an integrated luminosity of 500 fb^{-1}, corresponding to the first 10 years of running. All particle fluences are normalized to 1 MeV neutrons ($n_{eq}cm^{-2}$).

Radius (cm)	Fast hadron fluence (10^{14} cm^{-2})	Dose (kGy)	Charged particle flux ($cm^{-2}s^{-1}$)
4	32	840	10^8
7	12	371	
11	4.6	190	
22	1.6	70	6×10^6
75	0.3	7	
115	1.2	1.8	3×10^5

The CMS inner tracker system [17] layout is shown in Fig. 1.6. The pixel detector is the innermost part. Following the pixels there is a silicon strip detector (r > 20 cm). The pixel detector is explained in detail in Chapter 2.

The three pixel and ten strip layers can provide thirteen measurement points per track. There are two pixel and twelve strip end cap disks on either end of the detector. The total pseudorapidity coverage is $|\eta| = 2.4$. The transverse momentum resolution of the tracker as a

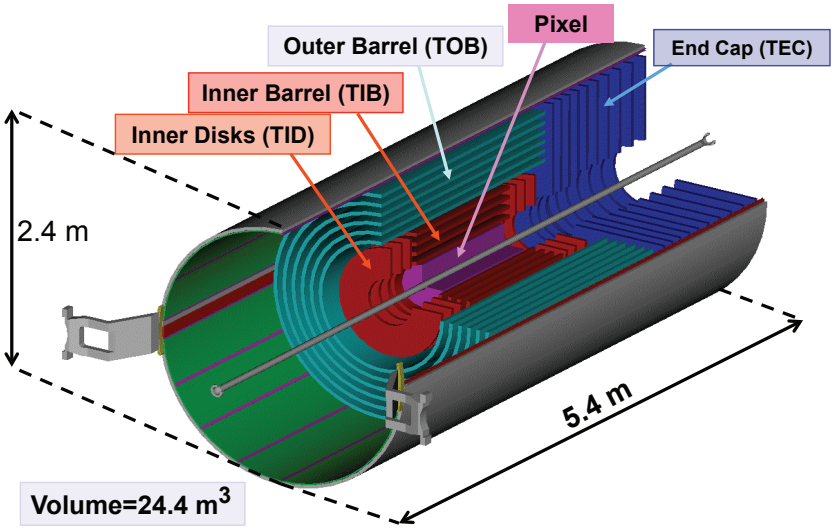

Figure 1.6 The CMS tracker layout overview.

function of η is illustrated in Fig. 1.7.

1.3.3 Electromagnetic calorimeter

An electromagnetic calorimeter (ECAL) is used to measure the energy and direction of electrons, photons, and jets. Measurements with very high precision are required. The CMS ECAL is made of lead-tungstate ($PbWO_4$) crystals. The high density of the crystals (8.2 g/cm^3) leads

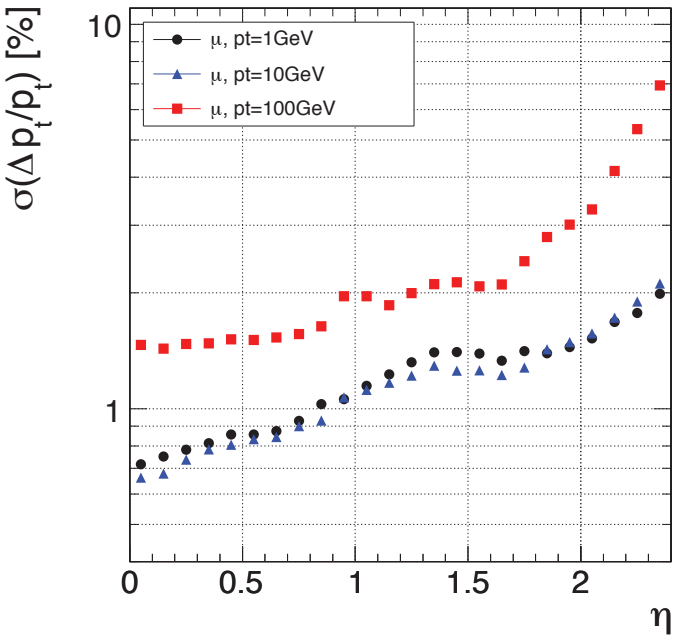

Figure 1.7 Transverse momentum resolution for muons with transverse momenta of 1, 10, and 100 GeV, as a function of η [18].

to a short radiation length and narrow showers, which allow for a compact calorimeter inside the solenoid that is fast, has fine granularity, and is radiation resistant [19]. The ECAL pseudorapidity coverage is $|\eta| < 3$. Particle induced scintillation light is detected by silicon avalanche photodiodes (APDs) in the barrel region and vacuum phototriodes (VPTs) in the end cap region.

1.3.4 Hadronic calorimeter

Similar to the ECAL the aim of the hadronic calorimeter (HCAL) is to measure the energy and the direction of strongly interacting particles and jets as well as missing transverse energy. The CMS HCAL [20] surrounds the ECAL. It has a sandwich structure of brass absorbers and plastic scintillators. The reason for choosing these materials is that they have smaller radiation lengths which minimize multiple scattering for traversing muons. The hadron barrel and end caps cover the range $|\eta| < 3$ with higher granularity. There are additional scintillators installed inside the muon barrel layer and steel-quartz fibers in the very forward region providing overall pseudorapidity coverage of $|\eta| < 5$.

1.3.5 Muon system

Muons have a relatively long lifetime of 2.2 μs. They interact weakly with matter and are not stopped by the calorimeters where they deposit some of their energy. The CMS muon detectors therefore are the outermost sensitive devices in the experiment [21]. The muon detectors are divided into a barrel and two end cap regions. The system utilizes three different

technologies: drift tubes (DT) in the barrel region, cathode strip chambers (CSC) in the end-cap region and resistive plate chambers (RPC) in both barrel and end-cap regions. The RPCs provide a trigger signal while DT and CSC detectors can reconstruct the muon trajectory and momentum. The muon system covers the region $|\eta| < 2.4$. The muon system is important for muon identification. For transverse momenta below 200 GeV the muon identification relies on the inner tracker.

1.3.6 Trigger system

The CMS trigger system has a two step decision system after which events will be recorded. The first trigger level, Level 1, decreases the event rate from 40 MHz to 100 kHz. The Level 1 is implemented in hardware and its decision takes 3.2 μs. This level requires information from the calorimeters and the muon detectors. The second level is known as High Level Trigger (HLT). The HLT is implemented in software. It uses the data from all CMS subdetectors. The event rate is reduced to 150 Hz at this level.

1.4 Motivation for this thesis

The pixel detector (Chapter 2) is the innermost device of the CMS experiment. This detector is used for precise track reconstruction due to its high granularity and good spatial resolution. However, in the harsh LHC radiation environment with large track multiplicities the pixel device performance is a big challenge. The expected radiation fluences in the CMS pixel barrel layers are given in Table 1.3. The CMS pixel sensors are specified to operate up to a irradiation fluence of 6×10^{14} $n_{eq}cm^{-2}$. From Table 1.3 it can be calculated that the innermost layer will be exposed to a radiation fluence of 6×10^{14} $n_{eq}cm^{-2}$ after the first four years of LHC operation. After this irradiation fluence the innermost pixel detector layer replacement is foreseen due to unavoidable damages in the silicon lattice resulting in degradation in pixel sensor performance. In particular, the particle hit resolution will decrease with radiation damage.

Table 1.3 Expected radiation fluences in the CMS pixel barrel layers at low and full LHC luminosities.

Radiation fluence (10^{14} $n_{eq}cm^{-2}yr^{-1}$)		
Radius (cm)	Low luminosity (10^{33} $cm^{-2}s^{-1}$)	Peak luminosity (10^{34} $cm^{-2}s^{-1}$)
4	1	3
7	0.4	1.2
11	0.2	0.6

The pixel sensor characteristics, in particular charge collection efficiency, signal-to-noise ratio, and position resolution have to be measured before and after irradiation as a function of irradiation fluence, and pixel readout threshold. Furthermore the hit reconstruction algorithms have to be investigated. Testing these algorithms will be helpful to understand the uncertainties

in determining the position resolution after irradiation. A correction is required to reduce the systematic uncertainties due to the radiation damage.

In this thesis, a simulation has been performed to study the particle hit resolution before and after irradiation. Two important hit reconstruction algorithms will be discussed. The so called eta-correction is used to correct for systematic uncertainties due to the radiation damage. After testbeam measurement, the following properties of the CMS pixel barrel detector sensors were established in a 3 T magnetic field before and after irradiation for the first time with the final sensor dimensions and front-end electronics:

- charge collection efficiency,
- signal-to-noise ratio,
- position resolution as a function of irradiation fluence, and
- position resolution as a function of pixel readout threshold.

Finally, the simulation and beam test results for the position resolution as a function of irradiation fluence and as a function of pixel readout threshold will be compared. The comparison results will be presented.

2 The CMS Pixel Detector

The pixel detector is the innermost subdetector of the CMS experiment. It is a part of the CMS tracking system. The pixel detector is used for precise track reconstruction. Because of multiple scattering at the pixel detector layers and the intrinsic detector resolutions the track reconstruction does not point to the decay vertex but to a shifted point. This shift is the impact parameter. In order to reduce the impact parameter the tracking devices have to be as close as possible to the vertex. Furthermore, high track multiplicity at the interaction point favors a pixel system with its high granularity, radiation resistant and good spatial resolution. The impact parameter and secondary vertex measurements are essential for many interesting physics studies. In this chapter the pixel barrel system on which I worked is reviewed briefly. Power and cooling are also briefly presented.

2.1 Detector overview

The pixel system has three barrel layers (BPix) with two end cap disks (FPix). The 53 cm long BPix layers will be placed at radii 4.4, 7.3 and 10.2 cm. FPix disks have radii between $\approx$ 6 and 10 cm and are located in the forward direction at $z = \pm 34.5$ and $z = \pm 46.5$. There are 48×10^6 pixels in BPix and 18×10^6 in FPix covering the total area of 0.78 m^2. The barrels and disks are shown in Fig. 2.1.

The pixel sizes in the transverse axis ($r\phi$) is 100 μm and 150 μm in the longitudinal axis. The pixel thickness is 285 μm. The pixel sensors are grouped in modules. In barrel the region the electron drift direction is perpendicular to the magnetic field. Therefore the Lorentz force distributes electrons over two or more pixels resulting in better position resolution. The forwards disks are tilted by 20° to have charge sharing. There is a secondary Lorentz effect in the forward disks but it is around few microns. Due to the charge sharing between adjacent pixels 15 μm position resolution is achievable in both BPix and FPix. For the rest of this thesis only the BPix detector issues are discussed. The FPix are in the responsibility of the US CMS Forward Pixel Collaborators [1].

2.2 The barrel pixel system

The barrel pixel system is installed inside the silicon strip detector. It has a cylindrical support structure with the supply tubes on both sides. The barrel length is 53 cm and 505 cm including the support structure. The supply tubes provide services such as power and cooling to the barrel and they hold electronic equipment for the readout and control. The detector modules are installed on the support structure. The assembled pixel detector is shown in Fig. 2.2.

The pixel sensors are assembled into modules. There are two types of modules, one is the half module consisting of 8 readout chips and the other is the full module consisting of 16

[1] The US CMS Forward Pixel Collaboration http://www.uscms.org/

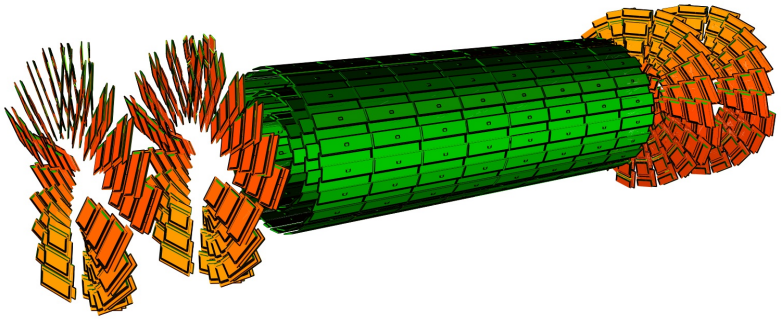

Figure 2.1 The CMS pixel detector layout.

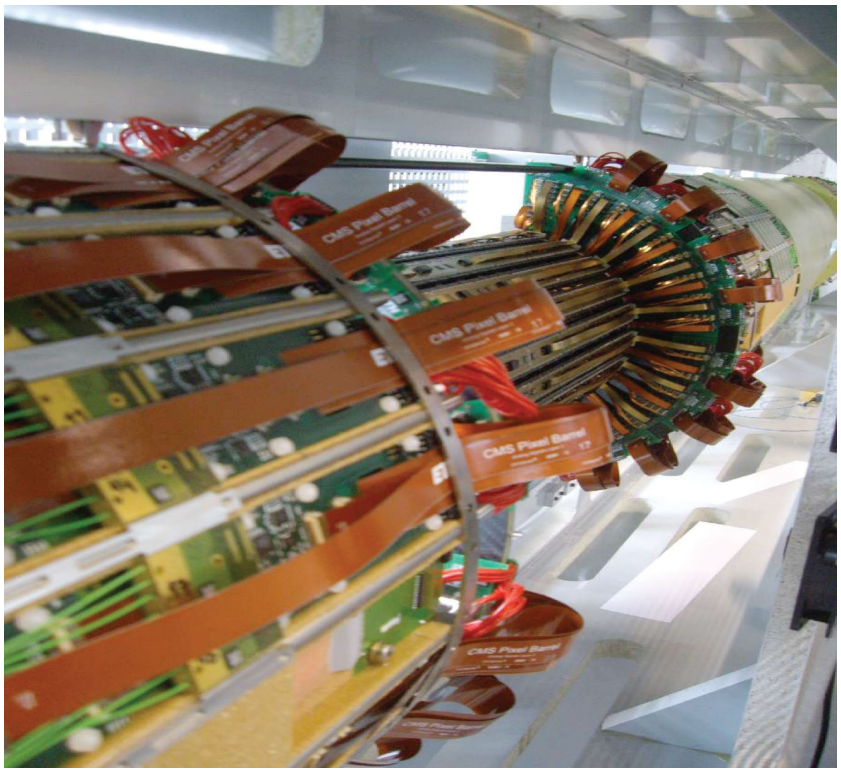

Figure 2.2 Assembled pixel barrel detector (middle) and supply tubes on both sides.

readout chips. The half modules are located at the edges of the barrel half shells in order to provide two half shell connection with no gap. The readout chips are bump bonded to the pixel sensors with 80×52 pixels of size 100×150 μm^2 each. A module has dimensions 66.6 mm in length and 26 mm in width. It weighs 3.5 g including both the Kapton and the power cables. The power consumption is 125 mW per readout chip, approximately 30 μW per pixel sensor and 2 W per module.

The pixel barrel mechanic support and supply tubes are machined at the University of

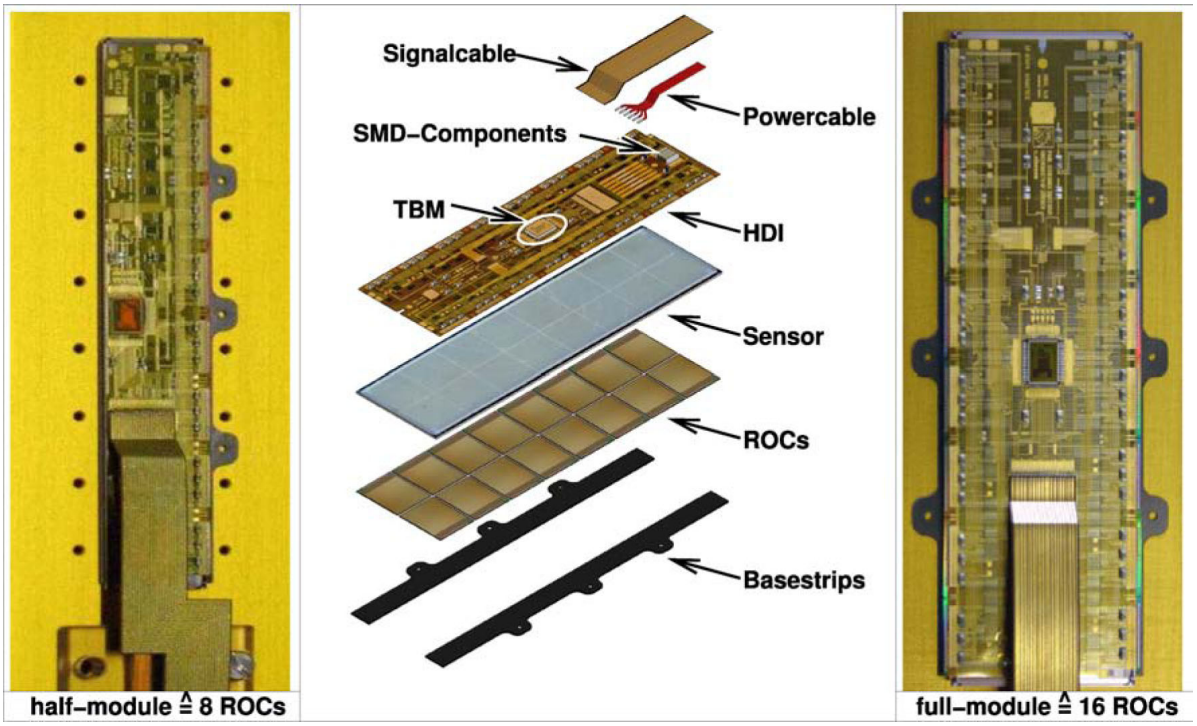

Figure 2.3 Exploded view (middle) of the barrel pixel detector full module (right) and picture of an assembled half module (left).

Zürich [2]. There are 800 half and full barrel modules assembled installed on the support structure at PSI [3]. The module assembly including several qualification tests are described elsewhere [22].

A module is composed of the following items (see Fig. 2.3):

- **Readout chip (ROC):** The signals are read out by ROCs which are bump bonded to the pixel sensors. A ROC, which is a standard ASIC technology in a commercial 0.25 μm five metal layer CMOS process, has 52×80 pixels with a pixel size of 100×150 μm^2 [23]. The ROC is explained in detail in Section 2.2.2.

- **High Density Interconnect (HDI):** It is a low mass, flexible printed circuit board. The control and power signals are distributed by the HDI to the readout chips and the TBM. The HDI has three metal layers. The top and middle layers are used for the delivery of the signals.

- **Token Bit Manager (TBM):** The TBM [24] controls the read-out of several ROCs. The data is transferred from the TBM to the FED via an optical link. The TBM token bits control the sequential read-out by passing from ROC to ROC.

- **Base stripes:** They are used for mechanical stability and as a contact between the module and the cooling structure. The base stripes have dimensions of 65×26 mm^2 and

[2]Physik Institut, Winterthurerstr. 190 CH-8057 Zürich, Switzerland.
[3]Paul Scherrer Institut, Villigen PSI, CH-5232 Villigen, Switzerland.

have a thickness of 250 μm.

- **Kapton cable:** The control and analog signals are transferred over the Kapton cable. It has a solid copper layer on its back side to suppress any crosstalk. The Kapton cable thickness is 170 μm.

- **Power cable:** The analog, digital and bias voltages are supplied by the power cable.

Bumb bonds are connected to the related sensors via an indium ball. The indium bumps have a diameter of 20 μm (see Fig. 2.4). The bump-bonding technique is used because there is no standard industrial process available for a ROC pitch below 100 μm.

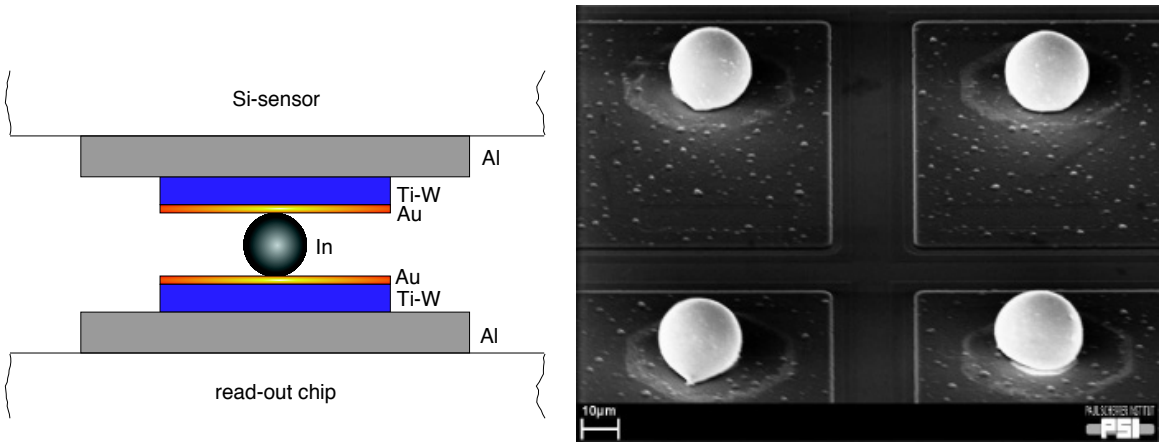

Figure 2.4 Cross section through the indium bump and related metal layers (left) and a scanning electron micrograph of a readout chip with the indium bumps (right).

2.2.1 Silicon sensors

The pixel detector sensors have to withstand a harsh radiation environment since they are close to the interaction point. The radiation is the main issue since it affects substantially the behavior of the silicon sensors. The sensors will be operated at $-10°$C before and during data taking to prevent leakage current which increases when irradiation increases.

The CMS pixel detector adopted the n-on-n technology concept, high dose n-implants (n^+) on a high resistive n-substrate as active volume. The n-type silicon has a resistivity of 3.7 kΩcm. The pn junction is realized by a high dose p-implant back contact to the n-substrate. For the CMS pixel barrel sensors the moderated p-spray design was chosen [25] (see Fig. 2.5). Each sensor has dimensions of 100×150 μm^2 and a thickness of 285 μm. The interpixel isolation is realized by using high dose p-implants (p^+). The gap between the n-implants is kept to 20 μm, in order to achieve homogeneous electric field across the sensor resulting in a relatively high capacitance ($\approx$ 80-100 fF per pixel). The full depletion voltage is around 70 V. This design allows operation even after high irradiation up to 10^{15} $n_{eq}cm^{-2}$ [26]. The pixel sensors are surrounded by several guard-rings to prevent any voltage breakdown. In order to ensure electron collection at high bias voltages ($<$ 600 V) after severe radiation fluences and to allow keeping guard rings at ground potential, the double sided processing was chosen.

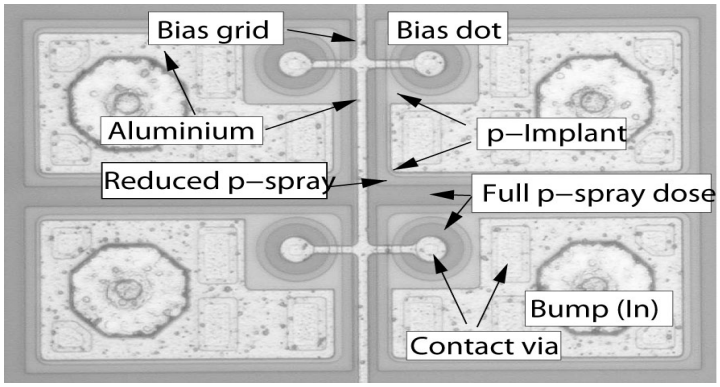

Figure 2.5 Picture of the moderated p-spray sensor. The indium bumps are already deposited but not yet reflown. Each bump is roughly a 50 μm wide octagon.

2.2.2 Readout chips

The ionization charge of the CMS pixel sensors are read out by the ROC of the type PSI46v2 at the LHC bunch crossing frequency of 40 MHz. These signals are kept in the ROC during the CMS Level-1 trigger latency. The ROC has an active area with one pixel unit cell (PUC) per pixel sensor to read out the collected charge, and the periphery with the control interfaces and data buffers to store the particle hit informations in data buffer [23]. In a ROC, there are 26 double columns and 80 rows in the active area to read out 4160 pixels in total. Each sensor is connected to a PUC via a bump bond. The collected ionization charge after the passage of a particle induces a voltage signal in the PUC. The signal is amplified. If the amplified signal is over the pixel threshold, the corresponding double column periphery is informed. Then this periphery starts to store the particle hit informations such as the position of the hit, collected charge, and the bunch crossing in data buffers. Depending on the received trigger signal this hit is accepted or rejected. If it is accepted, the hit information is added to the analogue signal.

Each ROC behavior is controlled by 26 digital to analog converters (DACs) and 3 registers. The functionality of these DACs and their optimization are given in [27]. As shown in Fig. 2.6, there is a switch labelled *enable* to able or enable a pixel. If the switch is closed then corresponding pixel is enabled. The electrical calibration signal is sent to enabled pixels.

The $Vcal$ DAC register controls the amplitude of the internal calibration signal. The internal calibration signal timing/delay is done by the $CalDel$ DAC register. The preamplifier and the shaper receive the sensor or internal calibration signal. Comparator compares the signal amplitude and the reference voltage which can be tuned by the $VthrComp$ DAC register. If the amplitude exceeds the reference voltage, the hit is generated. *Trimming* is done by four trim bits. The fine tuning of the threshold for each pixel is done by four trim bits. They lower the pixel threshold depending on the $Vtrim$ DAC register value. The *maskbit* disables the comparator of a pixel. The pulse height sampling time is defined by the $VhldDel$ DAC register. When the signal amplitude is higher than the reference voltage, the pixel is enabled by closing the *send* switch. Then the double column periphery is informed that a hit is generated.

The actions to be taken to produce and read out a hit in a pixel are:

- The double column of the pixel has to be enabled.

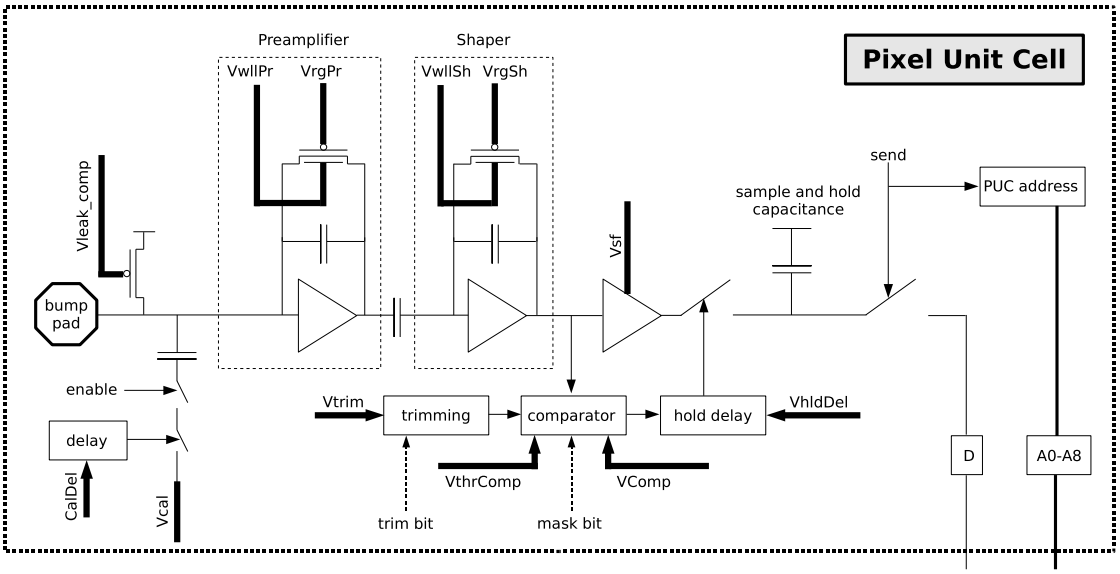

Figure 2.6 Overview of the PUC functionality [27]. Details are explained in the text.

- The calibration injection to the pixel has to be enabled.
- The readout of the pixel has to be enabled.
- A calibration signal has to be sent to the module.
- A trigger signal has to be sent to the module.

2.2.3 Readout system

The control and readout system for the pixel detector is shown in Fig. 2.7 [28]. The system has three parts. These are: (1) a read-out data link from the modules/disks to the pixel front end driver (pxFED), (2) a fast control link from the pixel front end controller (pFEC) to the modules/disks and (3) a slow control link from the FEC to the supply tube/service cylinder.

Basically, the data is transfered from the front-end electronics to the FED. The control signals are transmitted from the FEC to the front-end electronics. Both the FEC and FED are placed in the electronics control room, which is 100 m far away from the detector, and communicate to the front-end electronics via 40 MHz optical links.

Front End Driver (FED): The ROC optical signals are digitized by the pixel Front End Digitizer (pxFED).

Front End Controller (FEC): The trigger and clock information is provided by the pixel Front End Contoller (pFEC) to the front end. The pFEC delivers a data path to the front end in order to handle configuration settings via a fiber optic connection.

The detector front end control system: There are four communication and control unit boards (CCU boards) in the CMS pixel detector for the BPix systems. Each CCU board controls a quarter of the pixel detector with eight barrel read-out sectors.

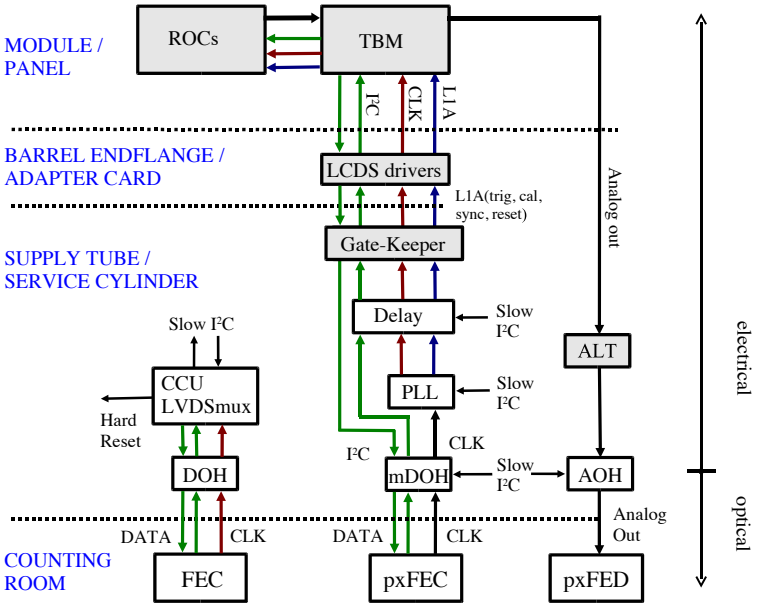

Figure 2.7 Pixel control and read-out system block diagram.

2.2.4 Power and cooling

The CAEN-EASY4000 commercial modular system is used to generate the required power for both high and low DC voltages. The main system has a main controller containing 3 branch controller and it is located in the detector control room (USC55). Since the actual power supply cards are radiation hard and magnetic field resistant they are placed in two racks of 5 crates close to the detector which reduces power loss in the cables. The power supply crates are connected to the branch controller via 100 m flat cables. Each crate has two types of electronics cards. One with 4 channels of 2.5V/7A feeding the service electronics and the other has 2 channels of each with 2 low (1.75 V/7 A and 2.5 V/15 A) and high (600 V/20 mA) voltage lines for ROC and sensor biasing.

A single pixel power consumption is approximately 55 μW. This includes 13 μW for the pixel leakage current after irradiated to a fluence of $\Phi = 5.9\times10^{14}$ $n_{eq}cm^{-2}$. The total 66×10^6 pixels consume approximately 3.6 kW power. The sensors will be kept at $-10°$C. The liquid C_6F_{14} is used for cooling. The aluminum cooling tube power load is about 50 W/m. Therefore a total flow rate of 1 ℓ/s is required to keep the temperature of the cooling tubes below 2°C.

3 Semiconductor as ionizing radiation detectors

Silicon detectors are widely used in high energy physics experiments. They can detect crossing charged particles by the energy that these particles release, producing free charge carriers. In the presence of an electric field, the free charge carriers generated during the ionization process drift to the detector's electrodes inducing a signal, thus testifying the passage of the particle. In this chapter, the *pn* junction formation, the ionization energy loss of charged particles, a simple signal acquisition system are reviewed. In addition the main radiation damage mechanisms in silicon, and leakage current issues are discussed.

3.1 Semiconductor pn junction

A semiconductor junction is obtained by bringing together p-type and n-type semiconductor resulting a good thermal contact. P-type semiconductors are obtained by doping silicon with acceptor impurity atoms and n-type with donor impurity atoms. These junctions have a diode characteristic, which means that the current flows in one direction.

Once the contact is established between p- and n-type semiconductors, the excess electrons in the n-side diffuse into the p-side while the excess holes in the p-side diffuse into the n-side. Thus en excess amount of positive charge will be created in the n-side while negative charge in the p-side. At thermal equilibrium, the total electrostatic potential difference in between is called *built-in potential* V_{bi}. While the holes (electrons) are diffusing, some of the negative (positive) acceptor (donor) ions ($N_{A(D)}$) near the p-side (n-side) are left uncompensated since the number of acceptors (donor) are fixed in the semiconductors. Therefore an electric field is created. Due to this electric field a zone around the interface becomes free of mobile charges (*depletion zone*). The electric field counteracts the diffusion and prevents further movement of the charge carriers. Diffusion and drift currents are in opposite directions which means the net electron and hole currents will be zero on the borders of the depleted region (see Fig. 3.1).

The total depletion layer width, w, as a function of the V_{bi} can be calculated as

$$w = \left[\frac{2\epsilon_s}{q} \left(\frac{N_A + N_D}{N_A N_D} \right) V_{bi} \right]^{\frac{1}{2}} \tag{3.1}$$

where ϵ_s is the permittivity of silicon (1.05×10^{-10} A s $(\mathrm{Vm})^{-1}$) and q is the elementary electric charge.

The width of an intrinsic depletion region is in the order of 10μm corresponding to a V_{bi} ≈ 0.5 V. This width is not sufficient for the detector applications. Therefore larger depletion width is realized by applying a *reverse bias voltage* V_{bias} across the junction. In the reverse bias case, the $-V_{bias}$ is applied on the p-side and $+V_{bias}$ on the n-side. Since $w \propto \frac{1}{N_A, N_D}$, w can be wider if the concentration of one side of the junction is much larger. For instance, if $N_A >> N_D$ then w on the p-side is much smaller than the one on the n-side. That leads to the

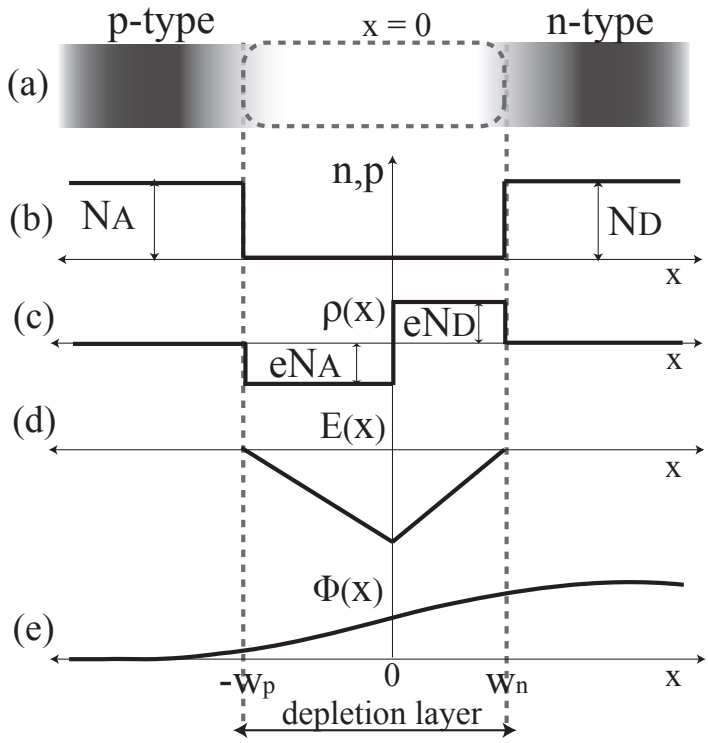

Figure 3.1 (a) Schematic view, (b) densities of donor and acceptor ions, (c) charge distribution, (d) electric field and (e) electrostatic potential distribution of a pn junction.

depletion width on the n-side (x_n) is much larger then the one on the p-side (x_p). Therefore w becomes

$$w \cong x_n = \left[\frac{2\epsilon_s \left(V_{bi} \pm V_{bias}\right)}{qN_{eff}}\right]^{\frac{1}{2}} \quad with \quad N_{eff} = |N_D - N_A| \tag{3.2}$$

where $+(-)V$ is for the reverse (forward) bias and the junction resistivity becomes

$$\rho = \frac{1}{q(\mu_n N_D + \mu_p N_A)} \approx \frac{1}{q\mu_d N_D} \tag{3.3}$$

where $\mu_{n(p)}$ is the electron (hole) mobility.

To fully deplete the junction the full depletion voltage, V_{FD}, will be

$$V_{FD} = \frac{qN_{eff}d^2}{2\epsilon_s} \tag{3.4}$$

where d is the junction thickness. For example, the CMS pixel barrel sensors reach the full depletion at 70V bias voltage. Typical resistivities for the sensors in high energy physics experiments are in the order of a few kΩcm.

3.2 Ionization energy loss in semiconductor detectors

When a charged particle passes through matter it interacts with its constituents via the Coulomb force. The two most important processes taking place are the elastic scattering on nuclei in which the particle is deflected from its incident direction, and the electromagnetic interaction in which the particle releases its energy due to the inelastic collisions with the atomic electrons of the material. As a result, the excited electrons transit to the conduction band where they behave as free carriers, leaving holes which are missing electrons, in the valance band.

The mean energy loss dE per length dx of a charged particle due to the ionization mechanism is given by the Bethe-Bloch formula [4]

$$-\frac{dE}{dx}[MeV/cm] = 2\pi N_A r_e^2 m_e c^2 \rho \frac{Z}{A}\frac{z^2}{\beta^2}\left[\ln\left(\frac{2m_e c^2\beta^2\gamma^2 E_{kin}^{max}}{I^2}\right) - 2\beta^2 - \delta\right] \tag{3.5}$$

where
N_A - Avogadro number
r_e - Classical electron radius
m_e - Electron mass
c - Speed of light
z - Charge of incident particle in units of elementary charge
Z, A - Atomic number and atomic weight of the absorbing material
ρ - Mass density of the absorbing material
I - Mean excitation energy of the absorbing material
E_{kin}^{max} - Maximum energy transfer in a single collision
β - $\frac{\upsilon}{c}$ of the incident particle
γ - $[1-\beta^2]^{-\frac{1}{2}}$
δ - Density correction: $\delta \approx ln\gamma + \zeta$, where ζ is a material constant.

The mean energy loss of a proton is shown in Fig. 3.2 as a function of its momentum neglecting the density effect δ.

The density correction has an important contribution to the energy loss of the incident particles. This effect appears at very high energies (ultra relativistic particles), because at high energies the electric field of incident particles polarizes atoms along their paths. This polarization reduces the energy loss contribution of the electrons far from the particle path. The δ is proportional to the density of materials.

At non relativistic energies, the mean energy loss is inversely proportional to the kinetic energy (velocity squared). At $\beta \approx 0.96$ the minimum energy loss is reached and the particles releasing such energies are called *minimum ionizing particles* (MIP). For example, for the 285 μm thick CMS pixel sensor a MIP corresponds to a ionization charge of 24'500 electrons at room temperature. As the energy increases the term $\frac{1}{\beta^2}$ becomes constant which increases the dE/dx due to the logarithmic dependence in Eq. 3.5. This relativistic rise is partially canceled by the density correction.

3.3 Charge carrier transportation in semiconductors

In semiconductors the charge transportation mainly occurs as diffusion and drifts. In the absence of electric field, electrons move randomly in all directions. Therefore the total momentum is lost due to lattice collision in silicon. The charge carriers are diffused from a high

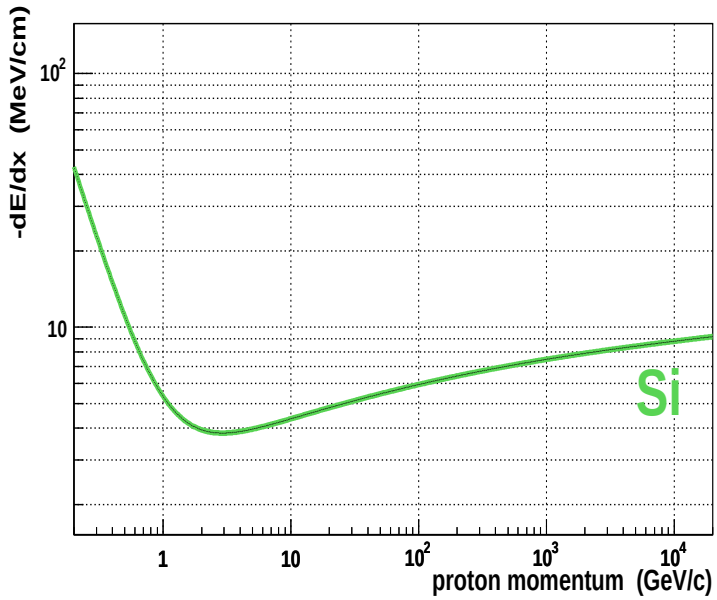

Figure 3.2 Mean energy loss of a proton in silicon as a function of proton momentum [29].

concentration region to a low concentration region. The electron diffusion D_n for electrons (holes D_p) are expressed by the Einstein relation which is

$$D_{n(p)} = \left(\frac{k_B T}{q}\right) \mu_{n(p)} \tag{3.6}$$

where k_B is the Boltzman constant. The electron (hole) charge carrier density is given by

$$\sigma_{n(p)} = \sqrt{2 D_{n(p)} t_{n(p)}} \tag{3.7}$$

where $t_{n(p)}$ is the drift time of electrons (holes).

The charge drift occurs in the presence of an external electric field. When the electric field is applied to silicon junction ionized electrons will be drifted along the field. The drift velocity of electrons (υ_n) and holes (υ_p) which are electric field dependent

$$\upsilon_n = \mu_n E, \quad \upsilon_p = \mu_p E \tag{3.8}$$

where $\mu_{n(p)}$ is the mobility of electrons (holes). The empirical formula for the mobility dependence on the electric field at temperature T can be found in [30]

The total drift force $\vec{F}$ acting on a charged particle in the presence of constant electric ($\vec{E}$) and magnetic ($\vec{B}$) fields is

$$\vec{F} = q \cdot (\vec{E} + \vec{v} \times \vec{B}) \tag{3.9}$$

where $\vec{v}$ is the velocity of the charge carriers.

If the magnetic field is perpendicular to the electric field, the carriers drift at an angle which is known as *Lorentz angle* θ_L:

$$\tan \theta_L = \mu_H \cdot |\vec{B}| \tag{3.10}$$

where μ_H is the Hall mobility.

3.4 Signal acquisition

Once the signal charge carriers are produced in the presence of a charged particle passing through the silicon sensor, they are collected and amplified. This operation is usually done by a *charge sensitive amplifier*.

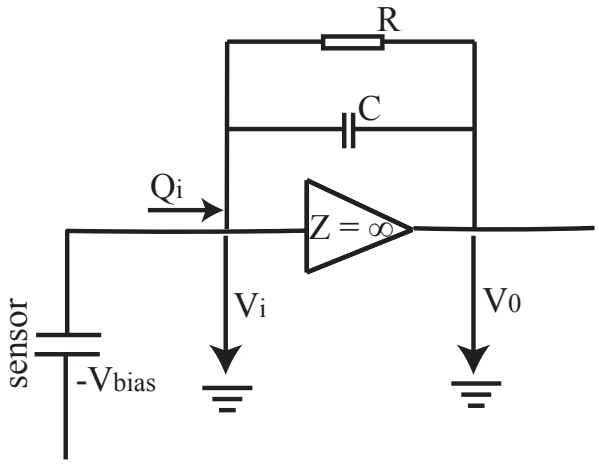

Figure 3.3 Block diagram of a charge sensitive amplifier.

A charge sensitive amplifier is shown in the Fig. 3.3. Basically, it consists of amplifier, a resistor R, a capacitor C. This circuit is attached to the sensor to collect the ionized charges. The charge is accumulated on a capacitor. Since the impedance of the amplifier Z is assumed to be infinite, the input charge Q_i is equal to the charge collected on the capacitor Q_C. Defining the amplifier voltage gain A as the ratio between the output voltage V_o and the input voltage V_i one can calculate the effective input capacitance C_i as

$$C_i = \frac{Q_i}{V_i} = C(-\frac{V_o}{V_i} + 1) = C(A + 1) \quad \text{with} \quad \mathrm{A} = -\frac{\mathrm{V_o}}{\mathrm{V_i}}. \tag{3.11}$$

The effective input capacitance provides the charge gain A_Q

$$A_Q \equiv \frac{V_o}{Q_i} = \frac{AV_i}{C_i V_i} = \frac{A}{Ci} = \frac{A}{(A+1)}\frac{1}{C}. \tag{3.12}$$

Eq. 3.12 becomes $A \approx 1/C$ for high voltage gains. The system has to be reset after each charge integration to be ready for the next event. The reset process (i.e. capacitor discharge) is done by the resistor R.

The choice of R value is a very important because it has to provide:

- The capacitor to be able to collect charges without signal cut-off by the resistive feedback (lower boundary),
- No event pile-up effect happens (upper boundary). Pile up occur with high pulse frequencies, when the capacitor is not fully discharged at the arrival of a new signal pulse.

3.5 Radiation damage in silicon

Radiation damages in semiconductor devices are one of the limiting factors in high energy detector applications. Silicon device behavior after high radiation doses was studied by several research and development projects (e.g. [31]).

In a radiation environment incident particles displace lattice atoms producing defects giving rises to new energy levels in the band gap. These new levels change several material properties. Therefore radiation in silicon has the following effects:

- it changes the effective carrier concentration resulting higher necessary bias voltages to deplete the silicon device (see Eq. 3.4),
- it increases the leakage current due to produced trap centers in the silicon band gap, and
- it reduces the charge collection due to charge carrier trapping hence deterioration in charge collection efficiency.

There are two main radiation damages in semiconductor devices. They are divided into bulk and surface defects. The former one is explained by the non-ionizing energy loss (NIEL) hypothesis ([31]). The latter one is due to changes in silicon-silicon oxide interface. Both effects are discussed briefly in the following sections.

3.5.1 Bulk defects

Two processes occur when particles enter a solid material. Energetic particles loose their energy via ionizing and non-ionizing processes as they pass through a given material. After these processes the resulting products are electron-hole pairs (ionization) and displaced lattice atoms (non-ionizing). At the first instance displacement damage is due to atomic vacancies and interstitials. Basically, a vacancy is the absence of an atom from its normal lattice position. If the atoms move further into non-lattice positions they are called interstitials. Displaced atoms can move several hundred angstroms through the silicon lattice. Vacancies and interstitials can combine producing so-called *Frenkel pairs*. The displacement can occur locally with many vacancies, giving rise to defect complexes. The radiation induced defects alter the optical and electrical properties of silicon devices. The damage depends on the nature of the defects and on the time after creation at a given temperature. Defect reordering is also temperature and excess carrier concentration dependent. Defect reordering is known as *annealing*. Annealing is a damage reducing effect. In addition, annealing can also lead to more stable defects at higher temperatures. This effect is known as *reverse annealing*.

Increasing fluence [1] Φ has effects on the macroscopical performance of the silicon device. These effects are leakage current and doping concentration. The leakage current increases linearly with increasing Φ and the following linear relationship holds between Φ and the current increase ΔI [32]

$$\Delta I_{vol} \equiv \frac{\Delta I}{V} = \alpha \cdot \Phi \tag{3.13}$$

where V is the volume of the silicon device, α is the leakage current damage rate. The RD48 (ROSE) collaboration at CERN derived the leakage current damage rate for irradiated silicon sensors as

[1] Accumulated particle flux.

$$\alpha = (3.99 \pm 0.03) \times 10^{-17}\mathrm{Acm}^{-1}$$

after 80 minutes annealing at 60°C [31].

The leakage current depends strongly on the temperature at which the silicon device operates. The proportionality relation between the leakage current and the operation temperature is

$$I(T) \propto T^2 \exp\left(-\frac{E_g}{2k_B T}\right) \tag{3.14}$$

where T is the operating temperature, E_g is the silicon band gap energy (1.12 eV) and k_B is the Boltzman constant. At -10°C, the leakage current is several times smaller than at room temperature. Both leakage current measurements and leakage current damage rate calculations are discussed in Chapter 5.

The effective carrier concentration N_{eff} (see Eq. 3.2) is reduced due to radiation damages. One can see clearly the linear proportionality between the V_{FD} (see Eq. 3.4) and N_{eff} in Fig. 3.4. The higher the fluence, the higher the voltage for full depletion.

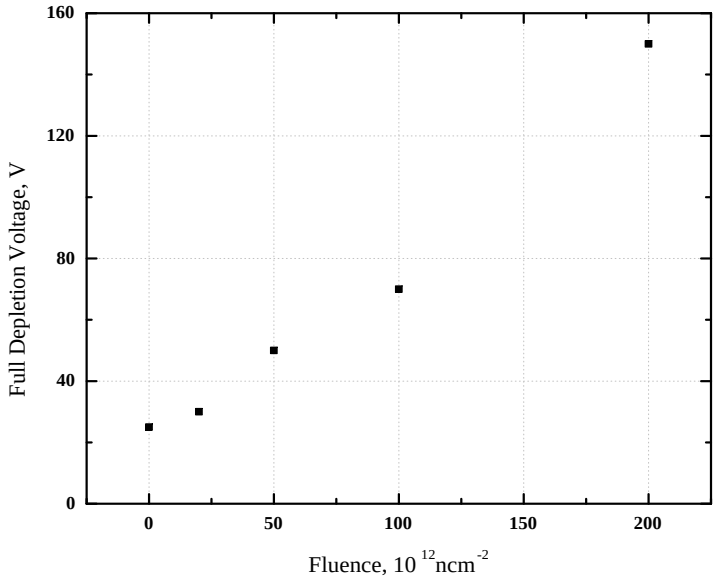

Figure 3.4 Full depletion voltage versus 10 MeV/c nuclear neutron fluences [33].

It has been found that silicon containing higher oxygen impurities has smaller leakage currents after irradiation. The oxygen impurity concentration does always exist in silicon but one tries to keep it as low as possible ($> 10^{15}$ cm^{-3}). Experimentally it was observed that a high oxygen concentration is reducing the radiation induced carrier concentration loss. The oxygen enriched silicon devices are as good as the best standard materials. There is no satisfactory explanation to this observation. This might be due to the fact that oxygen combines to vacancies forming electrically non-active complexes [34].

3.5.2 Surface defects

Surface defects have also important effects on the performance of silicon devices. These type of defects are located between the silicon bulk and the silicon-oxide layer. In comparison to

bulk defects they are non-uniformly distributed.

Following the passage of an ionizing particle, electron-hole pairs produced in the SiO_2 layer are drifted in the presence of an electric field. Due to their fast mobility [2] the electrons can escape from the silicon-oxide layer. The holes with lower mobility [3] cannot be swept out of the silicon-oxide layer. They are permanently trapped there leading to a constant positive charge layer which is very close to the SiO_2 layer. The positive layer induces a negative layer in the silicon bulk at the silicon-SiO_2 interface. The free electrons in the negative layers influence several parameters such as the maximum electric field, the implants, the inter-pixel resistance etc.

The radiation induced defects are also produced at the interface. These interface defects are due to bad wire bond or displaced silicon atoms close to the interface. They behave like bulk defects. The interface defects cause the *surface leakage current*. The surface defects are not severe compared to the bulk defects and the underlying physics has not yet been understood [35].

[2] The electron mobility is 20 $cm^2V^{-1}s^{-1}$.
[3] The hole mobility is 2×10^{-5} $cm^2V^{-1}s^{-1}$.

4 Simulation of irradiated pixel sensors

In this chapter a detailed simulation (PIXELAV) of the silicon pixel sensors for the CMS pixel detector is reviewed. This simulation is used to predict the effects of radiation damage on detector performance. The analysis of the simulated data is presented and the results for the position resolution are discussed.

4.1 PIXELAV simulation for irradiated pixel sensors

PIXELAV [36] is a detailed simulation tool used for the CMS pixel sensors. It is a very useful program for the fine-tuning of the sensor design, the development of more accurate reconstruction algorithms and the calibration of charge sharing functions. A continuous sensor position calibration is required as the pixel detector is increasingly damaged by radiation during operations.

The PIXELAV includes the following elements:

- a physical model of charge deposition,
- a realistic electric field map,
- charge carrier transport including mobilities,
- Hall effect and 3D diffusion,
- radiation damage and charge trapping effects,
- electronic noise, and front-end response.

The PIXELAV has two main simulation steps: electrostatic and electrodynamic. In the electrostatic simulation a realistic radiation damage model (see Section 4.1.3) including charge deposition is imported into the commercial ISE TCAD software [37] to produce a 3-D electric field map. In ISE TCAD, the electric field map is generated for the CMS pixel sensors with 100×150 μm^2 pixel cells and 285 μm thickness. The map is provided to the electrodynamic process which simulates charge transportation, charge trapping and the front-end electronics response.

The geometrical coordinates in the simulation are shown in Fig. 4.1. The magnetic field is along the 150 μm pitch and is perpendicular to the electric field causing the Lorentz drift along the 100 μm pitch.

4.1.1 Charge deposition and transport

Charge deposition by pions is simulated. The model is based on the π-e^- cross section which is computed elsewhere [38]. Cross sections for electrons between 1.8 eV and 1 MeV are integrated.

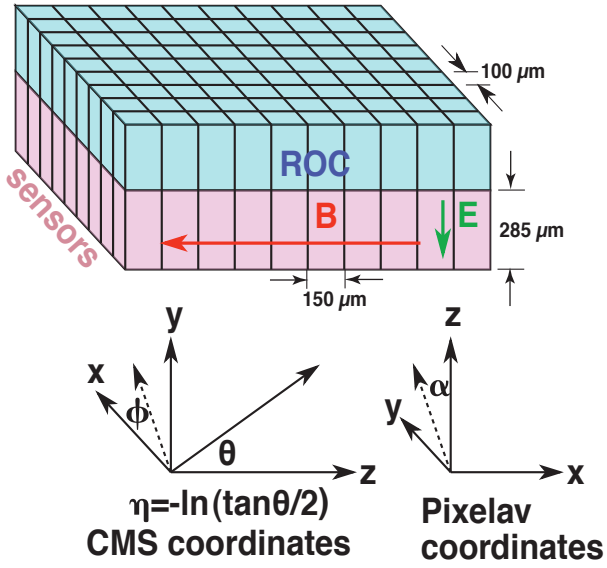

Figure 4.1 PIXELAV geometrical coordinates, pixel sensor and readout chip (ROC) drawing, and the CMS coordinates.

The electrons and δ-rays (recoil electrons) produce electron-hole carriers as they propagate through silicon. The δ-ray track length is chosen from the electron energy range relationship shown in Fig. 4.2. δ-rays continue propagating till they lose all their energy or leave the sensor.

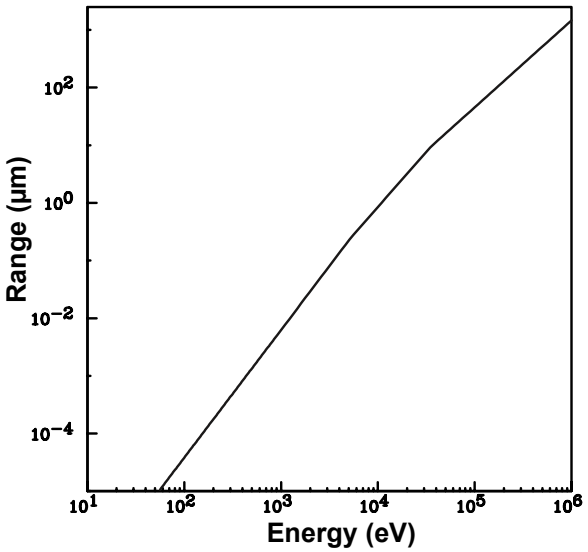

Figure 4.2 Range of a δ-ray of energy E in silicon [29].

Charge transport is the process by which electron and hole pairs drift towards the p^+ and n^+ implants in the presence of an internal electric field and an external magnetic field. The transportation is done by numerically integrating the equations of motion for the charge carriers,

$$\frac{d\vec{r}}{dt} = \frac{\mu\left[q\vec{E} + \mu r_H \vec{E}\times\vec{B} + q\mu^2 r_H^2(\vec{E}\cdot\vec{B})\vec{B}\right]}{1+\mu^2 r_H^2|\vec{B}|^2} \tag{4.1}$$

where $\mu(\vec{E})$ is the mobility (see Eq. 3.8), r_H is the Hall factor of the carriers, $q = \pm 1$ is the charge of the carrier, $\vec{E}$ is the electric field, and $\vec{B}$ is the magnetic field. The electron (hole) Hall factor is $r_H = 1.15$ (0.90). The electron and hole mobility parameters are taken from Ref. [39].

4.1.2 Signal induction

The integrated charge induced on the collecting electrode is computed by the image theory. The theory involves an infinite series of image charges on each side of the sensor for a given position of the charge carrier and considers the total flux crossing a given electrode due to the series of charges [40]. The implication of the image theory in PIXELAV is illustrated in Fig. 4.3 where the pixel sensor is represented as a parallel plate capacitor. In the sensor active area a produced electron induces an infinite series of image charges of both negative electrons e^- and positive holes h. Under the assumption that the sensor pitch P (transverse dimension) is much larger than its thickness t, the total induced charge Q_{tot} on the anode n^+ is given by

$$Q_{tot} = -q\frac{z}{t} \tag{4.2}$$

where the z is the distance of the induced electron from the cathode p^+, and q is the induced charge. At $z = 0$, Q_{tot} disappears because the opposite sign charges overlap. When $z = t$, Q_{tot} becomes -q. The charge -q is then removed from the readout preamplifier resulting in a $+q$ charge to be integrated. The transverse charge distribution on the anode is broad when the induced electron is close to the cathode side (dashed line in Fig. 4.3) and charge distribution becomes narrower as the induced charge approaches the anode (continuous line in Fig. 4.3). This effect occurs when charge traps are present within the sensor bulk, whereas in the absence of the trapped charge one counts the charge hitting the implants.

The PIXELAV output data gives the information of the coordinates of the pions and their directions, the produced electron-hole pairs, and two sets of signals for a 21×13 array of pixel signals.

The simulation of the electronics and readout system is performed by a separate code. This allows the electronic simulation to be changed without repeating the charge transport simulation. The electronics simulation is performed in two steps. In the first step, a 500-electron random noise signal is superimposed to each pixel signal. In the second step, the readout chip (ROC) response function is applied to the total signal. The ROC response function was measured during the CMS pixel testbeam in 2003/4 [41]. The digitized signal amplitude is shown in Fig. 4.4 as a function of input charge. A readout threshold of 2500 electrons is finally applied to the signal.

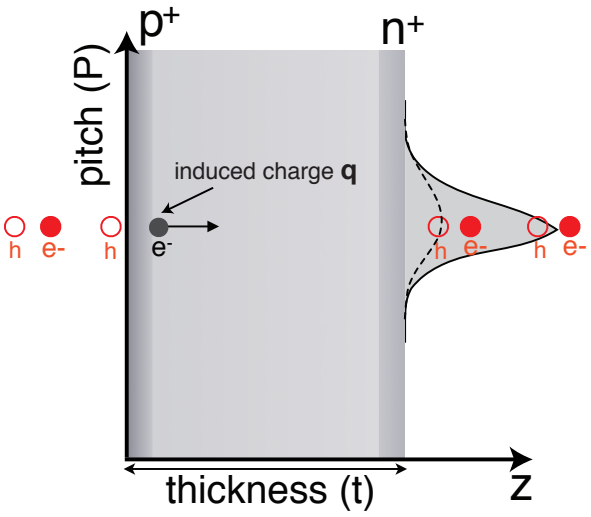

Figure 4.3 Several image charges produced by the induced electron (black solid dot). The image electrons are shown as red solid dots and holes are shown as red open dots. The transverse charge distribution on the anode n^+ is illustrated as the dashed (smaller z) and solid (larger z) curves.

4.1.3 Effective double-trap-model

In unirradiated sensors, the electric field varies linearly as a function of silicon sensor depth reaching a maximum at the *pn* junction. This is due to a uniform effective charge density ρ_{eff} (see Section 3.1) that varies in magnitude but remains uniform with irradiation. However, the CMS pixel testbeam measurements have shown doubly peaked electric field after heavy irradiation. The details about the testbeam measurements, data and experimental setup can be found elsewhere [41] (through this section all results are referenced to this paper). The measured charge collection profiles for an unirradiated and several irradiated sensors are shown in Fig. 4.5 as a function of the distance from the beam entry point. The measurements proves that the electric field does not vary lineary as a function of sensor depth but shows maxima at both p^+ and n^+ implants after irradiation.

One of the recent attempts to explain the double peak behaviour is the Eremin, Verbitskaya, and Li's (EVL) double trap model [42]. The model is a modified version of the Shockley-Read-Hall (SRH) statistics and it produces a space charge density ρ_{eff} from the trapping of charge carriers in the leakage current. In the EVL model, ρ_{eff} is defined as

$$\rho_{eff} = e\left[N_D f_D - N_A f_A\right] + \rho_{dopants} \tag{4.3}$$

where $N_{D(A)}$ is the donor (acceptor) trapping density, $f_{D(A)}$ is the occupied donor (acceptor) state fraction and $\rho_{dopants}$ is the ionized dopants charge density. The charge trapping occurs due to the generation and recombination processes. The $\rho_{dopants}$ expresses the material resistivity before irradiation. According to the standard SRH definitions, f_D and f_A can be defined as

$$f_D = \frac{\upsilon_h \sigma_h^D p + \upsilon_e \sigma_e^D n_i e^{E_D/kT}}{\upsilon_e \sigma_e^D \left(n + n_i e^{E_D/kT}\right) + \upsilon_h \sigma_h^D \left(p + n_i e^{-E_D/kT}\right)} \tag{4.4}$$

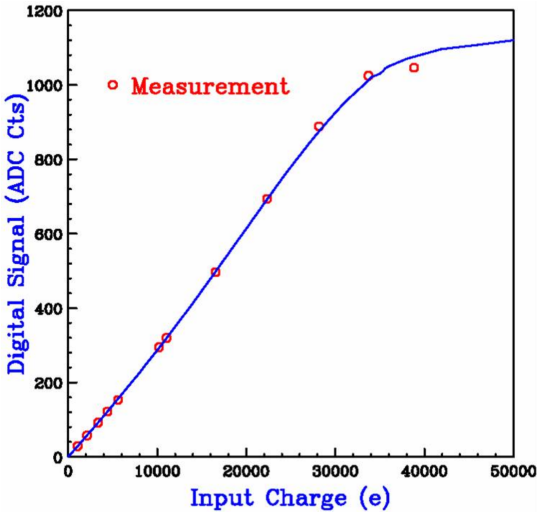

Figure 4.4 Measured calibration curve during the CMS pixel testbeam in 2003/4 (red circular points) [41]. The solid curve is a fit to the measured calibration function.

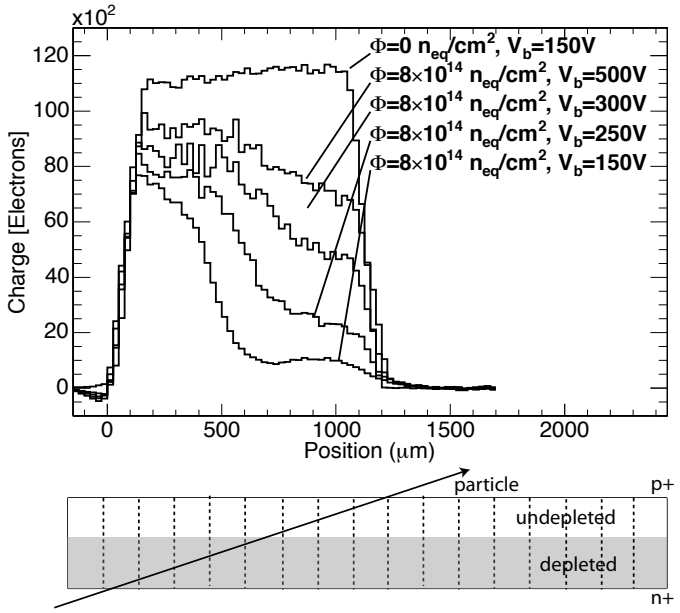

Figure 4.5 Measured charge collection profiles for an irradiated ($\Phi = 8{\times}10^{14}$ n_{eq}/cm^2) and an unirradiated sensor operated at several bias voltages [41].

$$f_A = \frac{\upsilon_e \sigma_e^A n + \upsilon_h \sigma_h^A n_i e^{-E_A/kT}}{\upsilon_e \sigma_e^A \left(n + n_i e^{E_A/kT}\right) + \upsilon_h \sigma_h^A \left(p + n_i e^{-E_A/kT}\right)} \tag{4.5}$$

where $\upsilon_{e(h)}$ is the termal speed of the electrons (holes), $\sigma_{e(h)}^D$ is the electron (hole) capture cross sections for the donor trap, $\sigma_{e(h)}^A$ is the electron (hole) capture cross sections for the acceptor trap, n (p) is the density of free electrons (holes), n_i is the intrinsic carrier density, $E_{D(A)}$ is the activation energy (with respect to the mid-gap energy level) of the donor (acceptor) states. The generation and recombination induced currents are determined by the SRH definitions as

$$\begin{aligned} U = & \frac{\upsilon_e \upsilon_h \sigma_e^D \sigma_h^D N_D \left(np - n_i^2\right)}{\upsilon_e \sigma_e^D \left(n + n_i e^{E_D/kT}\right) + \upsilon_h \sigma_h^D \left(p + n_i e^{-E_D/kT}\right)} \\ & + \frac{\upsilon_e \upsilon_h \sigma_e^A \sigma_h^A N_A \left(np - n_i^2\right)}{\upsilon_e \sigma_e^A \left(n + n_i e^{E_A/kT}\right) + \upsilon_h \sigma_h^A \left(p + n_i e^{-E_A/kT}\right)}. \end{aligned} \tag{4.6}$$

The physics of this model and its schematic drawing are shown in Fig. 4.6 and in Fig. 4.7 respectively. The ρ_{eff} and the electric field are illustrated as a function of the sensor depth (z) for the double trap model which is tuned to reproduce the $\Phi = 5.9{\times}10^{14}$ $\mathrm{n_{eq}cm^{-2}}$ charge collection data at 150 V bias and at T = -10°C. For an unirradiated sensor the charge carriers are produced almost uniformly along the sensor thickness. Electrons drift towards the n^+ implant, so that electron current decreases as z decreases. Holes drift towards the p^+ implant, so that hole current increases as z increases. For irradiated sensors, charge carrier trapping results in a net positive space charge density close to the p^+ backplane and a net negative space charge density close to the n^+ implant. It produces pn junctions at both sides of the sensor. The resulting electric field is minimal in the middle of the sensor and maximum at implants.

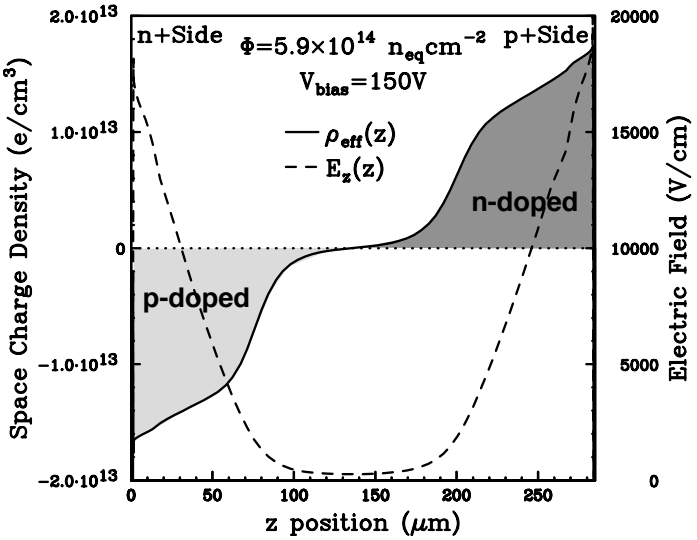

Figure 4.6 Space charge density (solid line) and electric field (dashed line) at T = -10°C as functions of depth in a double trap model tuned to reproduce the $\Phi = 5.9{\times}10^{14}$ $\mathrm{n_{eq}cm^{-2}}$ data at 150 V bias [43].

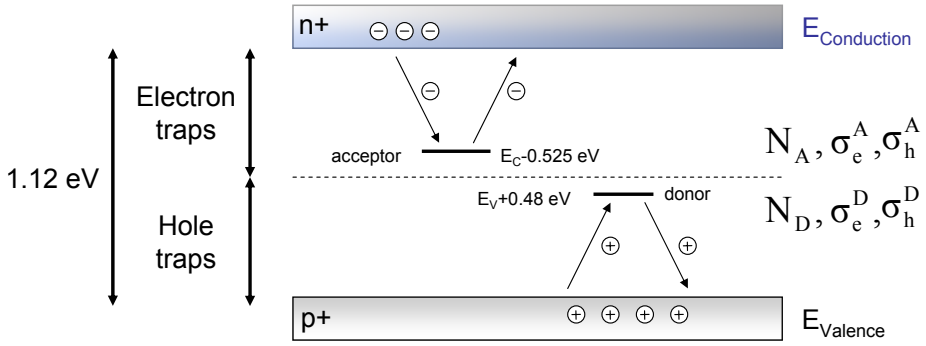

Figure 4.7 Schematic description of the EVL double trap model.

There are several issues relevant to the effective double trap model which can be listed as follows:

- the trapping cross sections $\sigma_{e/h}$ are not well known,
- the occupancies $f_{D/A}$ of the trapping states are independent of the absolute values of the cross sections but depend on their ratio $\sigma_{e/h}$,
- the generation and recombination current U is linear.

In the effective double trap model, the following is assumed: (1) relaxing the cross sections such as setting $\sigma_e^D = \sigma_e^A = \sigma_e$ and $\sigma_h^D = \sigma_h^A = \sigma_h$; (2) letting N_D, N_A, σ_e and σ_h vary, and (3) keep the activation energies as in the EVL model. In addition there are constraints which have to be taken into account. These are (1) the charge collection profiles at different bias voltages and irradiations, (2) the trapping rates, and (3) the generated leakage current. The effective electron (hole) trapping rates $\Gamma_{e(h)}$ can then be calculated as

$$\Gamma_e = \upsilon_e \left[\sigma_e^A N_A(1-f_A) + \sigma_e^D N_D f_D\right] \approx \upsilon_e \sigma_e^A N_A \tag{4.7}$$

$$\Gamma_h = \upsilon_h \left[\sigma_h^D N_D(1-f_D) + \sigma_h^A N_A f_A\right] \approx \upsilon_h \sigma_h^D N_D \tag{4.8}$$

where it has been assumed that the trap occupancies are small and the thermal velocity of electrons at $-10°$C is $\upsilon_e = 2.15\times10^7$ cm/s because N_D/N_A is assumed to be constant [44]. The effective double trap model is implemented into PIXELAV. Even if the simulation is below the measured profile, it reasonably describes the measurements as shown in Fig. 4.8. Simulation has also been performed for the irradiation fluences of $\Phi = 0.5\times10^{14}$ $\mathrm{n_{eq}cm^{-2}}$ and $\Phi = 2.2\times10^{14}$ $\mathrm{n_{eq}cm^{-2}}$.

4.1.4 The Lorentz deflection

In the presence of a magnetic field the electrons experience the Lorentz drift, which causes them to drift at an angle θ_L with respect to the electric field, given by the following expression

$$\tan(\theta_L) = r_H \mu(\vec{E}) \vec{B} \sin(\theta_{EB}) \tag{4.9}$$

where θ_L is the Lorentz angle, $\mu(\vec{E})$ (see Eq. 3.8) is the carrier mobility as a function of the internal electric field $\vec{E}$, r_H is the Hall factor (see Eq. 4.1), and θ_{EB} is the angle between

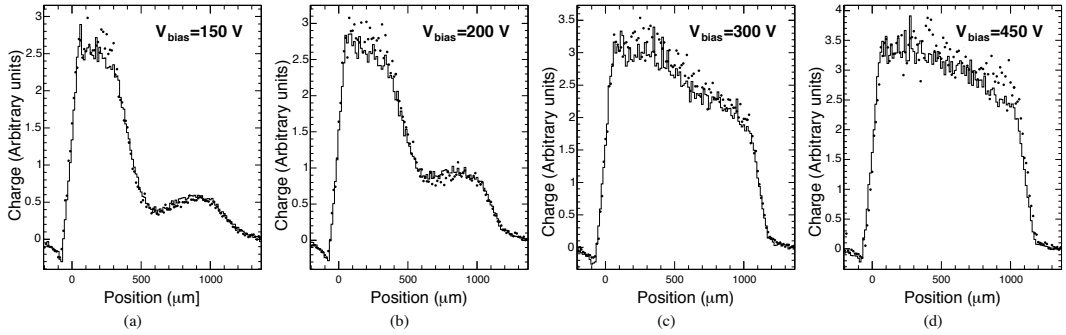

Figure 4.8 Measured charge collection profile for a sensor irradiated to a fluence of $\Phi = 5.9\times10^{14}$ $n_{eq}cm^{-2}$ (solid dots) and operated at (a) 150 V, (b) 200 V, (c) 300 V, and (4) 450 V biases are shown as solid dots. The effective double trap model simulation is shown as solid histograms in each plot [44].

the electric and magnetic fields. The total transverse displacement of the charge carriers is determined by integrating $\sin(\theta_L)$ over the drift path,

$$\Delta_y = \int_{path} \sin(\theta_L) dl \approx \int_{path} r_H \mu(\vec{E}) B \sin(\theta_{EB}) dz. \tag{4.10}$$

The mobility is roughly inversely proportional to the internal electric field (see Eq. 3.8). Therefore, the smaller the electric field, the larger the Lorentz angle and the displacement. Since trapping affects the charge collection, modifying the electric field, the Lorentz angle varies with irradiation. The effect of doubly peaked electric field on the Lorentz angle as a function of sensor depth is illustrated in Fig. 4.9 for a sensor irradiated to $\Phi = 5.9\times10^{14}$ $n_{eq}cm^{-2}$ at 200 V bias in 4 T. The hit reconstruction algorithms cannot therefore be based on a constant Lorentz angle.

4.2 Analysis of simulated data and results

4.2.1 Pixel clusters

The charge deposited by a charged particle passing through a pixel sensor is shown in Fig. 4.10. The tracking angles α and β are in the local x and y directions respectively. The electrons drift along the x direction (CMS rϕ-axis) which corresponds to the 100 μm pitch. The y (CMS z-axis) direction corresponds to the 150 μm pitch. A hit generates a cluster of up to four pixels in x due to the Lorentz deflection, while along y there is no Lorentz deflection. However, the cluster size goes up to ten pixels due to shallow tracks.

A typical cluster is shown in Fig. 4.11. The track angle $\beta = 20^\circ$ corresponds to $\eta = 1.83$. The pseudorapidity η is used for the y-coordinate calculations (see Fig. 4.1). In Fig. 4.11 the dashed red line shows the track projection on the cluster. The red cross represents the geometrical center of the particle track. Signals below the applied pixel threshold (2500 electrons) are shown in green. The large charge variations along the track are due to ionization fluctuations. For a cluster size larger than two pixels the hit position is determined by small signals near the cluster ends, while the charge distribution between the inner pixels is assumed to be flat. This

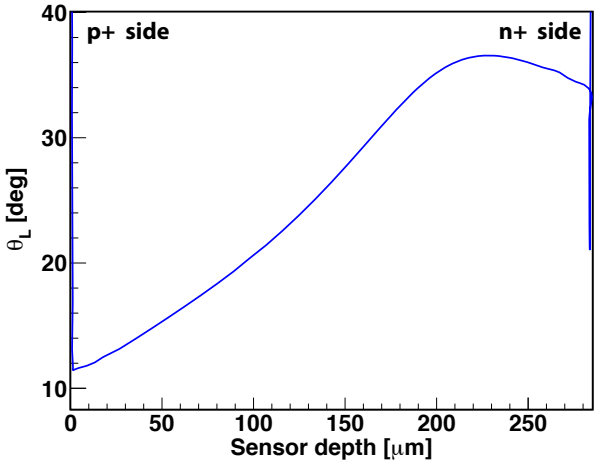

Figure 4.9 Lorentz angle as a function of sensor depth for a sensor irradiated to a fluence of $\Phi = 5.9{\times}10^{14}$ $n_{eq}cm^{-2}$ and operated at 300 V in 4 T magnetic field.

is to minimize the charge fluctuations. Energetic secondary electrons (δ-rays) can produce larger pixel signals causing unusual or long clusters. For example, along the x-axis δ-rays cause clusters larger than two pixels.

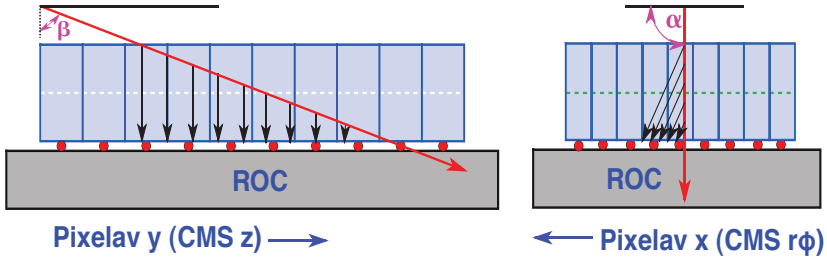

Figure 4.10 Charge deposition and drift in a pixel barrel module, left in the plane parallel to the beam, right in the plane transverse to the beam.

Pixel clusters are formed by combining adjacent pixels with charge above the pixel threshold. Both side and corner adjacent pixels are included in the cluster. The cluster charge is then obtained by projecting along x- and y- by summing the charge collected in the pixels with the same x- and y-coordinates.

4.2.2 Pixel hit reconstruction

The position resolution of the pixel sensors is mainly determined by the readout pitch and by charge sharing between neighboring pixels. Charge sharing is due to geometrical sharing (left sketch in Fig. 4.10) and Lorentz deflection (right sketch in Fig. 4.10). Charge carrier trapping causes nonuniform charge collection along the sensor bulk, as a consequence charge sharing between neighboring pixels becomes strongly nonlinear at the particle impact position.

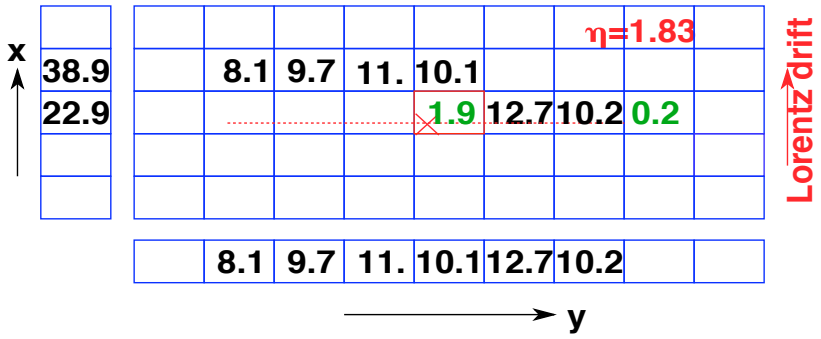

Figure 4.11 Charge deposition by a particle track ($\eta = 1.83$ or $\beta = 20°$). The signals in each pixel are in kiloelectrons. Signals below threshold are in green. The red cross is the geometrical center of the track and dashed red line represents the track projection.

For irradiated sensors the benefit of the Lorentz deflection is decreased due to the higher bias voltages needed to reach the maximum depletion.

The reconstruction of hits from clusters is done separately for the two coordinates. Along the x-projections there are mainly short clusters made of one as two pixels. δ-rays can cause clusters larger than 2 pixels, and as they spoil the determination of the particle hit position, they are excluded from the position resolution analysis along the x-axis (see Section 4.2.3.1).

Along the y-projections there are long clusters (> 2 pixels in a cluster). This is due to shallow impact angles β or pseudorapidity $\eta > 0$.

4.2.2.1 Transverse axis

The hit reconstruction along the x-axis is shown in Fig. 4.12 for a track in the transverse plane. It shows the definition of the track impact angle α. The angle α is defined so that it is positive (negative) towards the right (left) direction in Fig. 4.12. The total Lorentz deflection length L is given by

$$L = T \cdot \tan(\theta_L) \tag{4.11}$$

where T is the sensor thickness, and θ_L is the Lorentz angle. The total cluster width W_x is therefore given by

$$W_x = L - T \cdot \tan(\alpha) \tag{4.12}$$

W_x is largest when the α is on the left, as shown in Fig. 4.12.

The particle hit position for a single pixel cluster is given by the pixel center. For longer clusters the hit position x_{hit} is determined by the center of gravity,

$$x_{hit} = \frac{\sum_i q_i \cdot x_i}{\sum_i q_i} \tag{4.13}$$

where q_i is the charge deposited in the pixel x_i along the particle track.

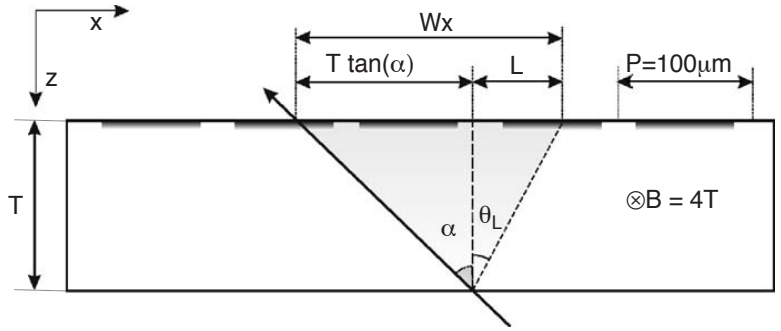

Figure 4.12 Impact position determination in the x-axis. In this figure the impact angle α is negative.

4.2.2.2 Longitudinal axis

The hit reconstruction along the y-axis is illustrated in Fig. 4.13. As mentioned previously, there is no magnetic deflection along this axis. The cluster width is therefore only determined by the electric field drift, charge diffusion, and the impact angle β. The cluster width W_y is given by

$$W_y = T \cdot \tan(\beta). \tag{4.14}$$

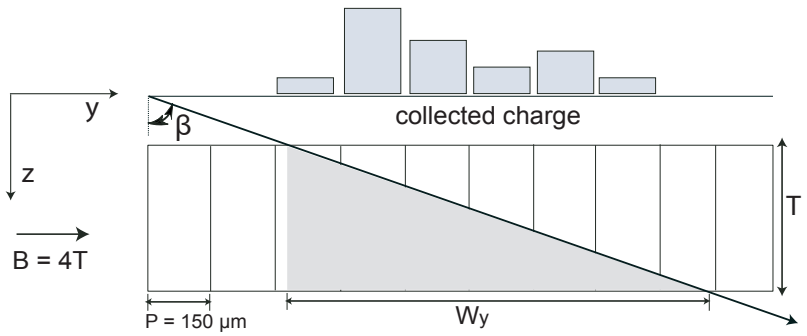

Figure 4.13 Impact position determination in the y-axis.

The hit position y_{hit} is calculated by [45]

$$y_{hit} = y_{center} + \frac{q^y_{last} - q^y_{first}}{2(q^y_{first} + q^y_{last})} ||W_y| - W^y_{inner}| \tag{4.15}$$

where y_{hit} is the particle hit position, y_{center} is the cluster geometrical center, W^y_{inner} is the length of the inner pixels and q^y_{first} (q^y_{last}) is the charge in the first (last) pixel. W^y_{inner} is defined as

$$W^y_{inner} = (y_{size} - 2) \times P, \tag{4.16}$$

where y_{size} is the cluster size, and P is the pixel pitch. This algorithm takes into account the fact that tracks do not in general enter or leave the sensor through sensor centers. The constraints of the algorithm are:

- cluster size (y_{size}) has to be larger than one pixel;
- $|W_y - W_{inner}|$ is set to P if W_y is larger than y_{size};
- for clusters larger than 4 pixels $|W_y - W_{inner}|$ is set equal to P in order not to spoil the position resolution in case of large charge fluctuation.

4.2.3 Results

Once the cluster hit coordinates are determined, the next step is the calculation of residuals, i.e. the difference between true hit positions x_{true} (y_{true}) generated by the simulation and reconstructed hit positions x_{rec} (y_{true}):

$$\begin{aligned} x_{residual} &= x_{rec} - x_{true}, \\ y_{residual} &= y_{rec} - y_{true}. \end{aligned}$$

4.2.3.1 Transverse position resolution

The distribution of cluster multiplicity along the x-axis as a function of impact angle α is shown in Fig. 4.14 for unirradiated and irradiated sensors. At negative α angles the Lorentz deflection and the geometrical charge width sum up resulting in longer total cluster width W_x, whereas shorter W_x values occur at positive α angles. In the heavily irradiated sensor the fraction for cluster of two pixels moves toward lower α values because of the smaller Lorentz angle at higher bias. For perpendicular tracks ($\alpha = 0°$) the cluster width is equal to the Lorentz deflection.

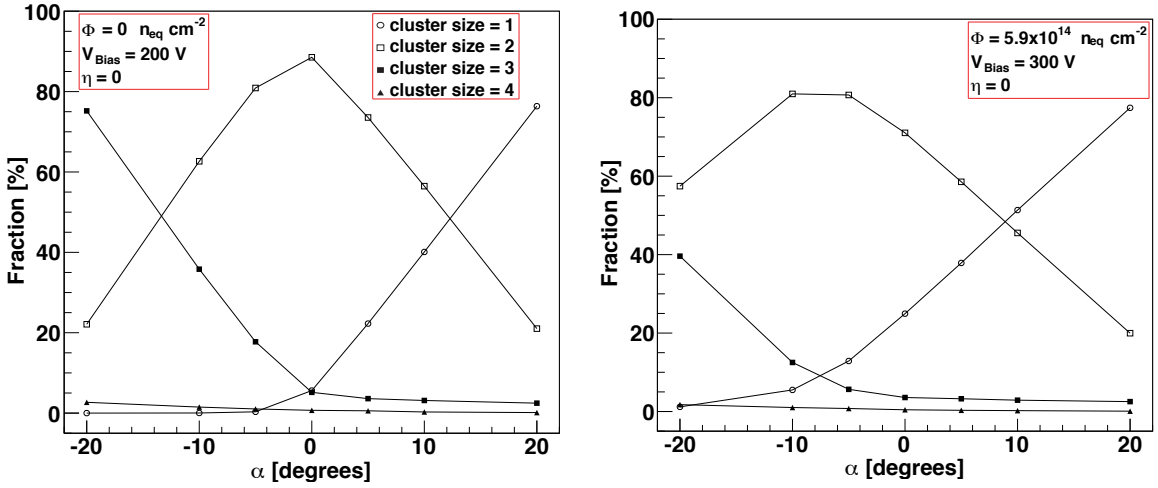

Figure 4.14 Cluster multiplicity distribution as a function of impact angle α (transverse x direction), for an unirradiated sensor (left), for a sensor irradiated to a fluence of $\Phi = 5.9{\times}10^{14}$ $\mathrm{n_{eq}cm^{-2}}$ [1] (right).

The combination of carrier trapping and higher bias voltages produces smaller cluster sizes after heavy irradiation. The average cluster size for an unirradiated sensor operated at 200 V and perpendicular tracks is 2.0. After a fluence of $\Phi = 5.9{\times}10^{14}$ $n_{eq}cm^{-2}$ and 300 V this value is 1.8.

As previously mentioned, clusters larger than two pixels are contaminated with δ-rays which produce more charge than expected. The cluster charge distribution as a function of impact angle α is illustrated in Fig. 4.15 for the transverse x-axis. The points are the mean of the average cluster charges. For clusters of three pixels the lowest charge is higher than 50'000 electrons which is equivalent to two times a MIP ($\approx$ 24'500 electrons). During the analysis an upper cluster charge of 1.5 MIP is applied to avoid δ-rays. Therefore, clusters larger than two pixels are excluded.

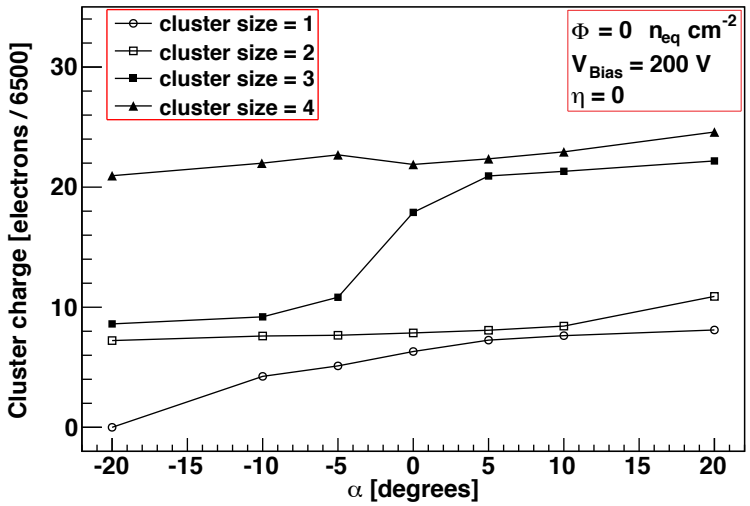

Figure 4.15 Cluster charge distribution as a function of impact angle α for an unirradiated sensor operated at 200 V in 4 T magnetic field (transverse x direction). The pseudorapidity η is zero.

As an example, the residual distribution along the transverse x-axis for clusters of two pixels is shown in Fig. 4.16 for an unirradiated sensor operated at 200 V in 4 T magnetic field. The distribution is not corrected for the Lorentz deflection. The residuls distribution is fitted with a Gaussian. The position resolution in microns is obtained by multiplying the Gaussian σ with the pixel pitch P (100 μm). The resolution is then $\sigma = 14.5$ μm.

The position resolution along the transverse x-axis as a function of impact angle α for an unirradiated and an irradiated sensor, for clusters of two pixels is shown in Fig. 4.17. The sigma values are not eta corrected. The resolution improves towards the positive α values. On the positive side α is closer to the Lorentz angle θ_L resulting in narrower charge sharing regions between adjacent pixels. Therefore, two-pixel cluster residual distribution becomes narrower. Note the position resolution degradation in the irradiated sensor due to charge trapping, particularly towards the negative α values where the charge sharing increases.

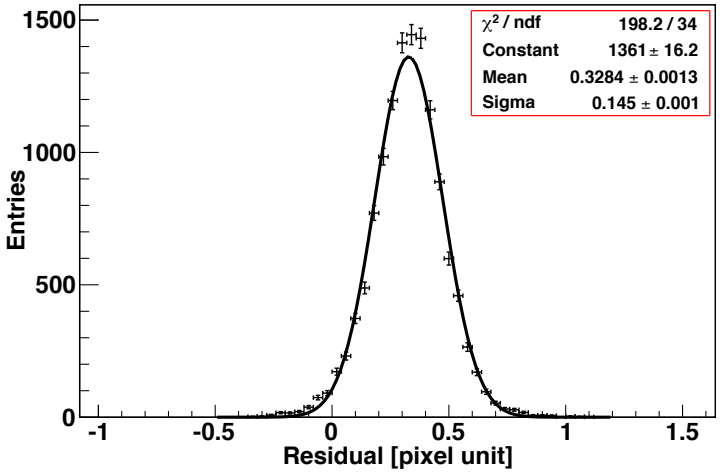

Figure 4.16 Residual distribution of an unirradiated sensor for tracks with the impact angle α = - 10° (transverse x direction). The distribution is not corrected for the Lorentz deflection. The simulated data points are represented by the markers and the line is a Gaussian fit to the distribution (simulation).

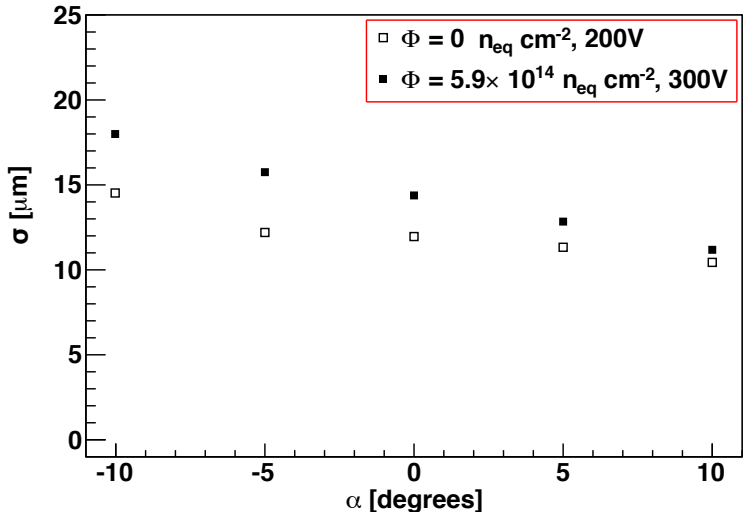

Figure 4.17 Position resolution as a function of impact angle α for an unirradiated and an irradiated sensor, for clusters of two pixels along the transverse x-axis (simulation).

4.2.3.2 Longitudinal position resolution

For very large pseudorapidity $|\eta|$ values the cluster length can be very large. The cluster multiplicity for an unirradiated sensor operated at 200V in 4 T magnetic field is shown in Fig. 4.18 as a function of pseudorapidity η along the longitudinal y-axis. For example, at $\eta = 0$ clusters of single pixels are dominant and the fraction of two-pixel clusters is only 10%.

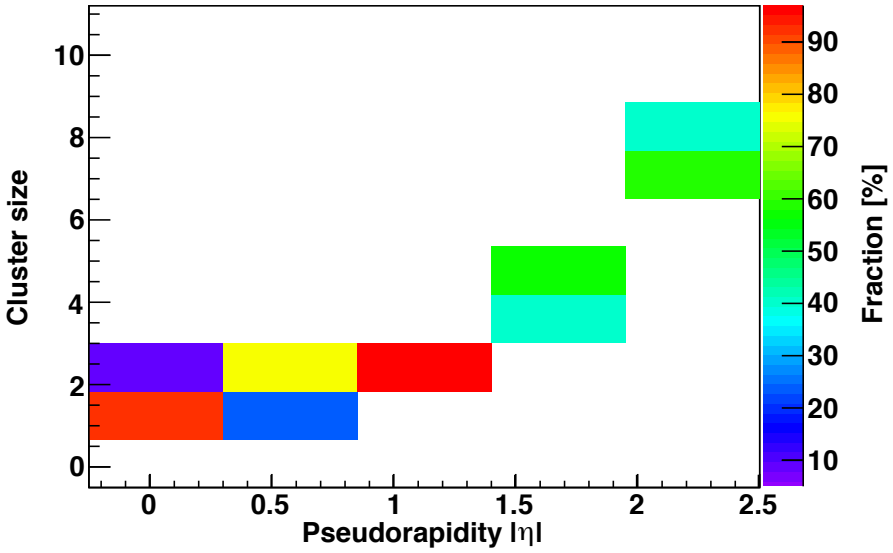

Figure 4.18 Cluster multiplicity as a function of η (longitudinal y direction).

The residual distribution for clusters of two pixels along the longitudinal y-axis for an unirradiated sensor operated at 200 V in 4 T magnetic field is shown in Fig. 4.19. A Gaussian function is fitted to the distribution. The position resolution is 21 μm.

The position resolution along the longitudinal y-axis as a function of $|\eta|$ for unirradiated and irradiated sensors and for all cluster sizes is shown in Fig. 4.20. For higher fluences the resolution degrades rapidly. At pseudorapidity $|\eta| = 0$ clusters include a single pixel and the resolution is binary [1] , corresponding to $\sigma = 43.3$ μm. The resolution improves substantially at pseudorapidity $|\eta| = 0.5$ due to enhanced charge sharing between sensors and degrades gradually at higher pseudorapidities due to very long clusters as illustrated in Fig. 4.18 (see also the same behavior in Fig. 4.26).

[1] If the sensor center is used as the measured coordinate and no charge sharing occurs between adjacent pixels, then the measurement accuracy (root mean square deviation from the true impact position) is given by the sensor pitch P

$$\sigma^2_{\text{position}} = \frac{1}{P}\int_{-P/2}^{P/2} x^2 dx = \frac{P^2}{12}$$
$$\sigma_{\text{position}} = \frac{P}{\sqrt{12}}.$$

The resolution can be improved with smaller pitch P and analog readout with lower thresholds.

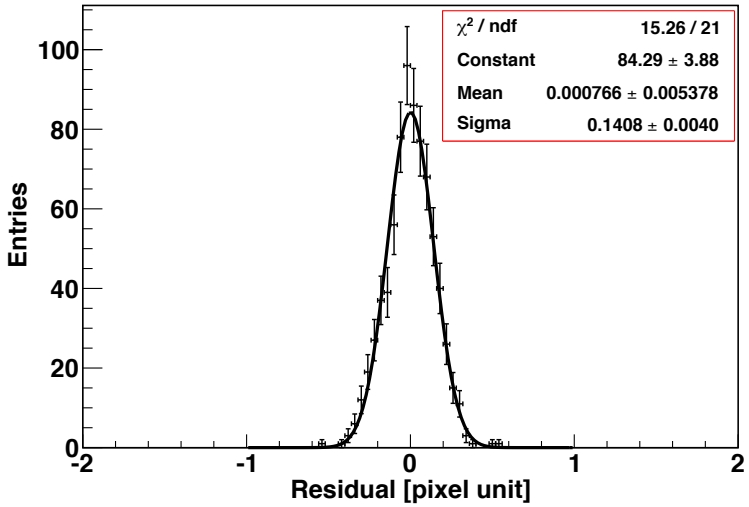

Figure 4.19 Residual distribution of an unirradiated sensor for tracks with the impact angle $\beta = 15°$ or $\eta = 2$ (longitudinal y direction). The simulated data points are represented by the markers and the line is a Gaussian fit to the distribution (simulation).

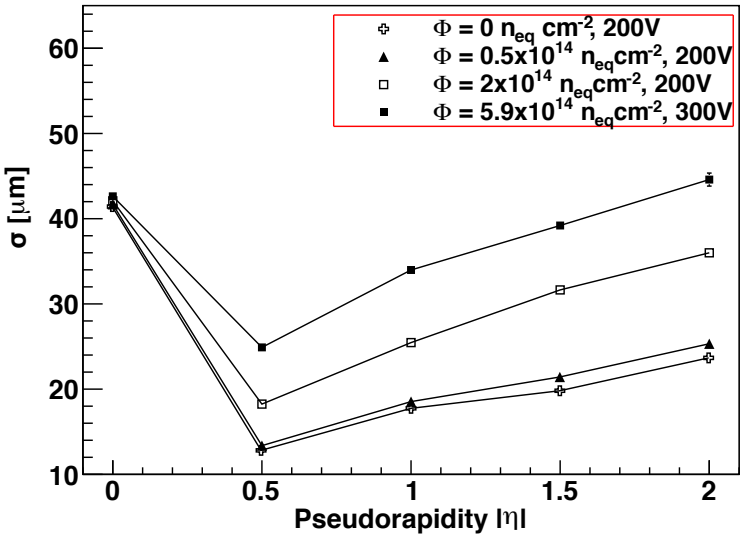

Figure 4.20 Position resolution of all cluster sizes as a function of pseudorapidity $|\eta|$ along the longitudinal axis for unirradiated and irradiated sensors. The simulated data points are extracted from single Gaussian fit to the residual distributions. The curves are to guide the eye.

4.2.4 Eta Correction

Usually it is assumed that generated charge carriers along the particle track are uniformly distributed in unirradiated sensors. Therefore, the charge distribution is expected to be uniform. However, the charge collection becomes inhomogeneous due to radiation induced damages which act as charge traps. This trapping effect on the charge collection is illustrated in Fig. 4.21 for the longitudinal axis.

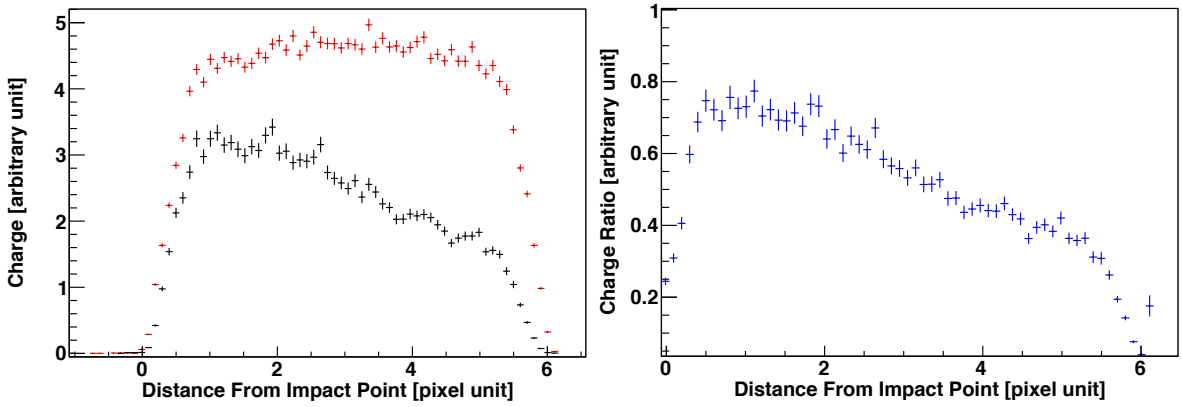

Figure 4.21 Left: simulated charge collection profile (longitudinal y direction) for an unirradiated sensor (red crosses) operated at 200 V and a sensor irradiated to a fluence of $\Phi = 5.9{\times}10^{14}$ $n_{eq}cm^{-2}$ (black crosses) operated at 300 V, as a function of distance from the impact point and for $\beta = 15°$ (or $\eta = 2$). Right: charge ratio of the irradiated sensor to the unirradiated one.

The nonuniform charge sharing produces systematical shifts on the reconstructed positions. This systematic effect for events where charge is shared between several adjacent pixels can be taken into account by the so-called eta-correction. A pixel hit contains the coordinate of the pixel in which charge is collected, and the position information within that pixel. For example, if the hit position is 14.3 the hit occurred in the pixel #14 and the floating number 0.3 is the location of the hit within the pixel 14. The non-integer part of the pixel hit is defined as ξ. The ξ distribution for all clusters is shown in Fig. 4.22 for perpendicular tracks ($\alpha = 0°$ and $\beta = 0°$). $\xi = 0$ is the pixel center and the peak at 0 is due to clusters with one pixel hit only. $\xi = \pm\ 0.5$ correspond to pixel borders where the flat distributions are due to clusters with more than one pixel hits. In other words, charge sharing mainly occurs across the pixel borders, whereas at the pixel center no charge sharing occurs.

The eta-correction corrects the reconstructed position by rescaling so as to get a uniform ξ distribution. The correction function $F(\xi)$ is given by

$$F(\xi) = \frac{\int_{-0.5}^{\xi}(dN/d\hat{\xi})d\hat{\xi}}{\int_{-0.5}^{0.5}(dN/d\hat{\xi})d\hat{\xi}} - \frac{1}{2} \tag{4.17}$$

where ξ is in pixel units. The function $F(\xi)$ provides a correction for each ξ value. The function $F(\xi)$ is shown in Fig. 4.23. Even though Fig. 4.22 and Fig. 4.23 are for the x-coordinate, the correction procedure is applied as well to the y-coordinate. The corrected positions x_{corr} and

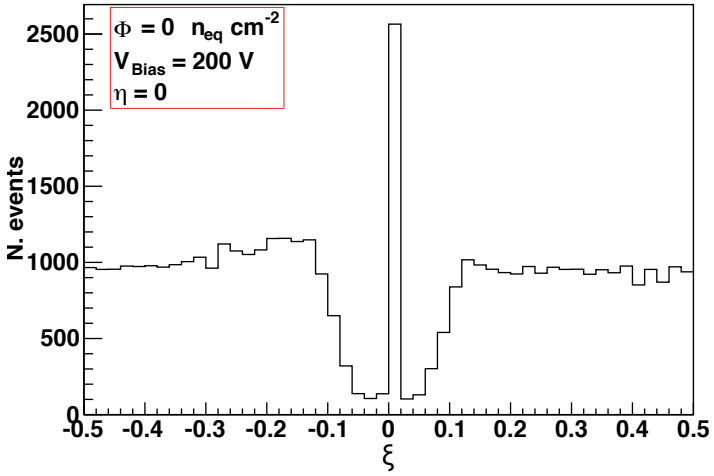

Figure 4.22 Distribution of ξ (transverse x direction and $\alpha = 0°$) for all cluster sizes in an unirradiated sensor operated at 200 V (simulation).

y_{corr} are given by

$$x_{corr} = x_{reco} + F(\xi) \tag{4.18}$$

$$y_{corr} = y_{reco} + F(\xi) \tag{4.19}$$

where x_{reco} (y_{corr}) is the reconstructed pixel index along the x-axis (y-axis). For example, for the transverse pixel hit position 15.43 x_{reco} is 15. As can be seen from the $F(\xi)$ function there is no correction for $\xi = 0$.

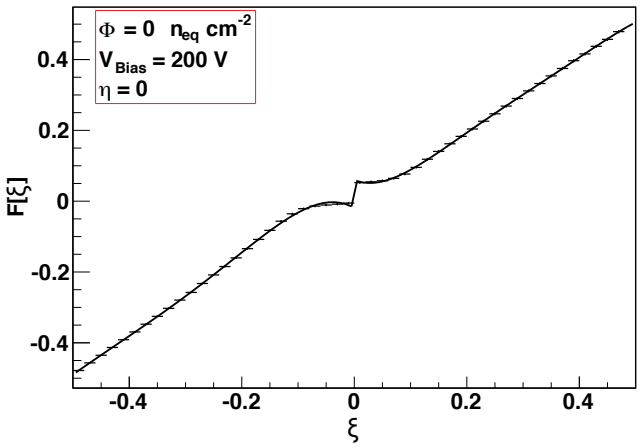

Figure 4.23 Correction function $F(\xi)$ (see Eq. 4.17) as a function of ξ extracted from the ξ distribution in Fig. 4.22 (transverse x direction and $\alpha = 0°$).

The effectiveness of the eta-correction method is illustrated in Fig. 4.24, which shows the residual distribution for a sensor irradiated to a fluence of $\Phi = 5.9{\times}10^{14}$ $\mathrm{n_{eq}cm^{-2}}$ and for

tracks with the impact angle $\alpha = 20°$ along the transverse x-axis. The distribution is not corrected for the Lorentz deflection. Note that the distribution shown in Fig. 4.24 is outside the CMS pixel barrel region corresponding to $|\alpha| \lesssim 10°$.

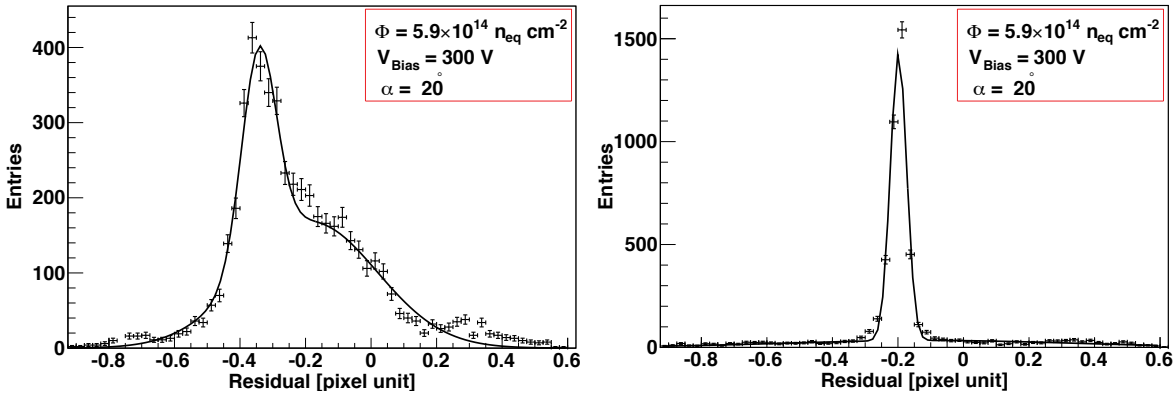

Figure 4.24 Residual distribution along the transverse x-axis for tracks with $\alpha = 20°$ for a sensor irradiated to a fluence of $\Phi = 5.9{\times}10^{14}$ $\mathrm{n_{eq}cm^{-2}}$. The distributions are processed without (left) and with eta-correction (right) and are not corrected for the Lorentz deflection. The simulated data points are represented by the markers and the solid line is a double Gaussian fit to the residual distribution [1].

The r.m.s residuals are shown in Fig. 4.25 as a function of impact angle α along the transverse x-axis for a sensor irradiated to a fluence of $\Phi = 5.9{\times}10^{14}$ $\mathrm{n_{eq}cm^{-2}}$. The position resolution for tracks perpendicular to the sensor ($\alpha = 0°$) is summarized in Table 4.1 for clusters of two pixels. In the table, the third and fourth columns represent the position resolution without and with eta-correction, respectively. The last column shows the resolution for all events, where the position of the two-pixel clusters are eta-corrected.

Depending on the track impact angle α, eta correction improves the position resolution. For instance, the resolution for $\alpha = 20°$ improves by 30%. In this case, the cluster width W_x is smaller because α is closer to the Lorentz angle ($\theta_L \approx 23°$). Therefore, the charge collection regions becomes very narrow reducing charge sharing. The eta-correction becomes larger when the track angle α is positive.

Table 4.1 Position resolution along the transverse x-axis for $\alpha = 0°$ at different fluences and bias voltages before and after eta correction for cluster of two pixels. The last column shows the resolution for all cluster sizes, where the position of the two-pixel clusters are eta-corrected [1].

Φ ($\mathrm{n_{eq}cm^{-2}}$)	$\mathrm{V_{bias}}$ (V)	Resolution without correction (μm)	Resolution with correction (μm)	Total resolution (μm)
0	200	9.3 ± 0.1	9.1 ± 0.1	9.0 ± 0.1
$2{\times}10^{14}$	200	13.4 ± 0.2	11.9 ± 0.2	12.1 ± 0.2
$5.9{\times}10^{14}$	300	13.3 ± 0.2	12.3 ± 0.1	12.9 ± 0.2

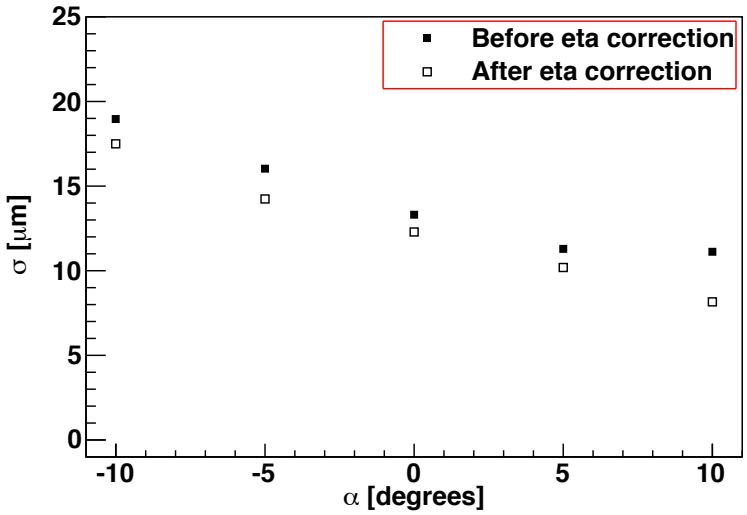

Figure 4.25 Position resolution (transverse x direction) as a function of impact angle α for clusters of two pixels, for a sensor irradiated to a fluence of $\Phi = 5.9{\times}10^{14}$ $n_{eq}cm^{-2}$ and operated at 300 V. The sigma values are shown before (solid squares) and after (empty squares) the eta-correction (simulation).

Along the longitudinal y-axis the position resolution as a function of pseudorapidity η for a sensor irradiated to a fluence of $\Phi = 5.9{\times}10^{14}$ $n_{eq}cm^{-2}$ is shown in Fig. 4.26. For larger η values the correction becomes larger. In the y-axis, the eta-correction improves the position resolution. For instance, the resolution for the highest pseudorapidity improves by 25%. The position resolution for tracks perpendicular to the sensor (pseudorapidity $\eta = 0$) is summarized in Table 4.2 for all cluster sizes.

Table 4.2 Position resolution along the longitudinal y-axis for pseudorapidity $\eta = 0$ at different fluences and bias voltages before and after eta-correction for all cluster sizes.

Φ ($n_{eq}cm^{-2}$)	V_{bias} (V)	Total resolution without correction (μm)	Total resolution with correction (μm)
0	200	41.3 ± 0.1	35.4 ± 0.1
$2{\times}10^{14}$	200	42 ± 0.1	35.8 ± 0.1
$5.9{\times}10^{14}$	300	42.6 ± 0.1	35.1 ± 0.1

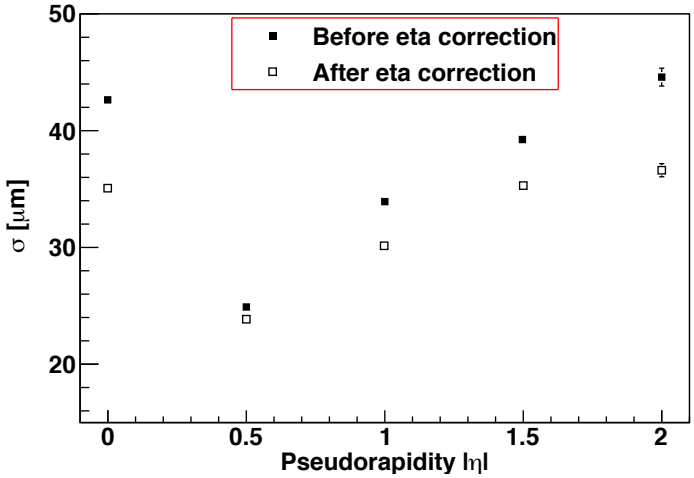

Figure 4.26 Position resolution along the longitudinal y-axis as a function of pseudorapidity η for a sensor irradiated to a fluence of $\Phi = 5.9\times10^{14}$ $n_{eq}cm^{-2}$ and operated at 300 V and for all events. The sigma values are shown before (solid squares) and after (empty squares) the eta-correction (simulation).

Table 4.3 Position resolution along CMS $r\phi$ as a function of impact angle α and along the CMS z as a function of pseudorapidity η for all events at different fluences in 4 T magnetic field. All events are eta corrected.

		Position resolution (μm)				
Φ ($n_{eq}cm^{-2}$)	V_{bias} (V)					
		α = -10°	α = -5°	α = 0°	α = 5°	α = 10°
0	200	14.26 ± 0.1	11.72 ± 0.1	9.1 ± 0.1	7.38 ± 0.1	5.59 ± 0.1
2×10^{14}	200	17.4 ± 0.2	14.5 ± 0.2	11.9 ± 0.2	10.6 ± 0.2	8.7 ± 0.2
5.9×10^{14}	300	17.5 ± 0.1	14.3 ± 0.1	12.3 ± 0.1	10.2 ± 0.1	8.2 ± 0.1
		$\eta = 0$	$\eta = 0.5$	$\eta = 1$	$\eta = 1.5$	$\eta = 2$
0	200	35.4 ± 0.1	14.0 ± 0.1	20.0 ± 0.1	21.8 ± 0.1	25.6 ± 0.1
0.5×10^{14}	200	35.3 ± 0.1	15.1 ± 0.1	21.0 ± 0.1	23.4 ± 0.1	27.7 ± 0.1
2×10^{14}	200	35.8 ± 0.1	20.1 ± 0.1	28.2 ± 0.1	33.8 ± 0.1	38.0 ± 0.1
5.9×10^{14}	300	35.1 ± 0.1	26.0 ± 0.1	37.1 ± 0.1	41.8 ± 0.1	47.8 ± 0.1

4.3 Summary

In this chapter a detailed simulation of the silicon pixel sensors for the CMS pixel detector is used to estimate the effects of radiation damage on the position resolution. The simulation, incorporating a double trap model of radiation damage and trapping of charge carriers, was shown to give a good description of the charge collection measurements in the irradiation fluence range from 0.5×10^{14} to 5.9×10^{14} $n_{eq}cm^{-2}$ [44].

The analysis of the simulated data includes clusterization, cluster position reconstruction, residual determination, and eta-correction.

The readout threshold is set to 2500 electrons. The systematic effects due to charge trapping can be corrected by the eta-correction method which improves the position resolution.

After an irradiation fluence of $\Phi = 5.9\times10^{14}$ $n_{eq}cm^{-2}$ and operating at 300 V in 4 T magnetic field one finds for perpendicular tracks:

- a position resolution of 13.3 μm improving to 12.3 μm after eta-correction along the transverse axis (CMS $r\phi$),
- a position resolution of 42.6 μm decreasing to 35.1 μm after eta-correction along the longitudinal axis (CMS z).

In Table 4.3, the position resolution along the CMS $r\phi$ (transverse) as a function of impact angle α and along the CMS z (longitudinal) as a function of pseudorapidity η are given for different irradiation fluences. All events are eta corrected.

5 Experimental setup for beam tests

5.1 Experimental setup

The experimental testbeam setup consisted of five components: a pixel telescope, a pixel device under test (DUT), a trigger PIN diode, a cooling system, and a data acquisition system. The pixel telescope had 4 identical unirradiated ROCs [1]. Two ROCs were placed in front of and two behind the DUT. Each ROC had 80 rows and 52 columns of pixels with dimensions 100×150 μm^2. The 100 μ pitch was along the the x-axis (transverse CMS $r\phi$) and 150 μ pitch along the y-axis (longitudinal CMS z). The sensor thickness was 285 μm^2. A picture of the setup is shown in Fig. 5.1.

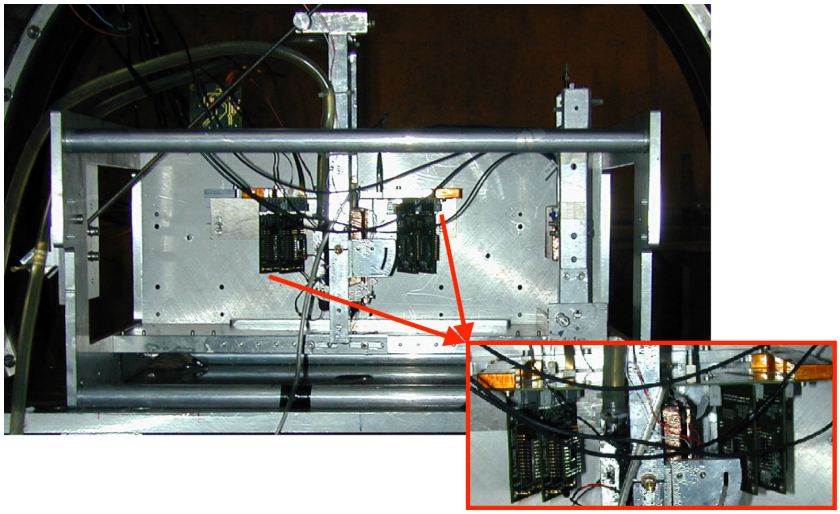

Figure 5.1 Testbeam experimental setup.

The whole setup was placed in an open pair of Helmholtz coils, capable of providing a 3 T maximum magnetic field. The magnetic field was perpendicular to the beam, i.e. perpendicular to the x-axis and parallel to the y-axis. A sketch of the experimental setup is illustrated in Fig. 5.2. All measurements were performed on the H2 beam line of the CERN SPS with 150 GeV pions. The beam had a 25 ns bunch structure. However, a timing signal for the beam was not used for these measurements. The data was taken with and without magnetic field.

The pixel telescope was used to extrapolate the position resolution on the DUT. The telescope ROCs were operated at 150 V and at room temperature. A 20° tilting was applied to the longitudinal y-axis of the telescope ROCs so as to increase charge sharing improving

[1] The term "ROC" will be used for the pixel sensor and the readout chip.

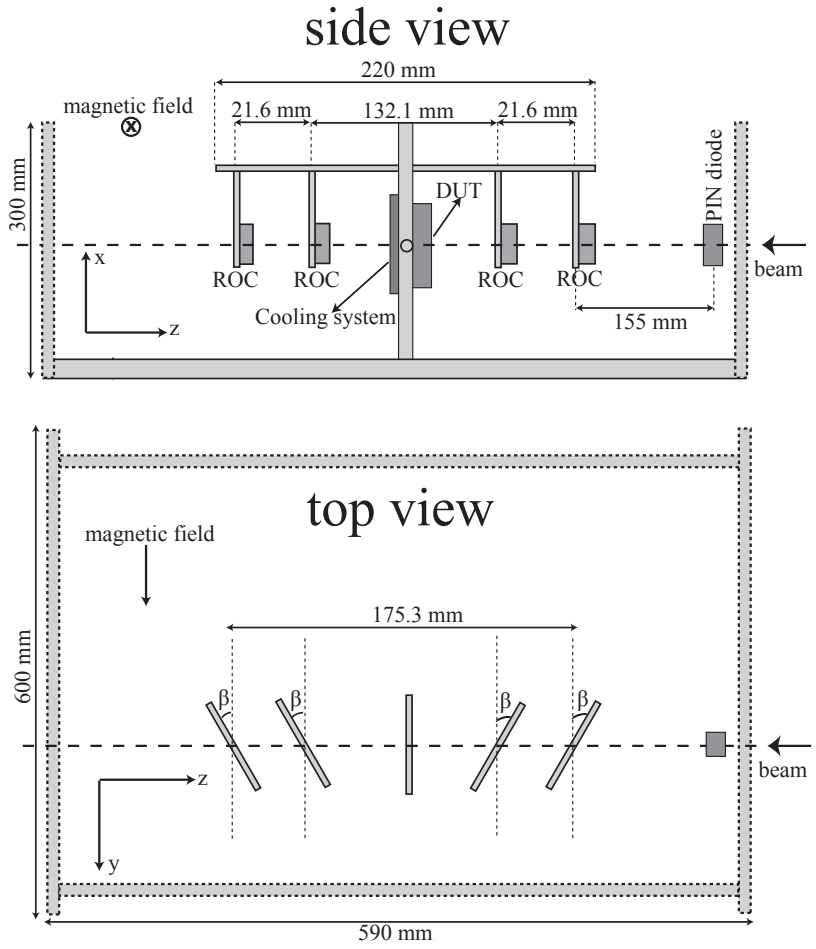

Figure 5.2 Side and top views of the experimental setup.

the position resolution. Therefore, a better track determination could be performed along the y-axis.

The readout and data acquisition was carried out by a motherboard. The motherboard was connected to the ROC readout system with a special readout adapter, which provided control signals, data readout, and sensor bias for the telescope ROCs. The DUT was kept in a cooling box to reduce the leakage current and to avoid reverse annealing. The cooling box was airtight. The cooling of the DUT was established by two water cooled Peltier elements. The hot sides of the Peltier elements were refrigerated with water circulation via a water chiller. The trigger signal was produced by a PIN diode that was placed in front of the telescope. The PIN diode position could be adjusted with a precision of 100 μm.

5.1.1 Sample preparation and sensor testing

The pixel sensors were bump bonded to ROCs of the type PSI46v2 at PSI. Then sensors were irradiated at the CERN IRRAD1 facility with a 24 GeV proton beam. The irradiation was performed at room temperature without a bias voltage applied. After irradiation the samples

were stored in a commercial freezer at $-20°$ and only warmed up for handling. To reach the minimum full depletion voltage they were annealed at 21°C for seven days. The irradiation fluence was converted to 1 MeV neutron equivalent by the scale factor 0.62 [46]. The delivered proton fluences were 2.2×10^{14} $n_{eq}cm^{-2}$, 6.2×10^{14} $n_{eq}cm^{-2}$, and 8.2×10^{14} $n_{eq}cm^{-2}$.

All samples were then wire-bonded to custom-made four layer printed circuit boards (PCB), shown in Fig. 5.3.

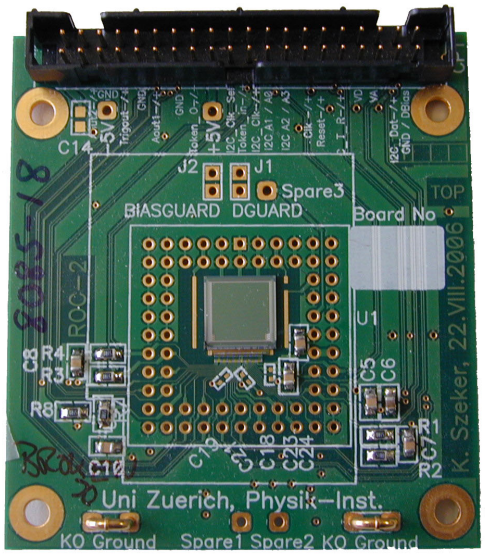

Figure 5.3 PCB with a single-chip sensor.

The selection of the samples for the test beam was based on the same test procedure as was used for the CMS pixel barrel modules [47]. The qualification procedure can be used for single ROCs as well. This test procedure consists of hardware functionality tests, performance tests, and calibrations tests. The tests were carried out together with the ETH collaboration [2]. The qualification test steps are described in the following sections.

5.1.1.1 Pixel address decoding test

The pixel address decoding test is used to separate individual pixel address levels. The pixel addresses define the physical position of pixels on a ROC and are encoded analogous. A single pixel address contains five clock cycles. Three clock cycles are needed for the row index, and two for the column index. Each clock cycle can have six different levels. The levels of all pixels in a ROC are measured and filled into a histogram as shown in Fig. 5.4. Correct decoding requires well separated signal levels. A simple algorithm searches for the peaks in this histogram. If six of them are found, then separation limits are put between neighboring peaks for decoding.

[2] Institut für Teilchenphysik, ETH-Zürich, 8093 Zürich, Switzerland

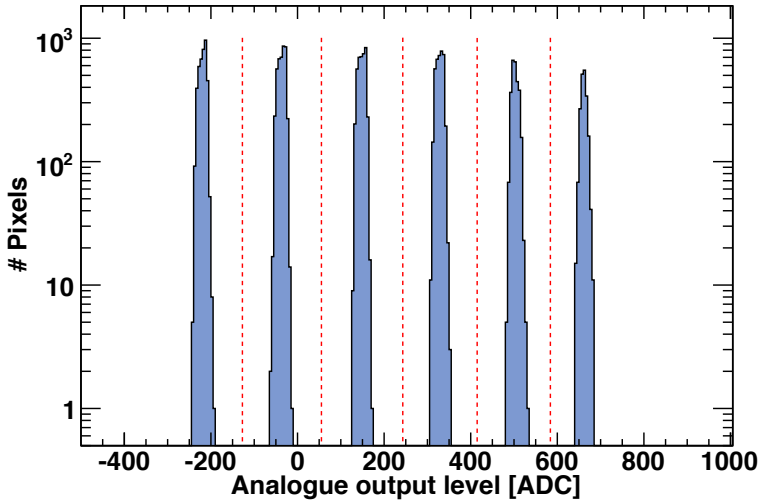

Figure 5.4 Address levels of all pixels in a ROC. The dashed red lines are the decoding limits between two adjacent peaks.

5.1.1.2 Trimming test

The trimming test is used to equalize all the pixel thresholds in a ROC which ensures a uniform response of the whole ROC. For all ROCs used in the testbeam, a trim value of 50 in units of the *Vcal* DAC (see Section 2.2.2) has been used. 1 Vcal corresponds to 65.5 electrons.

5.1.1.3 S-curve test

The s-curve test is used to determine the pixel noise. A typical s-curve plot for one pixel in a ROC is shown in Fig. 5.5. The s-curve is obtained by sending calibration signals and measuring the pixel response efficiency. Then an error function is fitted to the histogram. The pixel noise is determined from the slope of the curve at the turning point.

The noise distribution of all pixels in a ROC is shown in Fig. 5.6. The overall noise level is determined by fitting the noise distribution with a Gaussian function (not shown). The determined noise level is 164 e^- with an r.m.s spread of 17 e^-. In Table 5.1, the noise levels are given for the unirradiated and irradiated ROCs which were used in the testbeam. The first four unirradiated samples in the table are the telescope ROCs. These noise levels are used to calculate the signal-to-noise ratio, which is described in Section 6.2.2. Note that the noise of the sample with the highest irradiation fluence may be lower than the noise of the unirradiated one even if the charge collection of the former is worse.

5.1.1.4 Pixel alive and bump-bonding test

The pixel alive test is used to find defective pixels. It is done by sending 10 calibration signals to each pixel and reading them out. Only samples without any dead pixels were selected.

The purpose of the bump-bonding test is to check the bump-bonding quality. A charge is induced in the pixel sensor by the calibration signal and the charge is measured by the ROC. If

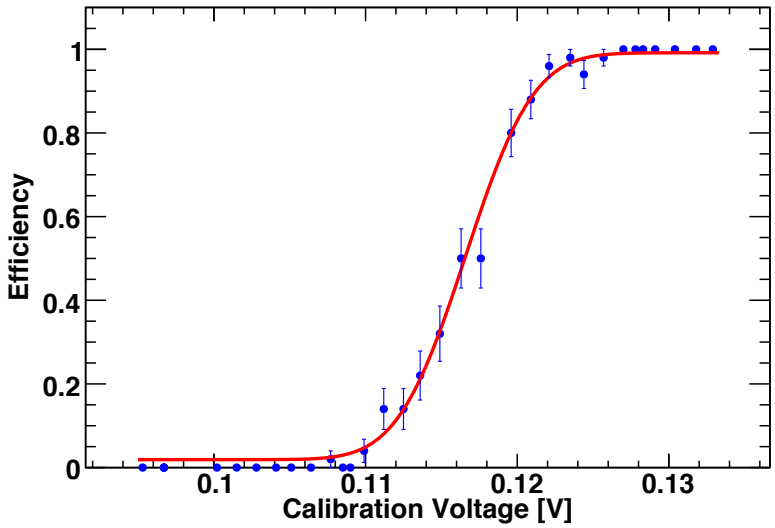

Figure 5.5 S-curve fit with an error function for measuring the noise level of a pixel.

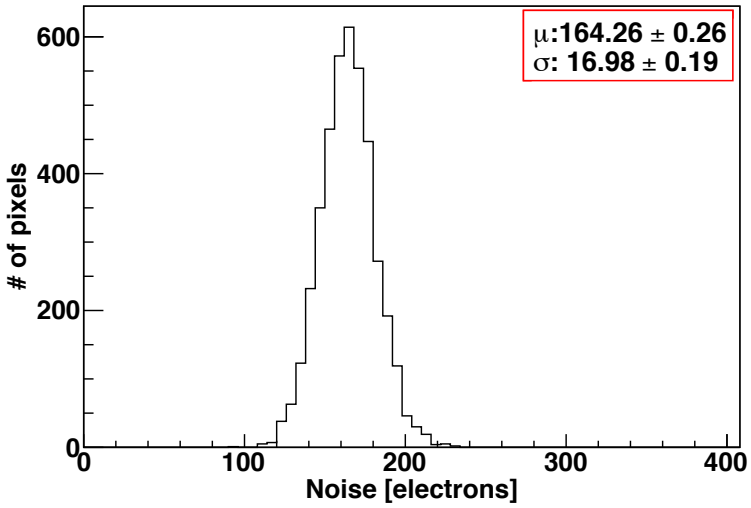

Figure 5.6 Noise distribution of an unirradiated ROC.

the bump-bond is functioning then the charge is detected, the bump-bond is missing otherwise. The samples with no defective bump bond were selected.

5.1.1.5 Pulse height calibration

Pulse height calibration is used to correlate the pulse height with the injected charges. The pulse height spectrum basically is the energy spectrum or a measure of the ionization charge. All signals are recorded in digital ADC counts. These ADC counts have to be converted back into ionization charge.

Table 5.1 Noise levels for the unirradiated and irradiated ROCs which are used in the test-beam. The first four unirradiated samples are the telescope ROCs ($T_{1,2,3,4}$) and the rest are the detector under test ROCs ($DUT_{1,2,3,4}$).

Detector	Φ ($n_{eq}cm^{-2}$)	Noise μ (electrons)	Noise spread σ (electrons)
T_1	0	173.73	19.30
T_2	0	169.69	18.47
T_3	0	176.19	17.88
T_4	0	173.98	18.10
DUT_1	0	164.26	16.98
DUT_2	2.2×10^{14}	114.32	18.72
DUT_3	6.2×10^{14}	124.27	22.62
DUT_4	8.2×10^{14}	124.73	22.10

The pulse height calibration is performed separately for every pixel, since the ADC to ionization charge conversion varies from pixel to pixel in a ROC. Calibration is carried out by injecting calibration signals of several amplitudes and recording the pulse heights. Each measured pulse height is an average over 10 readouts for better precision. In Fig. 5.7 a typical pulse height calibration curve as a function of calibration signal $Vcal$ is shown. The pulse height rises linearly and saturates at high amplitudes. There is no pulse height measured below $Vcal$ 10 because the signal is below the threshold.

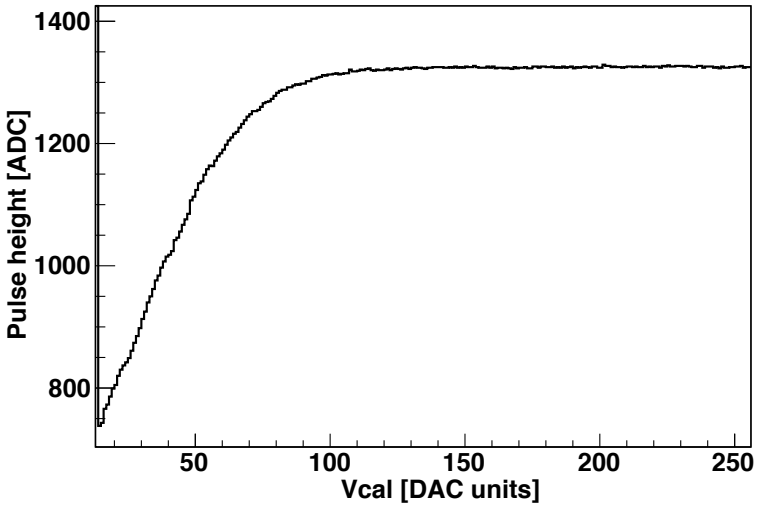

Figure 5.7 Pulse height as a function of calibration signal $Vcal$. There is no pulse measured below $Vcal$ 10, where the signal is below the threshold.

The pixel gain and pedestal values are determined from a linear fit to the region where there is a large linear dependency (see Fig. 5.7). The slope of the fit determines the pixel gain, and

the offset the pedestal. In Table 5.2, the gain and pedestal values for the tested samples are given. The first four unirradiated samples in the table are the telescope ROCs.

Table 5.2 Gain and pedestal values for the unirradiated and irradiated ROCs which are used in the testbeam. The first four unirradiated samples are the telescope ROCs ($T_{1,2,3,4}$) and the rest are the detector under test ROCs ($DUT_{1,2,3,4}$).

Detector	Φ ($n_{eq}cm^{-2}$)	Gain	Pedestal (electrons)
T_1	0	2.01	-257.2
T_2	0	1.70	-268.3
T_3	0	1.71	-250.3
T_4	0	1.83	-372.7
DUT_1	0	1.59	-103.5
DUT_2	2.2×10^{14}	1.87	-92.3
DUT_3	6.2×10^{14}	1.82	-103.7
DUT_4	8.2×10^{14}	1.74	-40.3

In order to determine the nonlinearity in the low pulse region the whole calibration curve is fit with the function

$$y = \tan[p_0 \cdot x - p_4] + p_1 \cdot x^3 + p_5 \cdot x^2 + p_2 \cdot x + p_3 \tag{5.1}$$

where p_0, p_1, p_2, p_3, p_4, and p_5 are the six free parameters.

5.1.1.6 Leakage current measurements

In the presence of the testbeam leakage currents were measured by a Keithley 2410 sourcemeter (see Section 5.1.2) for several irradiation fluences at several bias voltages. It is well known that irradiation negatively affects silicon detector performance. Effects are due to radiation induced damages or traps (see Section 3.5) in the silicon bulk. The leakage current is proportional to radiation fluence. Therefore, one can monitor fluences by measuring the leakage current. The measured leakage currents as a function of bias voltages for several irradiation fluences are shown in Fig. 5.8. For an unirradiated sensor the leakage current is in the order of a few nA. The leakage currents are measured at a temperature of $-10°C$. For damage rate calculations the leakage currrents at 200 V is chosen for unirradiated and irradiated sensors.

The leakage current of a module is estimated by multiplying the single ROC leakage currents measured at 200 V (see Fig. 5.8) by 16, since a pixel barrel detector module consists of 16 ROCs (see Section 2.2). The leakage current measurements for the testbeam ROCs and estimated leakage currents for a pixel barrel module as a function of irradiation fluence are shown in Fig. 5.9. The error on the bias voltage is assumed to be 5% while the error on the fluence measurement is 7%. The estimation on the error of the fluence measurement comes from CERN IRRAD1 facility where the sensors are irradiated. At a fluence of 8×10^14 $n_{eq}cm^{-2}$ the leakage current is four orders of magnitude larger than for an unirradiated sensor.

The leakage current damage rate α depends on the leakage current in the active sensor volume, annealing time t, and radiation fluences. The damage rate α can be determined by

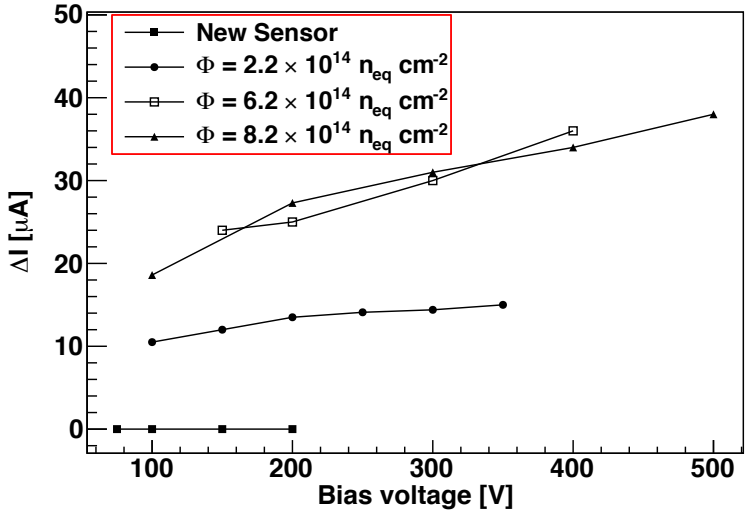

Figure 5.8 Leakage current for unirradiated and irradiated ROCs as a function of bias voltage.

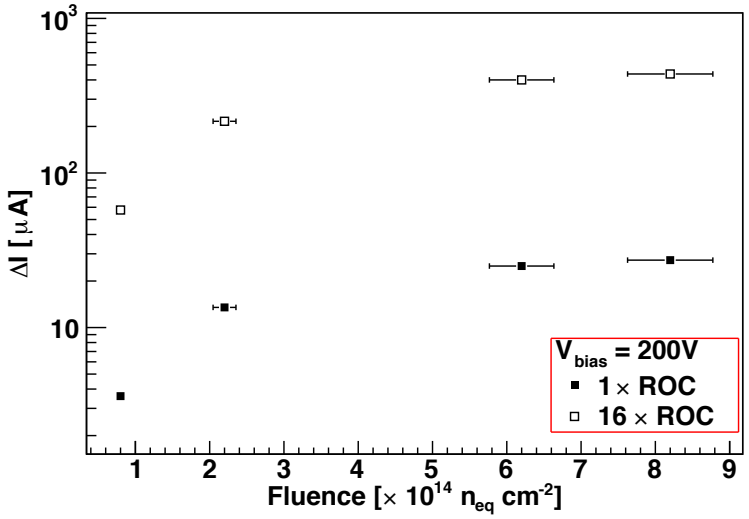

Figure 5.9 Leakage current as a function of radiation fluence. The leakage current of a module is estimated by multiplying the single ROC leakage current with a factor of 16.

(Eq. 3.13):

$$\alpha(\Phi, \mathrm{V}, \mathrm{t}) = \frac{\Delta \mathrm{I}(\Phi, \mathrm{t})}{\mathrm{V} \cdot \Phi} \tag{5.2}$$

where Φ is the radiation fluence, ΔI is the measured leakage current, and V is the sensor active volume. The volume includes 52 pixel columns, 80 pixel rows and with the sensor thickness of 285 μm leads to a total volume of 0.018 cm^3.

The annealing time for the testbeam sensor was 7 days at room temperature. This is equivalent to 80 minutes annealing at 60°C, which are the standard used parameters. Since the leakage current ΔI is measured at -10°C, they have to be normalized to room temperature 21°C so as to be able to compare damage rate results. The normalization can be done according to the following equation

$$\Delta I_{T_{room}} = \Delta I_{meas} \cdot \left(\frac{T_{room}}{T_{meas}}\right)^2 \cdot \exp\left[-\frac{E_a}{2k_B}\left(\frac{1}{T_{room}} - \frac{1}{T_{meas}}\right)\right] \tag{5.3}$$

where $\Delta I_{T_{room}}$ is the leakage current at T_{room} (21°C), E_a is the silicon activation energy (1.09 eV) and k_B is the Boltzmann constant [48].

Once $\Delta I_{T_{room}}$ is obtained, the expected α at room temperature is then calculated by Eq. 5.2. The calculated α values as a function of irradiation fluence are shown in Fig. 5.10. They are in the order of 10^{-17}Acm^{-1} and all agree within the uncertainties showing that α is independent of the fluence.

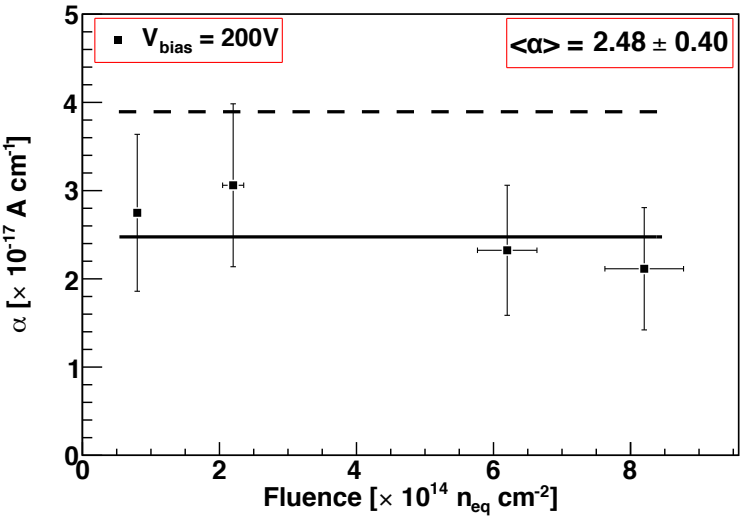

Figure 5.10 Damage rate as a function of radiation fluence. The solid line shows the average value, and the dashed line the measurement from ref. [31].

The expected α is determined by taking the average (see Fig. 5.10) as

$$\alpha = (2.48 \pm 0.40) \times 10^{-17}\mathrm{Acm}^{-1},$$

and it is about 40% smaller than the α value from [31]

$$\alpha = (3.99 \pm 0.03) \times 10^{-17}\mathrm{Acm}^{-1}.$$

Possible reasons for the observed difference in the α value are: the current scaling to 21°C, and the definition of the active volume in the small sensor. Since the region near the guard rings has a complicated electric field structure, it is not so clear where to define the boundary of the leaking region. In bigger sensors, this is less of an issue, because the total edge regions are a smaller fraction of the total volume. In addition, at the highest fluence there is a low electric field region in the middle of the sensor. One needs to bias to higher voltages to be fully efficient but the leakage current increases with bias.

5.1.2 Readout and data acquisition

The readout is performed by the PSI46v2 readout chip, which is bump-bonded to telescope and DUT sensors. When the trigger PIN diode is traversed by a particle, it produces a trigger signal which is sent to the test board. The analog pixel signals of all ROCs are sent through the TBM (see Section. 2.2) to the test board where they are digitized by a 12 bit analog-to-digital converter (ADC). A typical analog readout signal from all ROCs on a oscilloscope display is shown in Fig. 5.11. The digital signals are stored in a 64 MB SDRAM buffer. As soon as the buffer is full, the data is copied to a PC.

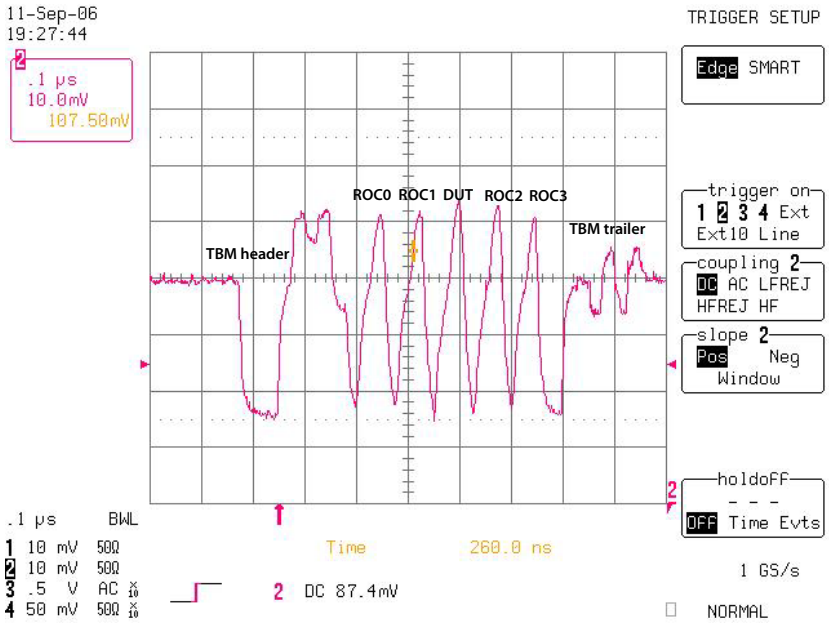

Figure 5.11 Analog readout signal with no particle hit. The analog signal consists of TBM header and trailer, and signals from 5 ROCs.

The data acquisition system consists of a motherboad for control and readout of the setup, a TBM adapter card, a TBM PCB, 2 Keithley 2410 Sourcemeters, and a Peltier controller. The Keithley sourcemeters are used to bias DUT and the telescope. In addition, these sourcemeters are used to measure DUT leakage currents. The adapter card connects the TBM PCB to the motherboad. The Peltier controller is used to bias the Peltiers. The controller is used as well as a temperature display. The temperature display is realized by a PT1000 temperature sensors.

The motherboard shown in Fig. 5.12 was designed at PSI for the CMS barrel pixel module testing and qualification. It requires 6 V power to operate. The motherboard has several components: a field programmable gate array (FPGA), 64 MB SDRAM, universal serial bus (USB) interface, a 12 bit ADC, a 4 Mbit flash memory, trigger interface, and a telescope bias (HV) interface. The USB interface connects the motherboard to a desktop PC, which is located in the control room. The desktop PC is operated with Scientific Linux 4.

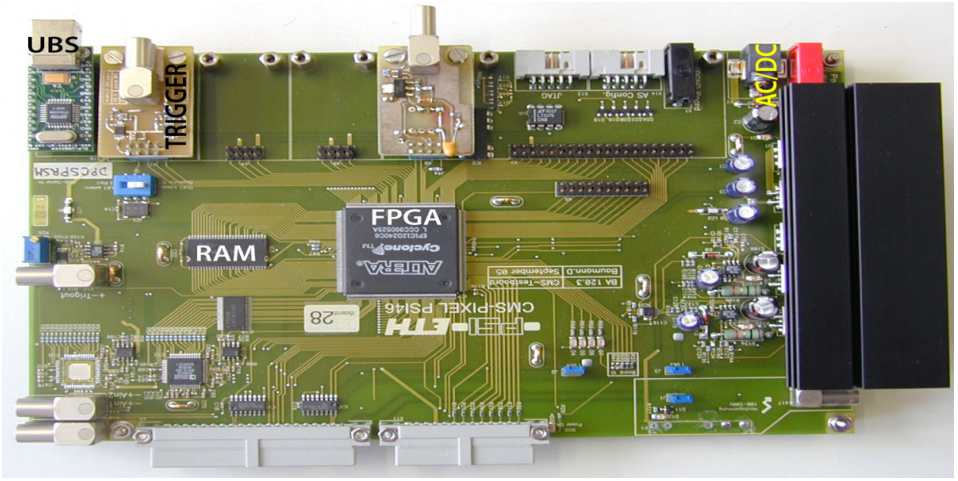

Figure 5.12 Testbeam motherboard for readout and data aquisition.

The motherboard provides supply voltages and electric signals to the TBM and the ROCs. The 12 bit ADC convert continuous analog signals into discrete signals. The ADC sampling interval is [-2048,2048]. 1 ADC count is equivalent to 0.128 mV.

All ROCs are connected to the TBM PCB. In addition this PCB has three interfaces: one for the control signals via a Kapton [3] cable, one for the telecope bias, and one for the DUT bias. The separate DUT bias connection is for operating test sensors at different bias voltages. The telescope bias is fixed to 150 V. The data acquisition system is shown in Fig. 5.13. A PIN diode is used to generate trigger signals. It is coupled to a low noise fast amplifier. The trigger system response is faster than 30 ns as required from the readout system which is optimized to 40 MHz. The preamplifier has a low noise operational amplifier. A fast comparator and a monostable circuit provide TTL and NIM pulses to the readout system. The PIN diode is described in more details in ref. [49].

5.1.3 Cooling

The heat generated by the ROCs has to be dissipated. This was done by means of two Peltier cooling elements. The Peltier elements have dimensions of 40×40×3.2 mm^3 and require 172 W of power. The Peltier elements are glued on the back side of the cooling box and they are placed in such a way that they surround DUT. A heat conduction paste is used to improve the thermal contact between the Peltier metal contacts and the DUT PCB.

The hot sides of the Peltier elements are cooled by circulating water. This is provided by the water chiller through the Peltier housing. The water chiller is operated around 5°C. This

[3] Kapton is a polyamide film of DuPont™.

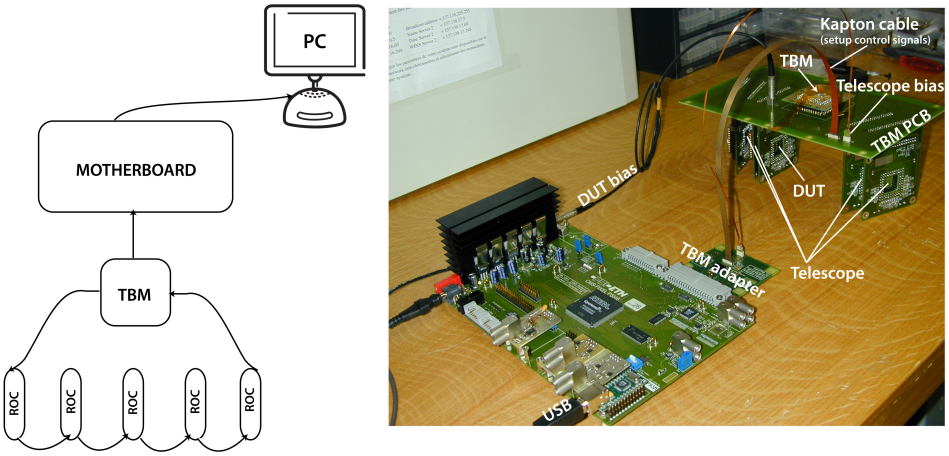

Figure 5.13 Testbeam data aquisition system (right) and data flow schematics (left).

is sufficient to cool the Peltier elements.

A PT1000 temperature sensor is attached on the DUT PCB to monitor the the DUT temperature regularly. This is used as a feedback to the Peltier cooling system. The DUT temperature is kept between $-5°C$ and $-10°C$ with a precision of $1°C$. Note that the CMS pixel detector operational temperature will be $-5°C$.

6 Data analysis and beam test results

The beam test results are discussed in this chapter. The data analysis steps are first described: pixel clustering, cluster position reconstruction, track reconstruction and spatial alignment, and event selection. Then charge collection is measured as a function of bias voltage and irradiation fluence, the signal-to-noise ratio as a function of irradiation fluence. Finally I present the position resolution results for different irradiation fluences, bias voltages, and readout thresholds.

6.1 Event reconstruction and analysis

A schematic diagram of the testbeam hardware is shown in Fig. 6.1. Several steps are performed during the data analysis. The raw binary data is first converted into ROOT [1] ntuples. Pixel clusters are formed by joining adjacent pixels and the cluster positions are determined. The procedure is completed by track reconstruction after spatial alignment of the sensors. The event reconstruction is explained in the following sections.

6.1.1 Clusterization

Pixel cells with charge above the readout threshold are read out. Pixel clusters are formed by grouping adjacent pixels. Both side and corner pixels are included in the cluster. A minimum cut of 10'000 electrons is applied on the total cluster charge to remove the pixel readout threshold effect which appeared as a small peak in the total cluster charge distribution. The cluster is projected along the vertical x (CMS $r\phi$ with pixel readout pitch of 100 μm) and horizontal y (CMS z with pixel readout pitch of 150 μm) axes by summing the charge collected in the pixels with the same axis. The cluster charge in ADC counts is converted into electrons using the pulse height calibration (see Section 5.1.1). In addition, a maximum of 50'000 electrons is required on the total cluster charge to reject large Landau fluctuations due to δ-rays.

The generated electron-hole pairs along the particle track experience a drift due to the combined action of electric and 3 T magnetic field along the x-axis. No Lorentz effect is present along the y-axis. The cluster width W_x along the x-axis is defined as (Eq. 4.12)

$$W_x = L - T \cdot \tan(\alpha) \tag{6.1}$$

where α is the particle impact angle, L is the Lorentz deflection, and T is the sensor thickness (see Fig. 4.12). The data are taken with particles moving perpendicularly to the sensor surface, i.e. with impact angle $\alpha = 0°$. Therefore in our case $W_x = L$. The Lorentz deflection is related to the Lorentz angle θ_L by (Eq. 4.11)

$$L = T \cdot \tan(\theta_L). \tag{6.2}$$

[1] ROOT is a data analysis framework: http://root.cern.ch/drupal/.

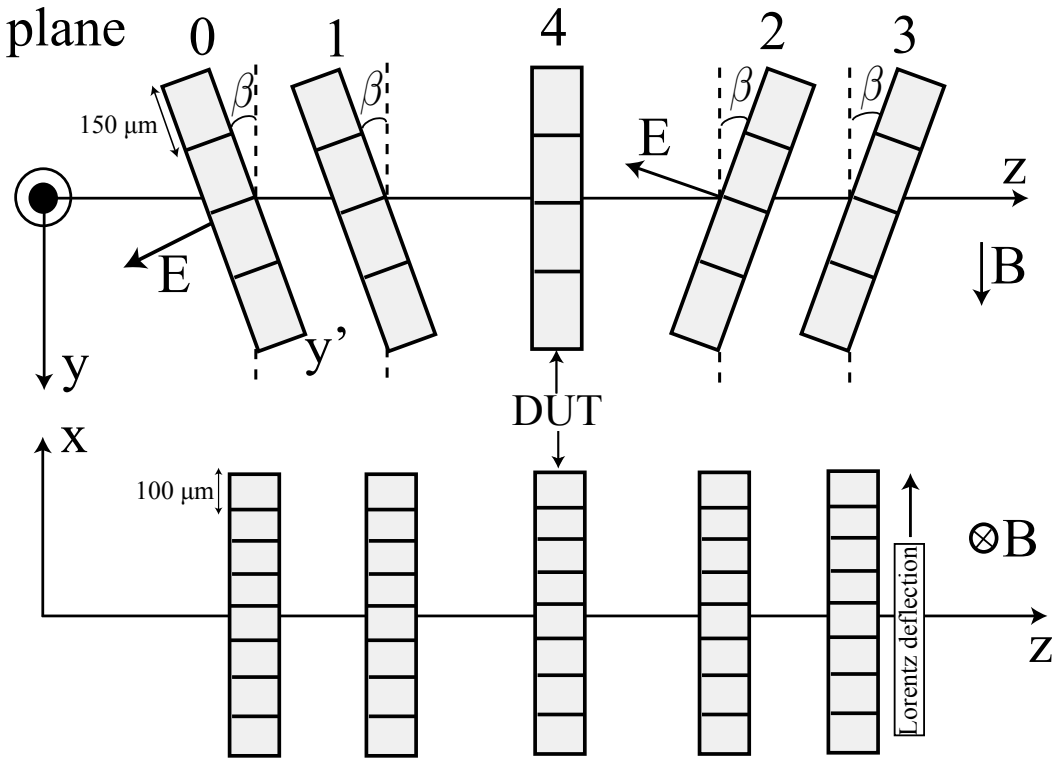

Figure 6.1 Layout of the testbeam apparatus. The apparatus top and side views are shown.

For an unirradiated sensor operated at 150 V bias the Lorentz deflection is 100 μm, corresponding to a Lorentz angle of $\theta_L = 19.4°$.

The cluster width W_y along the y-axis is defined as (see Fig. 4.13)

$$W_y = T \cdot \tan(\beta) \tag{6.3}$$

where β is the particle impact angle. W_y is 104 μm for the telescope sensors due to the constant angle $\beta = 20°$. For the device under test (DUT) W_y is zero.

6.1.2 Cluster position measurement

Two hit reconstruction algorithms are used in this work to determine the cluster position. The first reconstruction algorithm [2] is used for the telescope sensors. It uses the charge of the first and the last pixel in the cluster. In addition, the cluster width, impact angles, and the Lorentz deflection informations are required. This algorithm is applied to both x- and y-axes independently. The second reconstruction algorithm is the eta-algorithm which is used for the DUT sensors.

A sketch of the hit reconstruction algorithm for x-axis is shown in Fig. 4.12 and y-axis in Fig. 4.13. The calculation of the vertical and horizontal positions and the eta-algorithm are described in the following section.

[2]This algorithm is currently used in the CMS event reconstruction software (CMSSW)

6.1.3 Hit reconstruction algorithms

The hit position for the vertical x-axis is defined similar to Eq. 4.15 as

$$x_{hit} = x_{center} + \frac{q^x_{last} - q^x_{first}}{2(q^x_{first} + q^x_{last})} ||W_x| - W^x_{inner}| - \frac{L}{2} \tag{6.4}$$

where x_{hit} is the particle hit position, x_{center} is the cluster geometrical center, W^x_{inner} is the length of the inner pixels, q^x_{first} (q^x_{last}) is the charge in the first (last) vertical pixel, and L is the Lorentz deflection given by Eq. 6.2 (see also Fig. 4.12). W^x_{inner} is defined as

$$W^x_{inner} = (x_{size} - 2) \times P, \tag{6.5}$$

where x_{size} is the cluster size, and P is the pixel pitch. If the clusters are smaller than three pixels, W^x_{inner} is set to zero. If $||W_x| - W^x_{inner}|$ is greater than two, $||W_x| - W^x_{inner}|$ is set to one. Since the Lorentz deflection shifts the particle hit position, $L/2$ has to be subtracted from x_{hit}.

The hit position for the horizontal y-axis is given by Eq. 4.15 is

$$y_{hit} = y_{center} + \frac{q^y_{last} - q^y_{first}}{2(q^y_{first} + q^y_{last})} ||W_y| - W^y_{inner}|. \tag{6.6}$$

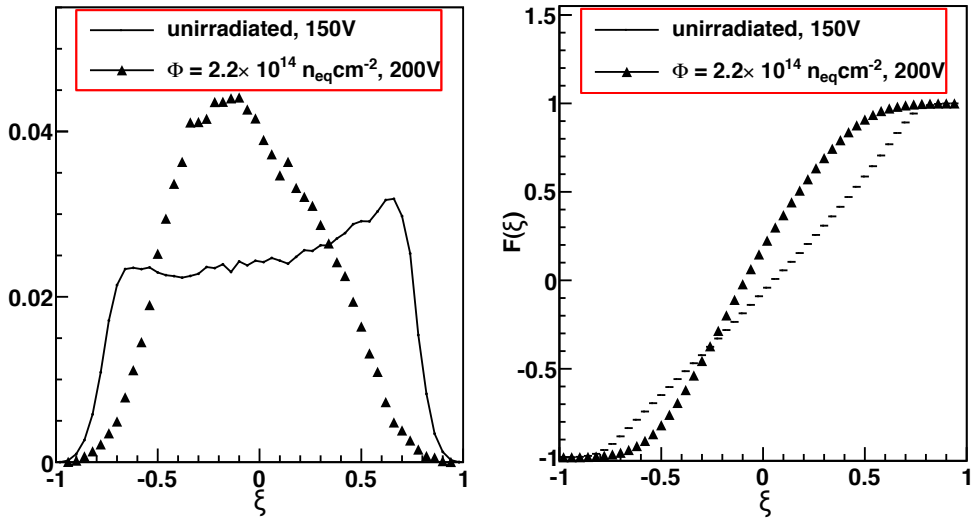

Figure 6.2 ξ distribution (left) and correction function $F(\xi)$ (right) measured with an unirradiated and an irradiated sensor.

The eta-algorithm is used to reconstruct hits in DUT sensors. We recall that the charge distribution between adjacent pixels is uniform before irradiation but it becomes asymmetric after irradiation due to radiation damage. This eta-algorithm weighs the last and first pixel charge in a cluster by ignoring the intermediate pixels and assuming that charge fluctuation between edge pixels carry no position information. It requires no a priori additional information

such as the Lorentz angle. It is therefore a robust algorithm with respect to radiation damage. The ξ variable is defined as

$$\xi = \frac{q^x_{last} - q^x_{first}}{q^x_{last} + q^x_{first}} \tag{6.7}$$

where q^x_{last} and q^x_{first} are charge collected by the first and last pixel in a cluster. The function $F(\xi)$ is extracted from the ξ distribution. The function $F(\xi)$ is defined similar to Eq. 4.17 as

$$F(\xi) = \frac{\int_{-1}^{\xi}(dN/d\hat{\xi})d\hat{\xi}}{\int_{-1}^{1}(dN/d\hat{\xi})d\hat{\xi}}, \tag{6.8}$$

where ξ is in pixel units. The ξ and $F(\xi)$ distributions are shown in Fig. 6.2 for an unirradiated and irradiated sensor. The uniform wide unirradiated ξ distribution becomes narrow and non uniform with irradiation due to the radiation induced charge loss. The particle hit position x_{hit} is then determined as

$$x_{hit} = x_{\text{first}} + F(\xi) \cdot P, \tag{6.9}$$

where x_{first} is the location of the first pixel in a cluster. Note the mainly linear dependence of F on ξ.

The eta-correction technique described in Section 4.2.4 corrects the pixel hits which are already reconstructed by hit reconstruction algorithms (see Section 4.2.2). Here the eta-algorithm is reconstructing the pixel hits while it is correcting the systematic asymmetries in the charge distributions due to the radiation damage. Therefore, the eta-algorithm itself is a correction.

6.1.4 Event Selection

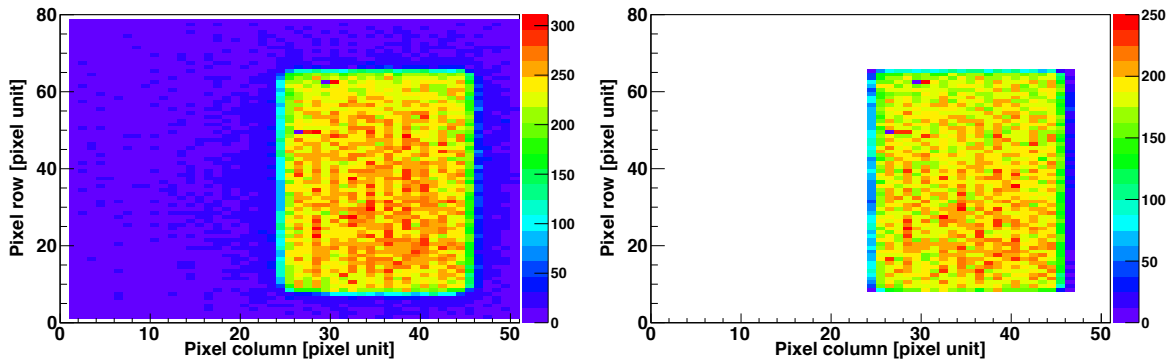

Figure 6.3 Hitmaps for a telescope sensor before the fiducial cut (left) and after the fiducial cut (right). The color scale shows the number of pixel hits.

Event selection steps are applied to the data. The selection is performed in two steps: events are first selected after the clusterization step; the second selection for the track reconstruction and alignment. First selection criteria are:

- Clusters with charge larger than 50'000 electrons are rejected to avoid δ-rays.

- A fiducial cut is applied by the trigger PIN diode which is smaller than the detector planes. Only hits which are in the area covered by the PIN diode are accepted. The fiducial cut shown in Fig. 6.3 removes the background events outside the PIN diode region. After the fiducial cut approximately 70% of the pixel hits remain.

Second selection criteria are:

- A hit multiplicity cut to reject the events with multiple tracks. The events with single hits in telescope and DUT sensors are selected. Therefore, the hit multiplicity cut selects one track per event.
- The hit coincidence is required to have events with single hit per telescope and DUT planes.

6.1.5 Spatial alignment and track reconstruction

In the testbeam setup the telescope and DUT use the same type of pixel sensors and front-end electronics. Therefore, telescope and the DUT sensor have the same measurement uncertainties in the vertical axis. Along the horizontal axis these uncertainties are different because the telescope planes are rotated around the vertical axis ($\beta = 20°$) as illustrated in Fig. 6.1 to improve the track resolution along this axis. In addition, there is no Lorentz deflection in the horizontal plane.

The hit axes in each pixel detector are ($x_j^{'}$,$y_j^{'}$) where j is the index of the plane (j = 1-5). The telescope horizontal y-axis measurements are corrected for the tilting angle β in order to align with the DUT sensor. Track reconstruction requires detector z position which also has to be corrected for the tilting angle β. The transformation to the telescope axes is then,

$$\begin{aligned} x_j &= x_j^{'} + \Delta x_j \\ y_j &= y_j^{'} \cos\beta + \Delta y_j \\ z_j &= z_j^0 + y_j^{'} \sin\beta \quad (j = 0, 1) \\ z_j &= z_j^0 - y_j^{'} \sin\beta \quad (j = 2, 3) \end{aligned} \tag{6.10}$$

where Δx_j and Δy_j are offsets to be determined, and z_j^0 is the measured z position of the detector j^{th} plane in the experimental setup (see Fig. 5.2).

The offsets are obtained from the mean residual distance between reconstructed track extrapolation and the measurement hits in a sensor. In general the alignment can be determined by minimizing the χ^2 defined as

$$\chi^2 = \sum_{tracks} (R_j/\sigma_j)^2 \tag{6.11}$$

where σ_j is the hit measurement uncertainty, and R_j is the particle hit residual. The hit residuals in the vertical x-axis R_{xj} and in the horizontal y-axis R_{yj} are defined by

$$\begin{aligned} R_{x_j} &= b_x + m_x z_j - (x_j^{'} + \Delta x_j) \\ R_{y_j} &= \frac{b_y + m_y z_j - (y_j^{'} + \Delta y_j)}{\cos\beta} \end{aligned} \tag{6.12}$$

where $b_{x,y}$ are the track offsets, and $m_{x,y}$ are the track slopes. Eq. 6.12 assumes linear tracks and each track is reconstructed by a linear least squares.

For the alignment of the testbeam detectors the so-called *Millepede* method [50] is used. The Millepede is a Fortran based program. This method allows the determination of up to several thousand alignment parameters in a simultaneous linear least squares fit of an arbitrary number of tracks. Due to the special structure of matrices with one set of global parameters (alignment parameters common to all the measurements) and many sets of local parameters (track parameters which apply only to a single measurement) the problem can be reduced to a solvable size, without making any approximations.

In Millepede a particle hit position h is defined by the linear equation

$$h = \sum_{i=1}^{n} a_j \cdot d_j + \sum_{j=1}^{\nu} \alpha_j \cdot \delta_j \tag{6.13}$$

where n is the number of global parameters, ν is the number of local parameters, a_j are the global parameters, d_j the global derivatives, α_j the local parameters, and δ_j the local derivatives. Straight particle tracks are assumed for the alignment. The magnetic effect is assumed to be negligible. Therefore, the local parameters for a single linear track are offset (α_1) and slope (α_2). The global parameters are z position of planes in the setup.

In the x- and y-axes the derivatives are determined using Eq. 6.12. They are shown in Table 6.1. Note that the angle β in the y-axis is defined as the rotation around the x-axis (see Fig. 6.1).

Table 6.1 Determined local and global derivatives for the testbeam axes. The z represents the detector position and the angle β in the y-axis is rotation around the x-axis.

	$\frac{\partial R}{\partial b}$ (local)	$\frac{\partial R}{\partial m}$ (local)	$\frac{\partial R}{\partial \Delta}$ (global)
x-coord	1	z	-1
y-coord	$1/\cos\beta$	$z/\cos\beta$	$-1/\cos\beta$

The alignment is performed for both telescope and DUT simultaneously. The x- and y-axes are treated independently since the measurements are uncorrelated. All the derivates and global parameters are provided to Millepede code [3] to perform the spatial alignment with the following constraints:

- First and last plane z positions in the setup are fixed to the measured values shown in Fig. 5.2.
- Due to initial large misalignment a cut of $\chi^2 = 10'000$ is applied for better performance [51].

The Millepede code provides the alignment constants. The testbeam setup is then aligned by subtracting these constants from the reconstructed measurements. The next step is to determine the position resolution of DUT. In order to do that the track reconstruction is performed. Each track is reconstructed by a least squares fit to the measured hits in the telescope planes. The fit parameters are then used to interpolate tracks on DUT. The residuals

[3] Millepede program code can be obtained from http://www.desy.de/~blobel.

are calculated as the difference between the predicted position from the telescope fit and the measured position on DUT. The total residual width is given by:

$$\sigma^2 = \sigma^2_{DUT} + \sigma^2_{track} + \sigma^2_{MS} \tag{6.14}$$

where σ_{DUT} is the position resolution of the DUT sensor, σ_{track} is the track interpolation uncertainty, and σ_{MS} is the multiple scattering contribution. The latter can be neglected given the high energy of the beam.

A simple Monte Carlo study is performed to estimate σ_{track}. In the Monte Carlo, five sensors are considered. Simulated hits for each sensor are smeared with a Gaussian distribution with a width of 10 μm. The sensor z-positions are taken from the setup (see Fig. 5.2) where the z positions are mechanically measured. A linear fit is applied to the hits in four sensors to reconstruct tracks and each track is then interpolated to the fifth sensor. Residuals are calculated as the difference between the interpolated hits and the simulated hits in the fifth sensor. The σ of this residual distribution is also defined by Eq. 6.14 since the track interpolation uncertainty and the fifth sensor resolution are compatible. Note that multiple scattering contribution is neglected. The quadratic difference between the σ of the residual distribution and expected σ_{DUT} of 10 μm results in $\sigma_{track} = 5$ μm. As a cross check a Gaussian fit is applied to the interpolated position distribution and the σ_{track} is also found to be 5 μm.

The residual distribution of all cluster sizes is not Gaussian due to the binary component. The position resolution is then given by the r.m.s. deviation of the residual distribution. For clusters larger than one pixel the residual distribution is Gaussian. In this case, the position resolution is defined by the sigma of a Gaussian fitted to the residual distribution. In addition, the track interpolation uncertainty is quadratically subtracted from the measurement results.

6.2 Results

In this section, the beam test measurement results for irradiated sensors are presented. The measurements are performed with 150 GeV pion beam in 3 T magnetic field. The tracks are perpendicular to the sensor plane.

6.2.1 Charge collection

Charge collection is measured as a function of irradiation fluence to determine the charge collection efficiency after irradiation. For unirradiated and irradiated sensors a bias voltage scan is also performed to provide an optimum setting for each irradiation fluence.

Charge collection is defined as the most probable value (MPV) of a Gaussian convoluted with a Landau function fitted to the total cluster charge distribution. The total charge distribution of an unirradiated sensor operated at 150 V bias voltage is shown in Fig. 6.4. The line is the fit while the markers represent the measurement. The MPV value is 24'760 electrons.

The charge collection for unirradiated and irradiated sensors is shown in Fig. 6.5. The points are the measurable Landau MPV values. For unirradiated sensors the charge collection increases for increasing bias voltages until it reaches a plateau. The saturation is starting already at 200 V bias. Note that the unirradiated sensor is fully depleted at 70 V bias. For irradiated sensors the charge losses are substantial and are partially recovered by applying higher bias voltages.

The charge collection of the highest irradiation fluence as a function of operated bias voltages is shown in Fig. 6.6. One cannot observe any saturation. At 500 V bias voltage the collected

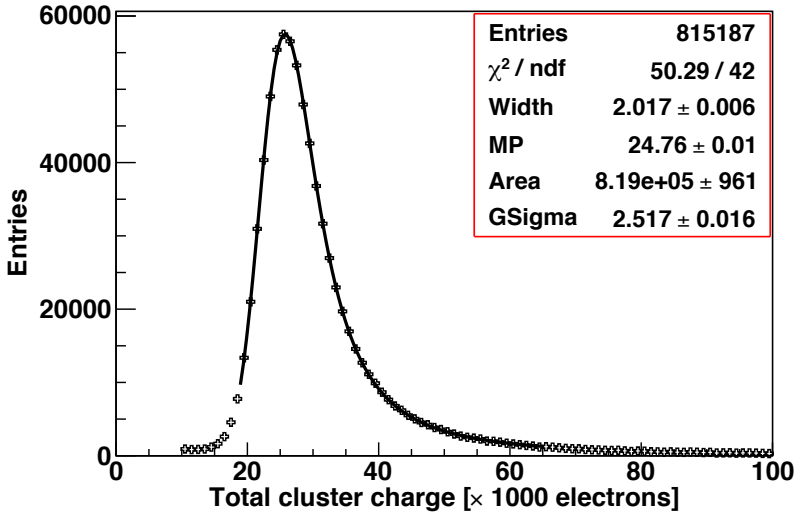

Figure 6.4 Total cluster charge for the unirradiated sensor operated at 150 V. The line is the fit of a Gaussian convoluted with a Landau distribution and the markers are the data.

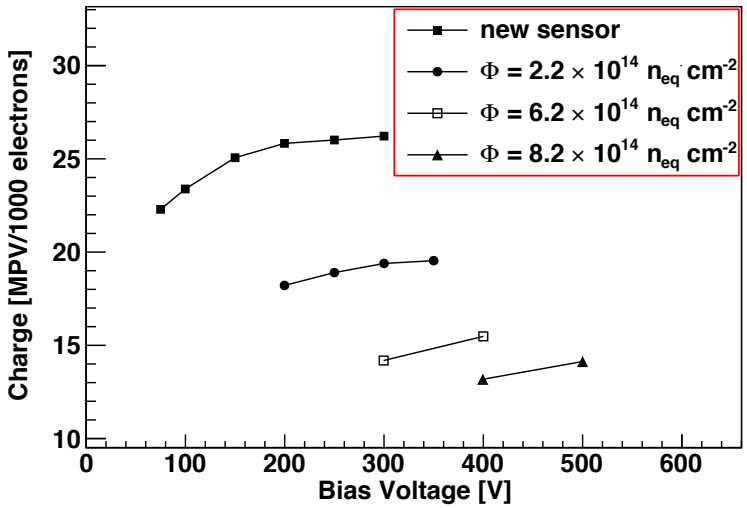

Figure 6.5 Most probable value of the total cluster charge distribution as a function of bias voltage for several irradiation fluences.

charge is 13'000 electrons which is approximately 50% of the charge deposit before irradiation.

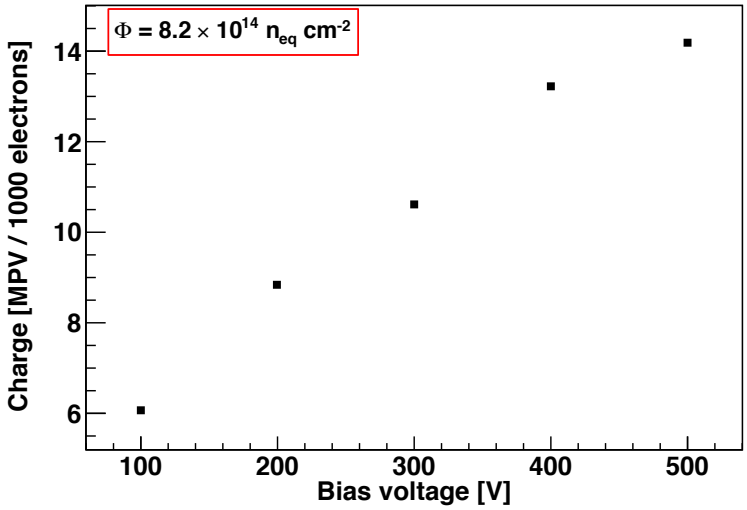

Figure 6.6 Charge collection as a function of bias voltage for the sensor irradiated to a fluence of $8 \times 10^{14} \mathrm{n_{eq}cm^{-2}}$.

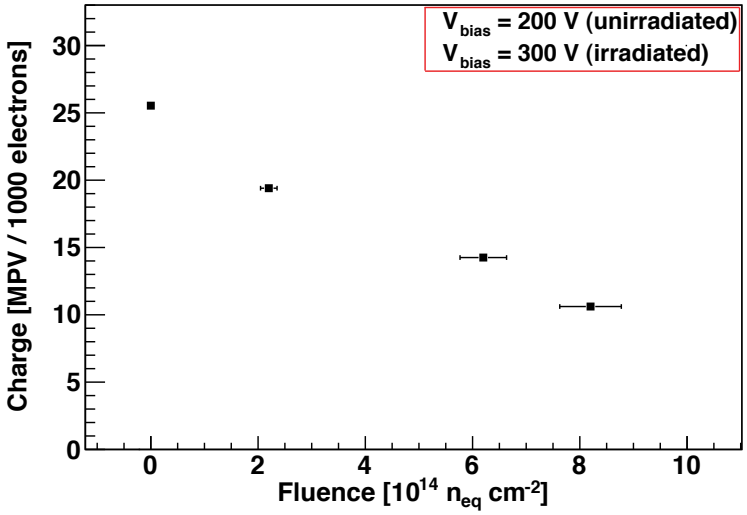

Figure 6.7 Charge collection as a function of irradiation fluence.

In Fig. 6.7, the charge collection is shown for several irradiated sensors operated at 300V bias and unirradiated sensor operated at 200 V bias. One can see the decrease of the collected charge for increasing irradiation fluences. The total collected charge is reduced to 77% of an unirradiated device for $\Phi = 2.2{\times}10^{14}$ $\mathrm{n_{eq}cm^{-2}}$. This amount is reduced to 46% for $\Phi =$

6.2×10^{14} $n_{eq}cm^{-2}$ and to even 38% for $\Phi = 8.2\times10^{14}$ $n_{eq}cm^{-2}$. It is important to note that a fluence of 6.2×10^{14} $n_{eq}cm^{-2}$ corresponds to the first 4 years of LHC operation for the innermost barrel layer of the CMS pixel detector (according to calculation given in Section 1.4).

6.2.2 Signal-to-noise ratio

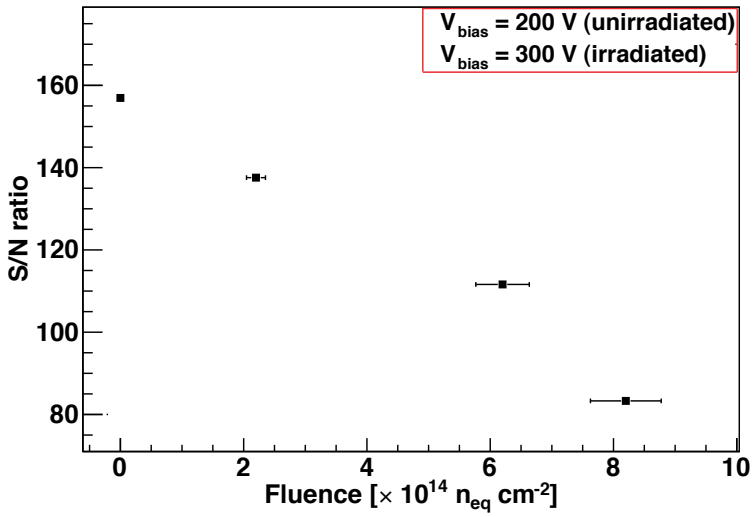

Figure 6.8 Signal-to-noise ratio measured with the pixel sensors as a function of irradiation fluence.

The signal-to-noise ratio (S/N) is measured for several irradiation fluences. The signal is determined from the MPV value of the total cluster charge. The operated bias voltage is chosen in such a way that the MPV value is measurable. The pixel noise is determined as described in Section 5.1.1.

The S/N ratios are shown in the Fig. 6.8 as a function of irradiation fluence. For a fluence of 2.2×10^{14} $n_{eq}cm^{-2}$ the S/N ratio is 137 (corresponding to 16'000 electrons). This corresponds to 87% of the unirradiated sensor. The signal drops to 70% of the unirradiated sensor for $\Phi = 6.2\times10^{14}$ $n_{eq}cm^{-2}$.

The noise does not increase as a function of irradiation fluence and the decrease of the S/N ratio is mainly due to charge collection. For the sensor irradiated to a fluence of 8.2×10^{14} $n_{eq}cm^{-2}$ the S/N ratio is 83 which corresponds to a signal of 10'000 electrons and to a noise of 124 electrons. 50% of the signal is lost due to the radiation damage. This fluence is in the range expected after the LHC luminosity upgrade.

6.2.3 Position resolution

The position resolution is measured separately for the horizontal and vertical axes. For the x-axis clusters larger than one pixel are reconstructed. These clusters are mainly due to the Lorentz deflection. The residual distribution of clusters of two pixels for an unirradiated sensor operated at 150 V bias is shown in Fig. 6.9. A Gaussian fit is applied to the residual

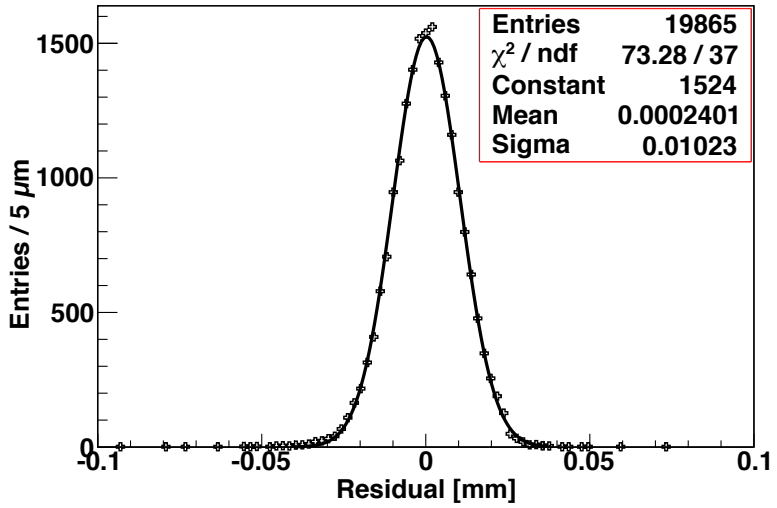

Figure 6.9 Residual distribution along the x-axis for clusters of two pixels. The sensor is unirradiated and operated at 150 V bias. The magnetic field is 3 T. The marker represents the data and the line is the Gaussian fit.

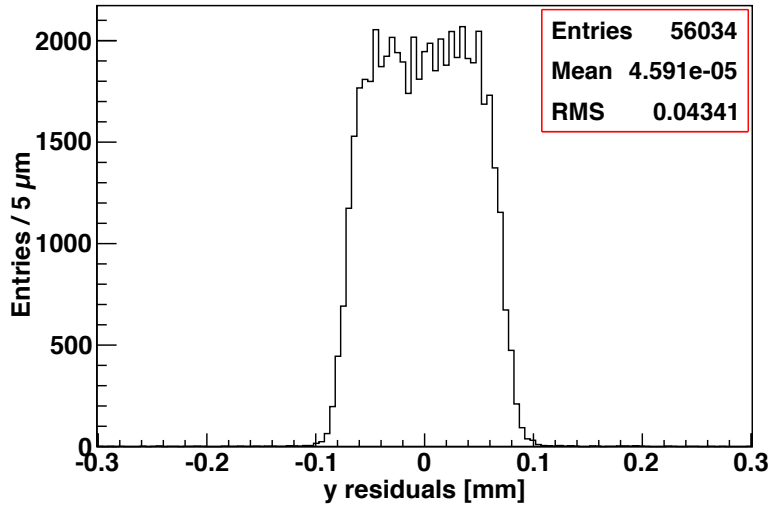

Figure 6.10 Residual distribution along the y-axis for clusters of one pixel. The detector is unirradiated and operates at 150 V bias. The magnetic field is 3 T.

distribution. The σ of the residual distribution is 10.2 μm, corresponding to a sensor position resolution $\sigma_{DUT} = 8.9$ μm (according to Eq. 6.14).

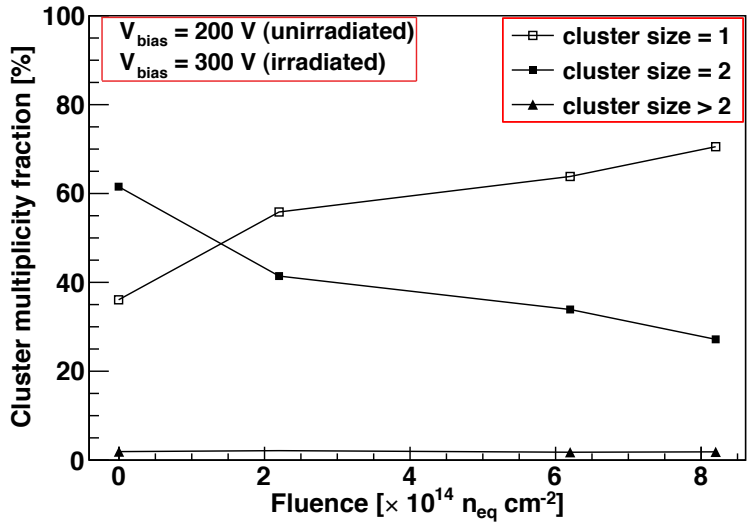

Figure 6.11 Cluster multiplicity as a function of irradiation fluence.

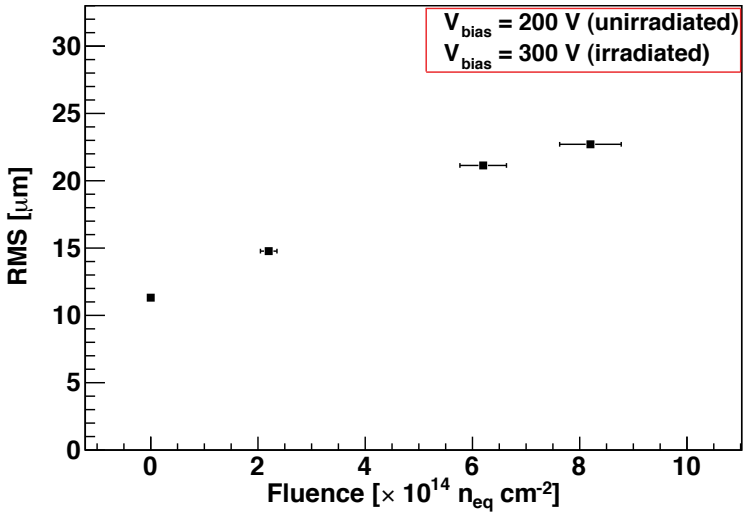

Figure 6.12 R.m.s. of the residual x-distribution as a function of irradiation fluence for all cluster sizes. Tracks are perpendicular to the sensor plane.

Along the y-axis there is no Lorentz deflection and clusters of a single pixel are dominant. The resulting residual distribution is binary. The residual distribution along the y-axis is shown in Fig. 6.10 for an unirradiated sensor operated at 150 V bias. The r.m.s. is 43 μm (as described in Section 4.2.3.2).

In this section, only the position resolution of the x-axis (100 μm pitch) is presented (CMS transverse $r\phi$ axis) for which the charge drift is affected by the Lorentz effect. The read-out threshold is 3000 electrons. The results are corrected with the function as described in Section 6.1.3.

The cluster multiplicity distribution as a function of irradiation fluence is shown in Fig. 6.11. The unirradiated sensor is operated at 200 V and the irradiated sensors at 300 V. Clusters of two pixels are dominant (62%) for the unirradiated sensor, while clusters of one pixel become dominant for irradiated sensors due to the charge loss.

For the sensor irradiated to a fluence of 8.2×10^{14} $n_{eq}cm^{-2}$ clusters of two pixels represent approximately 30% of the total. Clusters larger than two pixels represent 1% of the total, independently of the irradiation fluence.

The r.m.s. of the residual distribution as a function of irradiation fluence is shown in Fig. 6.12 for all cluster sizes. The bias voltage is 200 V for the unirradiated sensor and 300 V for the irradiated sensors.

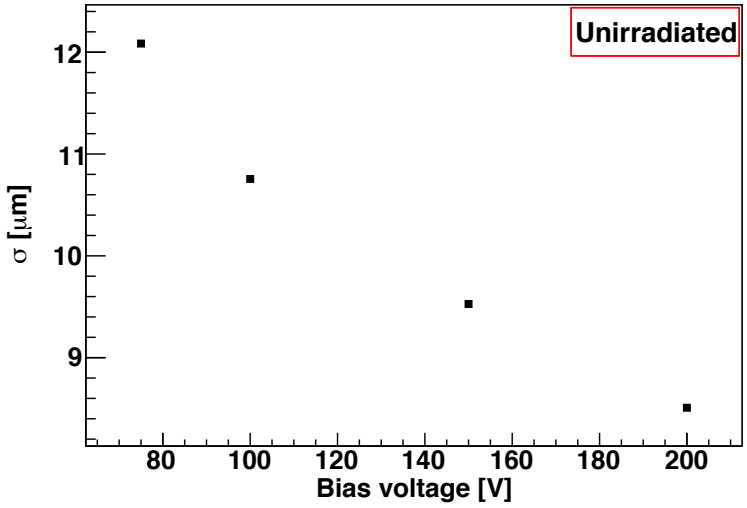

Figure 6.13 Position resolution as a function of bias voltage for the unirradiated sensor. Clusters of two pixels are used. Tracks are perpendicular to the sensor plane.

The higher bias voltage reduces the beneficial effect of the Lorentz deflection, leading to less charge sharing. A higher bias voltage increases the electric drift across the sensor bulk and therefore the Lorentz angle becomes smaller. The region of charge sharing between neighboring pixels shrinks. This leads to two consequences: the fraction of clusters larger than one pixel becomes smaller and the residual distribution of clusters of two pixels becomes narrower when the bias voltage is increased. As a result, the position resolution is smaller as shown in Fig. 6.13. Each point is the sigma of a Gaussian fit to the residual distribution. The position resolution for clusters of two pixels is below 10 μm at 200 V bias.

In Fig. 6.14, the unirradiated (at 200 V) and irradiated sensors (at 300 V) resolutions for clusters of two pixels are shown. Each point is the sigma of a Gaussian fit to the residual distribution. The position resolution for irradiated and unirradiated sensors is similar with 1-2 μm. The resolution improvement from unirradiated sensor to a sensor irradiated to a fluence

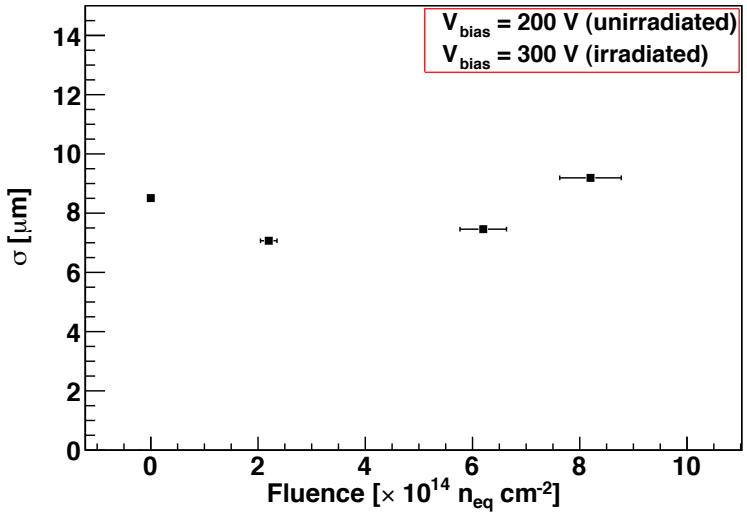

Figure 6.14 Position resolution as a function of irradiation fluence for clusters of two pixels. Tracks are perpendicular to the sensor plane.

of 2.2×10^{14} $n_{eq}cm^{-2}$ is due to higher bias voltage.

6.2.3.1 Position resolution for different readout thresholds

The readout threshold is applied by the pixel front-end electronics. In principle, the threshold has to be as low as possible since signals with lower charge are important to enhance the position resolution. Therefore, a threshold scan helps to determine the best possible readout threshold.

Table 6.2 Readout thresholds and threshold spreads for an unirradiated sensor operated at 100 V bias. The relative spreads are given in percentage.

Threshold (electrons)	Threshold spread (%)
2363	3.6
2690	2.8
3018	3.0
3673	2.5
4328	2.6
6293	1.7

The thresholds are applied during data taking and set through the data acquisition software. The scan is performed with the unirradiated sensor operated at 100 V bias voltage and in 3 T magnetic field. The scan for irradiated sensors could not be done due to the lack of time. Tracks are always perpendicular to the sensor plane.

Thresholds of all pixels in a ROC are filled into a histogram. The mean of the histogram

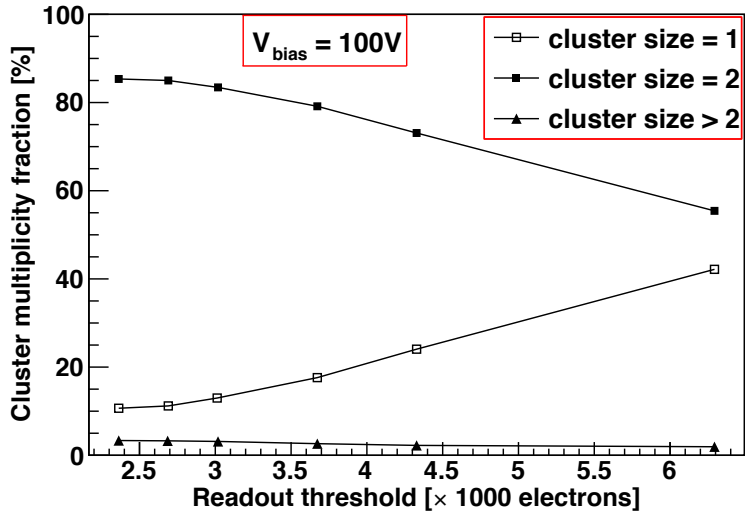

Figure 6.15 Cluster multiplicity as a function of readout threshold for an unirradiated sensor.

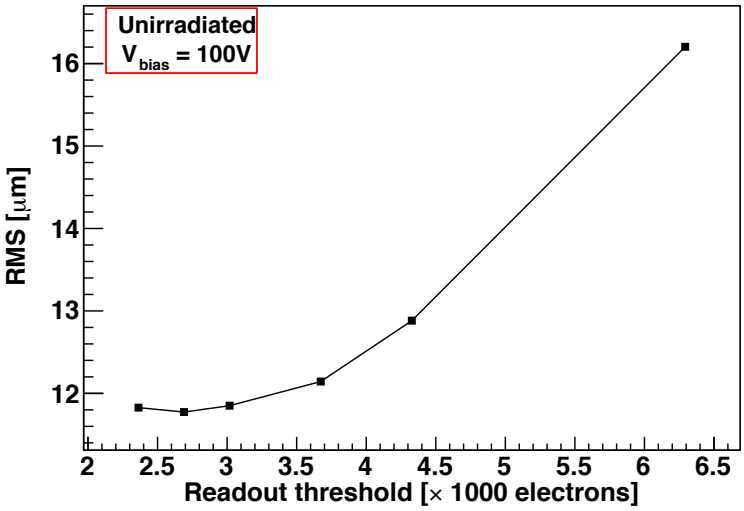

Figure 6.16 R.m.s. of the residual distribution as a function of readout threshold for all cluster sizes. Tracks are perpendicular to the sensor plane.

is defined as the threshold. The r.m.s. deviation is the threshold spread. The mean readout thresholds and the threshold spreads for an unirradiated sensor operated at 100 V bias are given in Table 6.2. The relative spreads are given in percent of the corresponding threshold. The threshold spreads are negligible compare to the corresponding threshold values.

The cluster multiplicity as a function of readout threshold is shown in Fig. 6.15. Clusters of two pixels become dominant when the threshold falls below 5000 electrons. Above 6500

electrons clusters of one pixel are dominant. The fraction of clusters larger than two pixels is less than 4% on average for 5000 electrons threshold.

The r.m.s. of the residual distribution is shown in Fig. 6.16 for several readout thresholds. A degradation of the position resolution is observed as the threshold increases. At a threshold of 3000 electrons, the r.m.s value is 12 μm, increasing to approximately 16 μm for a threshold of 6500 electrons.

The position resolution of clusters of two pixels is very slightly degraded when the threshold is higher than 3000 electrons (see Fig. 6.17). For a threshold of 3000 electrons, the resolution is 10.8 μm increasing to 11.8 μm for 6500 electrons. The degradation in the position resolution is hence only of the order of 1 μm.

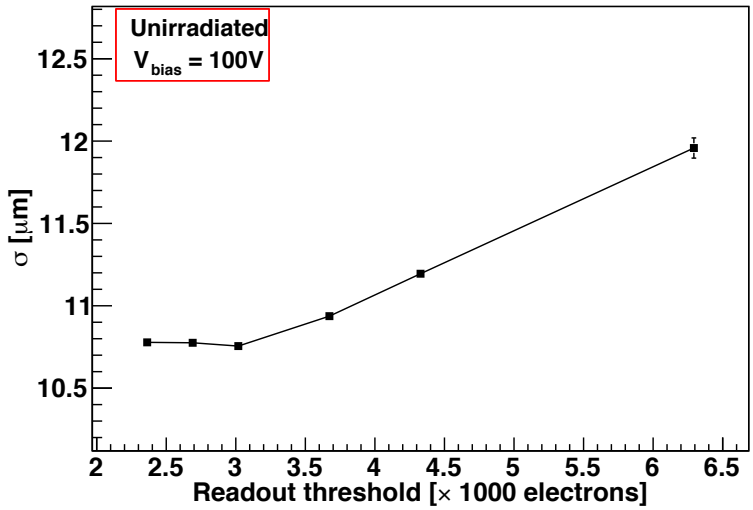

Figure 6.17 Gaussian σ of the residual distribution as a function of readout threshold for clusters of two pixels. Tracks are perpendicular to the sensor plane.

The degradation in position resolution can be explained by looking at the cluster multiplicity shown in Fig. 6.15. At the highest threshold (6500 electrons) the fractions of multiplicity one and two become equal. For low threshold, clusters of two pixels are dominant.

6.2.3.2 Comparison with the PIXELAV simulation

The PIXELAV simulation has a realistic radiation damage model well suited for performance studies of irradiated sensors. A simulation and beam test comparison is performed to validate the position resolution measurement results as a function of irradiation fluence and readout threshold.

PIXELAV is used to simulate the position resolution for unirradiated and irradiated sensors. Simulation data is produced and processed as described in Chapter 4 except that the magnetic field is modified to 3 T instead of original 4 T. The irradiation fluences are set to 2.2×10^{14} $n_{eq}cm^{-2}$ and 6.2×10^{14} $n_{eq}cm^{-2}$. The operated bias is 200 V for the unirradiated sensor and 300 V for the irradiated sensors. In addition, the unirradiated sensor operated at 100 V is simulated with several readout thresholds.

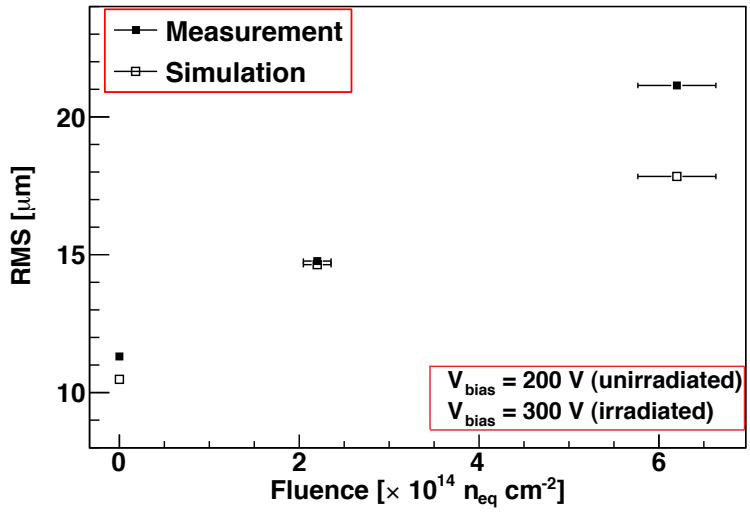

Figure 6.18 R.m.s. of the residual distribution as a function of irradiation fluence for all cluster sizes. The full squares show the measurement, the empty squares the PIXELAV prediction.

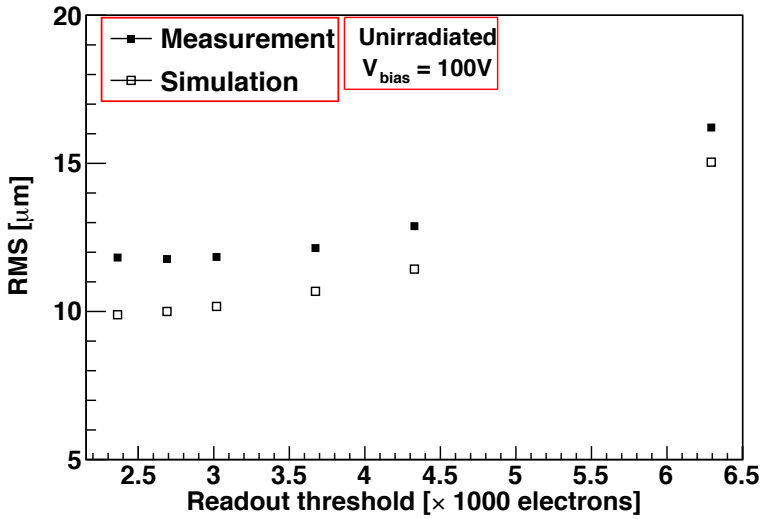

Figure 6.19 R.m.s. of the residual distribution as a function of readout threshold for all cluster sizes. The full squares show the measurement, the empty squares the PIXELAV prediction.

The measured position resolution is compared with the PIXELAV simulation. The r.m.s. of the residual distribution as a function of irradiation fluence is shown in Fig. 6.18. Good agreement is observed between simulation and test measurements except at the fluence of 6.2×10^{14} $n_{eq}cm^{-2}$ for which a 3 μm discrepancy is observed. The discrepancy might be due to miscalibrations of this sensor.

The comparison of the residuals r.m.s. as a function of readout threshold for the unirradiated sensor is shown in Fig. 6.19. The simulation describes qualitatively well the increase of r.m.s. but is systematically 1-2 μm below the measurement. Possible explanations for the discrepancies in Fig. 6.18 and Fig. 6.19 are miscalibration of sensors and the constant noise assumption for all unirradiated and irradiated sensors in the simulation. However, overall the simulation and the measurement results are in good agreement.

6.3 Summary

Several CMS pixel sensors have been tested before and after irradiation. The irradiation fluences were 2.2×10^{14} $n_{eq}cm^{-2}$, 6.2×10^{14} $n_{eq}cm^{-2}$, 8.2×10^{14} $n_{eq}cm^{-2}$ and the sensors were operated at bias voltages up to 500 V. The data was taken without and with a 3 T magnetic field.

Along the y-axis (150 μm pitch) clusters are mainly of one pixel. The resulting residual distribution is a binary distribution with an r.m.s. of 43 μm. For an unirradiated and irradiated sensors the position resolution along the x-axis (100 μm pitch) is given in Table 6.3 for perpendicular tracks in a 3 T magnetic field. All hits are corrected with the eta-algorithm as described in Section 6.1.3.

Table 6.3 Position resolution along CMS $r\phi$ axis for perpendicular tracks at different fluences and bias voltages in a 3 T magnetic field. All events are corrected for systematical effects (see Section 6.1.3).

		Position resolution σ_{DUT} (μm)	
Φ ($n_{eq}cm^{-2}$)	V_{bias} (V)	Cluster of two pixels	All cluster sizes
0	200	8.50 ± 0.01	11.30 ± 0.10
2.2×10^{14}	300	7.20 ± 0.02	14.80 ± 0.02
6.2×10^{14}	300	7.50 ± 0.02	21.00 ± 0.03
8.2×10^{14}	300	9.20 ± 0.02	22.70 ± 0.03

At the irradiation fluence of 6.2×10^{14} $n_{eq}cm^{-2}$ for which the replacement of the CMS innermost pixel barrel layer is foreseen (see Section 1.4), the measurement results are:

- The leakage current normalized to the total volume at 300 V is 30 μA.
- The charge collection efficiency is 46% of the unirradiated sensor.
- The signal-to-noise ratio is 112 corresponding to 14'000 electrons.

A comparison of the position resolution between simulation and beam test was performed as a function of irradiation fluence and readout threshold. The simulation can describe the measurement within 2 μm.

7 Summary and conclusions

In the CMS experiment the innermost pixel barrel layer sensors will be exposed to an irradiation corresponding to a fluence of 3×10^{14} $n_{eq}/cm^2/yr$ at full LHC luminosity (10^{34} $cm^{-2}s^{-1}$). As a consequence, sensor characteristics such as charge collection will be degraded due to radiation damage in the silicon crystal. The charge loss will deteriorate the determination of the particle hit position.

CMS pixel sensor performance before and after irradiation was studied in a testbeam. Irradiated sensors were exposed to a 150 GeV pion beam. A telescope made of pixel sensors was used to predict the hit position on test sensors. Sensors were tested at several bias voltages and irradiation fluences in a 3 T magnetic field, for the first time with the final CMS front-end electronics. Measurements as a function of irradiation fluence such as charge collection, leakage current and related damage rates, signal-to-noise ratio, and sensor spatial resolutions were performed. The position resolution as a function of readout threshold was also investigated for unirradiated sensors.

The CMS pixel sensors can be operated up to an irradiation fluence of 8.2×10^{14} $n_{eq}cm^{-2}$. The beam test results for the highest irradiation fluence of 8.2×10^{14} $n_{eq}cm^{-2}$ can be summarized as follows:

- The charge collection drops to 46% with respect to an unirradiated sensor.
- The leakage current normalized to the total sensor volume is 28 μA. The current is of the order of nA for the unirradiated sensor.
- The measured leakage current damage rate is $(2.5 \pm 0.4) \times 10^{-17}$ Acm^{-1}. It is in good agreement with previous measurements performed by the RD48 collaboration.
- The charge collection decreases due to the radiation damage but it can be recovered by applying higher bias voltages. The charge collection is increased from 6'000 electrons at 100V bias voltage to 14'000 electrons at 500 V bias voltage. The minimum operating bias voltage for the highly irradiated sensor is 300 V.
- The signal-to-noise ratio is about 83 corresponding to a signal of 10'000 electrons. The noise is 124 electrons.
- The position resolution was measured in 3 T magnetic field with tracks perpendicular to the sensor plane. Clusters of one pixel are dominant. The r.m.s. of the residual distribution for all cluster sizes is 23 μm and the position resolution is below 10 μm for clusters of two pixels at 300 V.

The position resolution as a function of readout threshold was measured for an unirradiated sensor at 100 V in 3 T magnetic field with perpendicular tracks. The readout thresholds were between 2400 electrons and 6500 electrons. For a readout threshold of 3'000 electrons

the r.m.s of the residual distribution is below 12 μm for all cluster sizes. This r.m.s is above 16 μm for the highest readout threshold (6500 electrons). The deterioration of the position resolution is due to the fact that at higher threshold pixels with low charge at the cluster edges are suppressed. For a readout threshold of 3'000 electrons the position resolution for two-pixel clusters is 10 μm. A degradation of 1 μm is observed in the position resolution for two-pixel clusters between the lowest (2400 electrons) and the highest readout threshold (6500 electrons).

The PIXELAV radiation damage model simulates sensor performance after irradiation. This simulation is important for the development of more accurate particle hit reconstruction algorithms and the calibration of charge sharing functions. The simulation shows that a position resolution of 13 μm can be achieved at the irradiation fluence of 6.2×10^{14} $n_{eq}cm^{-2}$. The systematical shifts on reconstructed hit positions, due to the radiation damage, can be corrected by the so called eta-correction. The eta-correction works well for both simulated and beam test data.

A comparison of the simulated and measured position resolution as a function of readout threshold and irradiation fluence was performed. The PIXELAV simulation can describe the measured values within 2 μm.

Bibliography

[1] E. Alagoz, V. Chiochia, M. Swartz, Simulation and hit reconstruction of irradiated pixel sensors for the CMS experiment, Nucl. Instrum. Meth. in Phys. Research A566 (2006) 40–44.

[2] V. Chiochia, E. Alagoz, M. Swartz, Sensor simulation and position calibration for the CMS pixel detector, Nucl. Instrum. Meth. in Phys. Research A569 (2006) 132–135.

[3] E. Alagoz, et al., Position resolution for the CMS barrel pixel detector after irradiation, will appear in Nuclear Physics B.

[4] C. Amsler, et al., Review of Particle Physics, Phys. Lett. B667 (2008) 1.

[5] M. M. Kado, C. G. Tully, The searches for Higgs bosons at LEP, Ann. Rev. Nucl. Part. Sci. 52 (2002) 65–113.

[6] The TEVNPH Working Group, Combined CDF and DZero Upper Limits on Standard Model Higgs-Boson Production with up to 4.2 fb-1 of Data .

[7] P. W. Higgs, Broken symmetries, massless particles and gauge fields, Phys. Lett. 12 (1964) 132–133.

[8] A. Djouadi, J. Kalinowski, M. Spira, Hdecay: A program for higgs boson decays in the standard model and its supersymmetric extension, Comput. Phys. Commun. 108 (1998) 56–74.

[9] Evans, Lyndon, (ed.) and Bryant, Philip, (ed.), LHC Machine, JINST 3 (2008) S08001.

[10] G. Aad, et al., The ATLAS Experiment at the CERN Large Hadron Collider, JINST 3 (2008) S08003.

[11] R. Adolphi, et al., The CMS experiment at the CERN LHC, JINST 0803 (2008) S08004.

[12] K. Aamodt, et al., The ALICE experiment at the CERN LHC, JINST 0803 (2008) S08002.

[13] A. A. Alves, et al., The LHCb Detector at the LHC, JINST 3 (2008) S08005.

[14] G. Anelli, et al., The TOTEM experiment at the CERN Large Hadron Collider, JINST 3 (2008) S08007.

[15] CMS, the Compact Muon Solenoid: Technical proposal CERN-LHCC-94-38.

[16] G. Acquistapace, et al., CMS, the magnet project: Technical design report CERN-LHCC-97-10.

[17] CMS, tracker technical design report CERN-LHCC-98-06.

[18] G. L. Bayatian, et al., CMS physics: Technical design report CERN-LHCC-2006-001.

[19] CMS: The electromagnetic calorimeter. Technical design report CERN-LHCC-97-33.

[20] CMS: The hadron calorimeter technical design report CERN-LHCC-97-31.

[21] CMS, the Compact Muon Solenoid. Muon technical design report CERN-LHCC-97-32.

[22] S. König, C. Hörmann, R. Horisberger, S. Streuli, R. Weber, Assembly of the CMS pixel barrel modules, Nucl. Instrum. Meth. in Phys. Research A565 (2006) 62–66.

[23] H. C. Kastli, et al., Design and performance of the CMS pixel detector readout chip, Nucl. Instrum. Meth. in Phys. Research A565 (2006) 188–194.

[24] E. Bartz, The 0.25-mu-m token bit manager chip for the CMS pixel readout, Prepared for 11th Workshop on Electronics for LHC and Future Experiments (LECC 2005), Heidelberg, Germany, 12-16 September 2005.

[25] T. Rohe, Design and test of pixel sensors for the ATLAS pixel detector, Nucl. Instrum. Meth. in Phys. Research A460 (2001) 55–66.

[26] T. Rohe, et al., Fluence dependence of charge collection of irradiated pixel sensors, Nucl. Instrum. Meth. in Phys. Research A552 (2005) 232–238.

[27] S. Dambach, CMS pixel module optimization and B meson lifetime measurements, Ph.D. thesis, ETH Zurich, Switzerland (2009).

[28] D. Kotlinski, et al., The control and readout systems of the CMS pixel barrel detector, Nucl. Instrum. Meth. in Phys. Research A565 (2006) 73–78.

[29] NIST, http://physics.nist.gov/PhysRefData/Star/Text/ESTAR.html.

[30] N. Arora, J. Hauser, D. Roulston, Electron and hole mobilities in silicon as a function of concentration and temperature, Electron Devices, IEEE Transactions on 29 (2) (1982) 292–295.

[31] F. Lemeilleur, G. Lindstrom, S. Watts, Third RD48 status report CERN-LHCC-2000-009.

[32] R. Wunstorf, Radiation hardness of silicon detectors: Current status, IEEE Trans. Nucl. Sci. 44 (1997) 806–814.

[33] E. Alagoz, Planar Edgeless Silicon Detectors for the TOTEM Experiment, Master's thesis, University of Siegen, Germany (2005).

[34] S. J. Watts, Overview of radiation damage in silicon detectors: Models and defect engineering, Nucl. Instrum. Meth. in Phys. Research A386 (1997) 149–155.

[35] R. Kaufmann, Development of Radiation Hard Pixel Sensors for the CMS Experiment, Ph.D. thesis, University of Zurich, Switzerland (2001).

[36] M. Swartz, CMS pixel simulations, Nucl. Instrum. Meth. in Phys. Research A511 (2003) 88–91.

[37] ISE-TCAD, Integrated System Engineering AG, Zürich, Switzerland.

[38] H. Bichsel, Straggling in thin silicon detectors, Rev. Mod. Phys. 60 (1988) 663–699.

[39] R. Kaufmann, B. Henrich, Charge Drift in Silicon, CMS Pixel Internal Note.

[40] S. Ramo, Currents induced by electron motion, Proceedings of I.R.E. 27 (1939) 584–585.

[41] A. Dorokhov, et al., Tests of silicon sensors for the CMS pixel detector, Nucl. Instrum. Meth. in Phys. Research A530 (2004) 71–76.

[42] V. Eremin, E. Verbitskaya, Z. Li, The origin of double peak electric field distribution in heavily irradiated silicon detectors, Nucl. Instrum. Meth. in Phys. Research A476 (2002) 556–564.

[43] M. Swartz, et al., Observation, modeling, and temperature dependence of doubly peaked electric fields in irradiated silicon pixel sensors, Nucl. Instrum. Meth. in Phys. Research A565 (2006) 212–220.

[44] V. Chiochia, et al., Simulation of heavily irradiated silicon pixel sensors and comparison with test beam measurements, IEEE Trans. Nucl. Sci. 52 (2005) 1067–1075.

[45] D. Kotlinski, S. Cucciarelli, Pixel hit reconstruction, CMS Internal Note 2004/014.

[46] G. Lindstrom, et al., Radiation hard silicon detectors developments by the RD48 (ROSE) Collaboration, Nucl. Instrum. Meth. in Phys. Research A466 (2001) 308–326.

[47] A. Starodumov, et al., Qualification procedures of the CMS pixel barrel modules, Nucl. Instrum. Meth. in Phys. Research A565 (2006) 67–72.

[48] M. Moll, Radiation damage in silicon particle detectors: Microscopic defects and macroscopic properties , Ph.D. thesis, University of Hamburg, Germany (1999).

[49] A. Dorokhov, Performance of Radiation Hard Pixel Sensors for the CMS Experiment, Ph.D. thesis, University of Zurich, Switzerland (2001).

[50] V. Blobel, C. Kleinwort, A new method for the high-precision alignment of track detectors, arXiv: hep-ex/0208021.

[51] Private communication from Dr. M. Stoye and Dr. J. Castillo.

List of Figures

List of Tables

Acknowledgments

This PhD thesis would not have been possible without the support of many people. I would like to express my gratitude to my thesis supervisor, Prof. Dr. Claude Amsler, who was abundantly helpful and offered invaluable assistance, support and guidance. Deepest gratitude are also due to the members of the promotion committee, Prof. Dr. Vincenzo Chiochia and Dr. Alexander Schmidt without whose knowledge and assistance this study would not have been successful. I would like to thank to Prof. Dr. Morris Swartz and Dr. Thomas Speer for their constant support during my PhD research.

Special thanks to PSI CMS pixel people: Dr. Roland Horisberger, Dr. Tilman Rohe, Dr. Danek Kotlinski, Prof. Dr. Urs Langenegger, Dr. Andrey Starodumov, Dr. Peter Trüb, Dr. Wolfgang Erdmann, Sarah Dambach, and Beat Meier.

My deep gratitude to Prof. Dr. Claude Amsler's research group members: Dr. Christian Regenfus, Dr. Peter Robmann, Vittorio Boccone, Tanja Rommerskirchen, Lotte Wilke, Dimitrios Tsirigkas, Jacky Rochet, and Patricia Perreard.

Many thanks to CERN Turkish Forum members Dr. Gökhan Ünel, Dr. V. Erkcan Özcan, Dr. Özgür Çobanoğlu, Dr. Tülay Çuhadaroğlu, Öznur Mete, and all the other members who supported me during my PhD.

Last but not least I owe my loving thanks to my wife, my friends and my family...